RESIDUAL STRESSES AND DEFLECTIONS IN COMPLEX SHAPES FORMED BY LASER BENDING

by

Louis King Biegeleisen

M.S., University of Georgia
(1975)

SUBMITTED TO THE DEPARTMENT OF OCEAN ENGINEERING
IN PARTIAL FULFILLMENT OF THE REQUIREMENTS
FOR THE DEGREE OF

S.M., NAVAL ARCHITECTURE AND MARINE ENGINEERING

at the

MASSACHUSETTS INSTITUTE OF TECHNOLOGY

June 1986

Signature of Author ______________________________
Department of Ocean Engineering
June 2, 1986

Certified by ______________________________
Dr. Koichi Masubuchi

Accepted by ______________________________
Professor A. Douglas Carmichael
Chairman, Department Graduate Committee Ocean Engineering

Residual Stresses and Deflections in Complex Shapes Formed by Laser Bending

by

Louis King Biegeleisen

Submitted to the Department of Ocean Engineering on June 2, 1986 in partial fulfillment of the requirements for the degree of S.M., Naval Architecture and Marine Engineering.

ABSTRACT

Previous quantitative results obtained at M.I.T. on the bending of steel by laser line heating to produce simple angular deflections have been verified and expanded. Deflections and residual stresses in compound shapes formed by laser line heating of steel are measured and analyzed. From the measured deflections, algorithms are developed allowing the construction of idealized compound shapes including the dish, saddle, cone, and sine. All algorithms are developed from single pass laser line heating data.

Thesis Supervisor: Dr. Koichi Masubuchi
Title: Professor of Ocean Engineering and Materials Science

ACKNOWLEDGEMENTS

I would like to express my gratitude to Professor K. Masubuchi for his supervision and support during this research. Special appreciation is extended to Andrew Debicarri for his suggestions during the residual stress measurements.

TABLE OF CONTENTS

LIST OF FIGURES

LIST OF TABLES

CHAPTER ONE

INTRODUCTION

It has been substantially demonstrated by Masubuchi [1], McCarthy [2], et. al. that bending of steel plates by laser line heating is practicable for simple one dimension bending and possible for bending complex shapes. In some ways laser bending is preferable to mechanical forming. These include:

(1) Minimal material degradation [3],[4];

(2) The ability to determine deflection angles with heat input parameters;

(3) The ability to automate the process fully with a closed-loop feedback control system.

References [1] and [2] also show that complex shapes such as the dish, saddle, sine, and cone which are not readily formed as a unit by mechanical processing, can easily be formed by laser line heating. Much literature exists extolling the advantages of line heating over mechanical forming for complex shapes. However, to date most attention has been focussed on the use of flames for bending steels.

Historically, line heating by flame has been an art rather than a science. Attempts have been made to quantify the physics of flame bending including the description of plastic and elastic phenomena by boundary integral equations and finite element methods [5]. In spite of the application of advanced and sophisticated mathematical tools to the field of flame and laser bending, simple and easily programmable algorithms to predict the curvature of complex shapes by flame or laser bending do not exist.

Lasers have been used for decades to produce an intense and concentrated line or point heat for welding or producing micro and mini-holes. The technology already exists to control accurately the heat input and heating pattern of a laser by optically defocussing the beam. This high degree of control indicates the major advantage of laser line heating over flame line heating. Specifically, a laser system is, by its very nature, quite adaptable to a closed-loop control system for thermal bending of steel into complex shapes including those with well-defined inflection points.

Today is a period of transition in manufacturing from simple open-loop and closed-loop control systems to the development and implementation of "expert" and robotic systems. The ability to control and to predict accurately relevant thermal parameters is critical if plate bending by line heating is to become an accepted automated manufacturing process.

In spite of the expense of a high power laser system, its use in industry is increasing rapidly. Discussions with one major high power CO_2 industrial scale laser manufacturer revealed that, for that company, the sale of large scale industrial lasers is increasing about thirty per cent per year. Many companies who would not be willing or able to apply the large capital expenditures required for a laser system might invest in an automated flame bending system. For that reason, the algorithms developed in this paper were designed to be applicable to flame bending with obvious adjustment to power-deflection parameters.

The purpose of the research discussed in this paper is threefold. First, to prove the reproducability of laser line heating by predicting and then reproducing one of the experiments discussed in references [1] and [2]. Secondly, to measure the residual stresses found in one of the shapes previously formed by laser line heating. Finally, and most importantly, to develop simple, linear algorithms which utilyzes the extensive, simple, one dimensional data base to mathematically construct complex shapes. Algorithms for the dish, saddle, cone, and sine shape are separately developed. They are empirically formulated from shapes previously formed by laser line heating. These algorithms are then used to predict the deflections of shapes to be formed in subsequent experiments.

CHAPTER TWO

PREVIOUS AND FUTURE RESEARCH

2.1 Long-Term Research Goals

A discussion of future research is normally included at the end of a paper. In this case, in order to understand adequately the intent and scope of current research in laser forming of steel plates, one must be aware of the long-term research goals of which the work reflected in this paper is but one step in the process.

The ultimate goal of current research in laser bending of steel plates is the development of a closed-loop and/or expert system to fully automate the process of forming simple and complex shapes frequently found in the shipbuilding industry. Although the focus of research has been on using a high power (6-15 kW) laser as the line heater, it is anticipated that the method will be readily adaptable to flame bending. Several subsystems must be developed in parallel in order to accomplish this:

a) An extensive data base for one dimensional bending must be established correlating plate deflections to heating and material parameters.

b) Algorithms must be developed so that the system has initial values and heating patterns from which to start and from which the system could estimate correct curvatures for complex shapes when encountering new sets of requirements.

c) A "real-time" deflection measurement subsystem must be developed to give closure to the feedback system.

d) Computer programs and methodologies must be developed to control and interface the database, algorithms, and the real-time deflection measurements. Also, they must be capable of interfacing with the bending laser and movable bedplate systems.

e) Prototype total system development and assembly.

References [1] and [2] and part of this paper show that step "a" has been accomplished. A low power laser/video camera interferometer system is being developed at this time. It should accomplish step "c". The main purpose of this paper is to describe the effort to accomplish step "b"; namely, the development of the algorithms. Subsystem "d" and total system integration will follow from past and current research.

2.2 Review of Previous Research

References [1] and [2] discuss in detail the results of experiments on the bending of steel plates by a high power CO_2 laser. Figure 2.2-1 is a sketch of the basic method of laser bending a plate.

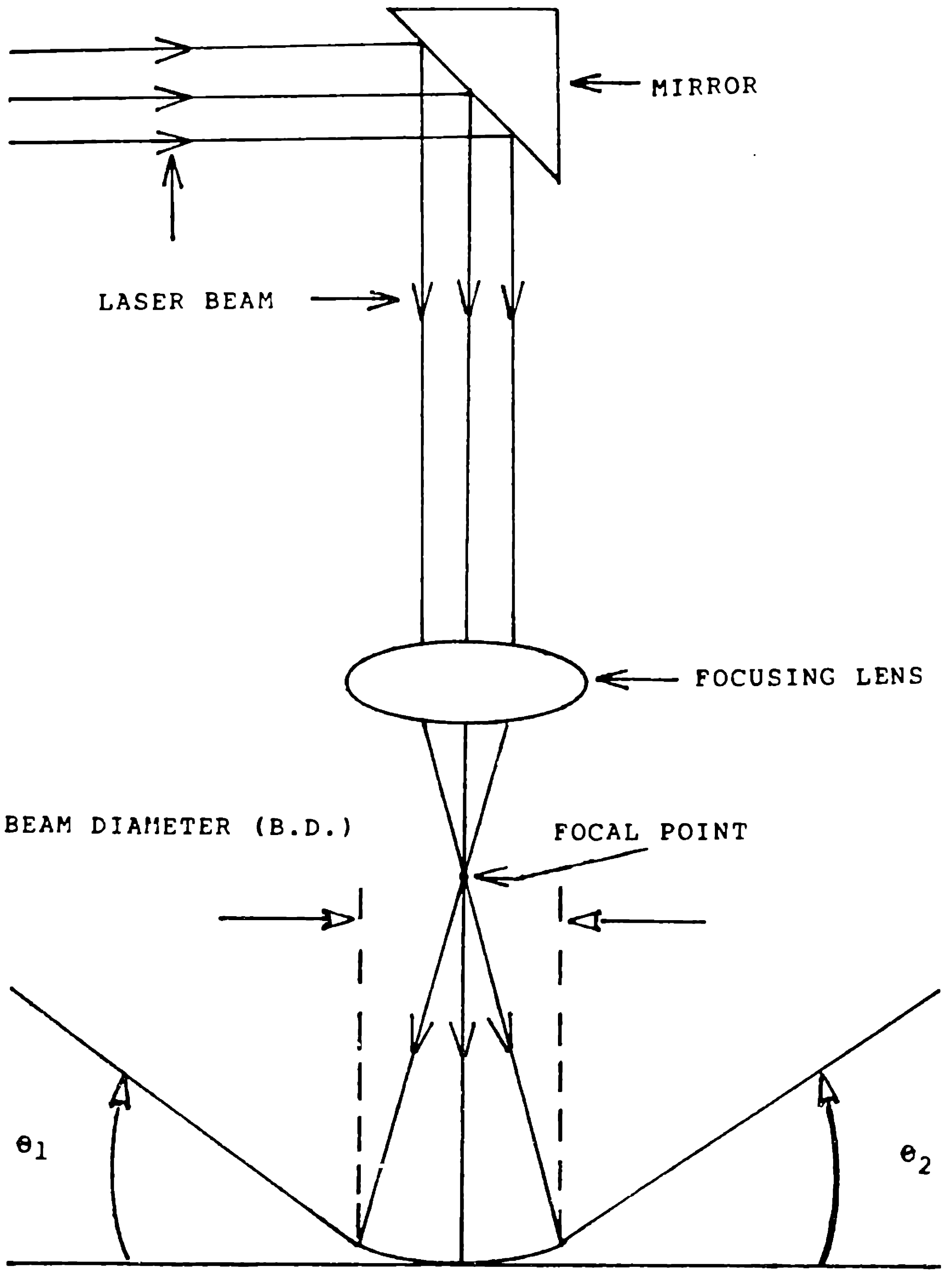

Figure 2.2-1: Diagram of a Basic Laser Bending Apparatus

The steel plate rests on a movable bed plate such that the stationary beam irradiates the surface of the steel as a line pass. Primary deflection is perpendicular to the laser line pass. The resulting deflection angle, θ_f, is the sum of θ_1 and θ_2. All deflection angles given in [1] and [2] are in terms of θ_f.

Many factors can affect the amount of curvature. These include:

1) Plate thickness and type of steel.
2) Heat input which is, itself, dependent on the laser power, optical path energy loss, absorbance fraction by the plate of the delivered infrared power, and the speed of the plate underneath the laser beam.
3) Plate restraints such as clamping and free edge effects.
4) Plate cooldown rate.
5) Laser beam spot geometry may have an effect by changing the power density delivered to the plates surface.

Since metals are highly reflective to the infrared radiation (~10 microns) emitted from a CO_2 laser, the plate surface must be coated with an absorbing substance. Black spray paint is currently being used for that purpose. Optical losses are approximately ten per cent for the 15 kW laser used at the Naval Research Laboratory.

Heat input is being represented by the following parameters:

$P/\sqrt{V}$ and $P/t\sqrt{V}$

where P is the laser power is kWatts less optical loss, V is the plate speed in inches-per-minute and t is the thickness of the plate in inches. The deflection angle, θ_f, is correlated to specified $P/\sqrt{V}$ and/or $P/t\sqrt{V}$. The deflection angle has been measured by dial gages and a laser interferometer ([1],[2]). Table 2.2-1 and figures 2.2-2 and 2.2-3 are extracted from reference [1]. Clearly, the results represented in the graphs and table can be programmed into a computer with routines for estimating deflections at parameters not previously found by experiment. These results with the additional data measured and described later in this paper form the data base from which the algorithms for complex shapes are developed.

The free edge of the plate where residual stresses must vanish have been shown ([1],[2]) to have a pronounced effect on the magnitude of the deflection angle for a given set of parameters. Distortion angle decreases relative to that obtained on the interior of the plate at the edges of a plate. However, approximately one beam diameter (1.5 inches, nominal) away from the edge, this effect is small and will generally be neglected in this paper. For purposes of the analyses in this paper the effects of the cooldown rate, edge restraint, and beam spot pattern also will be neglected unless otherwise specified.

Table 2.2-1: Process Parameters and Test Results Obtained in Parametric Studies

	Thickness (in)	Size (in)	Power (kw)	Speed (ipm)	Heat Input (KJ/in)	$\frac{P}{\sqrt{v}}$	$\frac{P}{t\sqrt{v}}$	θ_f^* (degree)
Original Parametric Study	1/4	5x10	9.0	25	19.4	1.80	7.2	1.45
			7.0	20	18.9	1.56	6.24	2.00
			5.0	16	16.9	1.25	5.0	0.84
			3.0	12	13.5	0.86	3.44	0.48
	1/2	12x12	12.7	16	42.8	3.17	6.34	1.40
			7.0	12	31.5	2.02	4.04	0.90
			5.0	8	33.8	1.76	3.52	0.70
			3.0	6	27.0	1.22	2.44	0.20
	3/4	12x12	10.5	10	63	3.32	4.43	0.82
			11.0	12	55	3.17	4.23	0.75
			9.0	12	45	2.6	3.47	0.60
			5.0	8	37.5	1.76	2.35	0.33
	1	12x12	10	9	66	3.33	3.33	0.75
			9	9	60	3.00	3.50	0.64
			7	8	52.5	2.47	2.47	0.33
			5	8	37.5	1.76	1.76	0.12
Additional Parametric Study	1/2	12x12	5	12	25	1.44	2.88	0.33
			5	10	30	1.58	3.16	0.55
			5	8	37.5	1.76	3.52	0.92
			5	6	50	2.04	4.08	1.23
			5	5	60	2.24	4.48	1.40

Note:

*The amount of angular distortion after the plate cooled to room temperature, or the final angular distortion, θ_f is shown here.

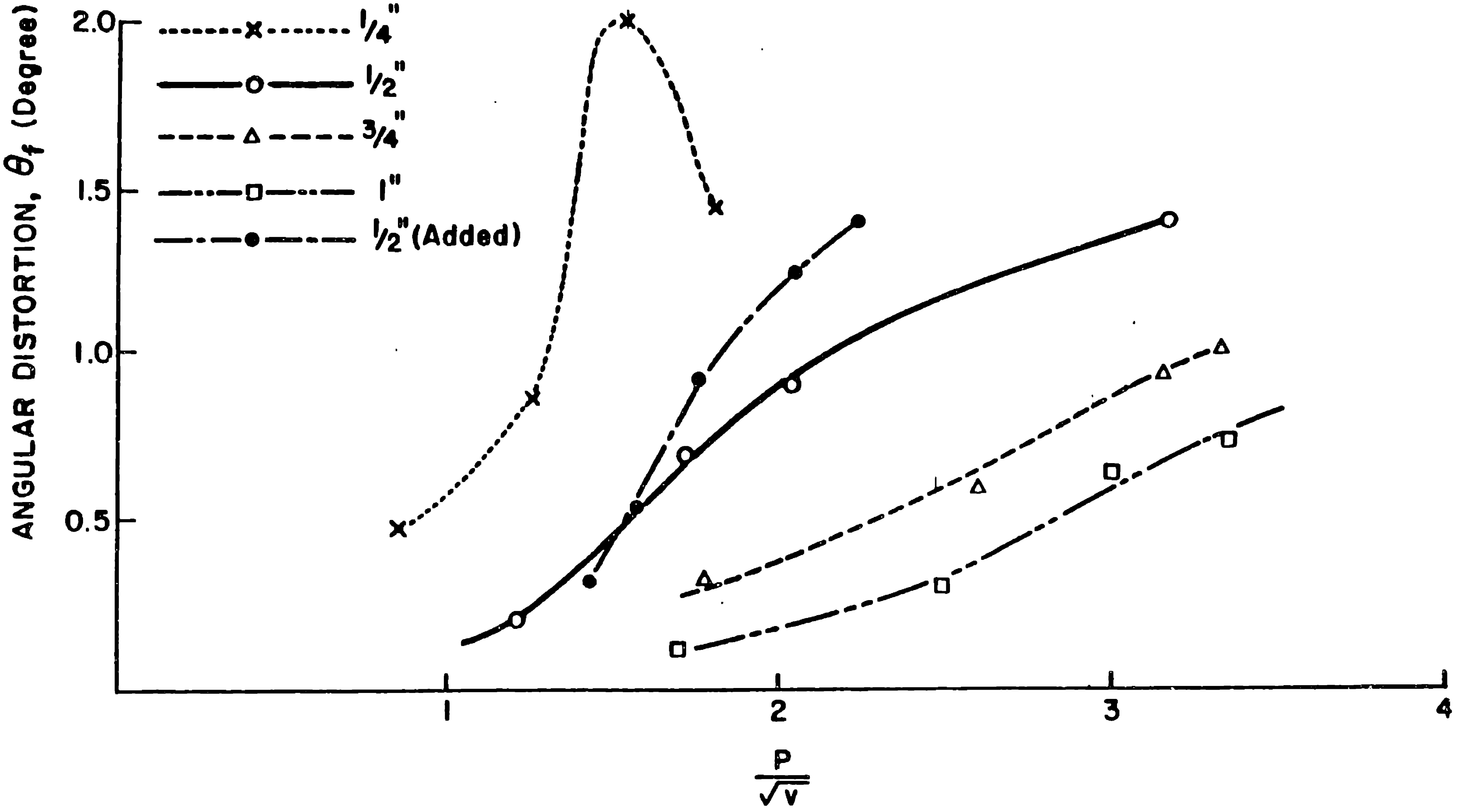

Figure 2.2-2: Results of Parametric Studies-$P/\sqrt{V}$ vs. Angular Distortion

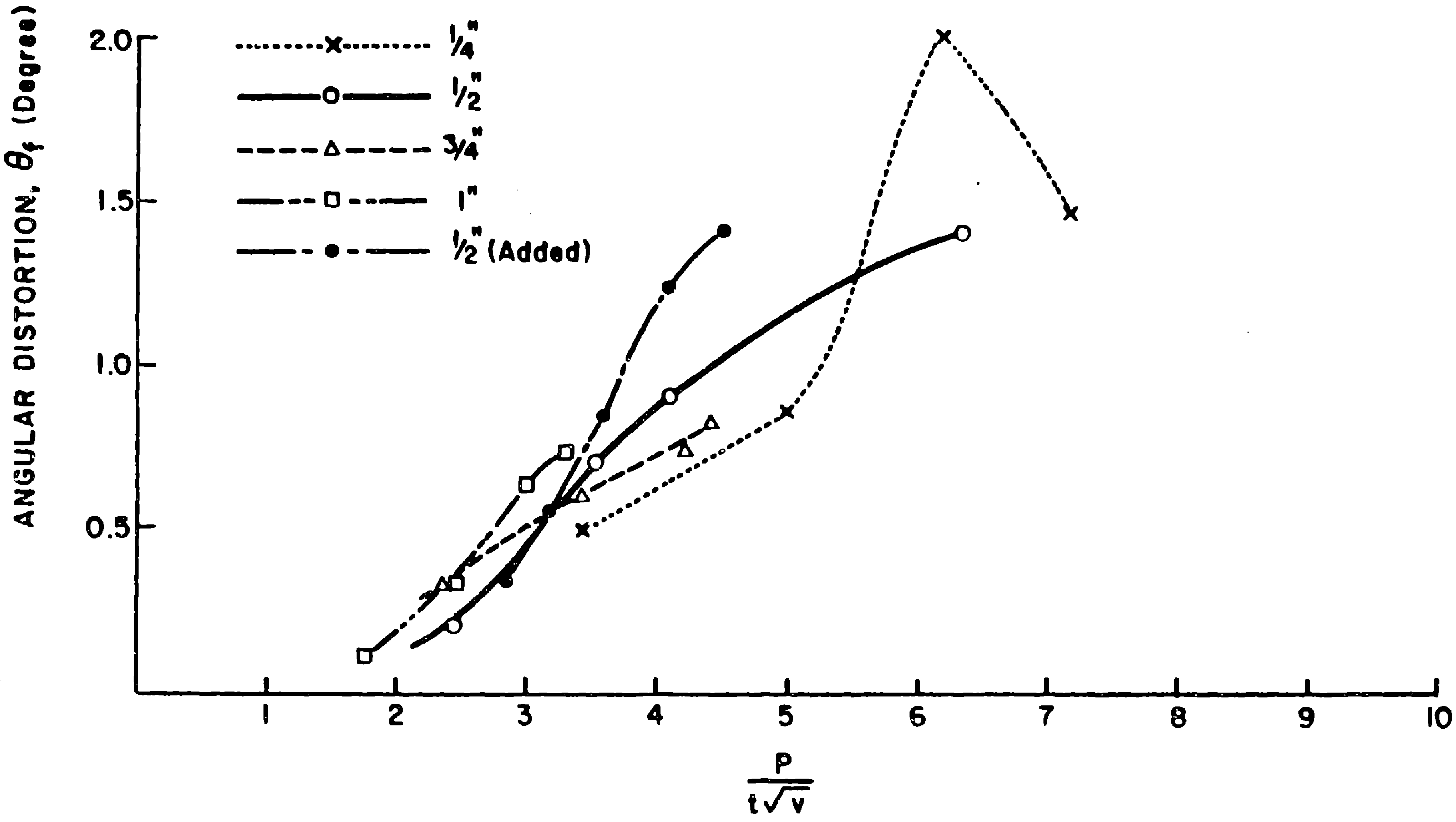

Figure 2.2-3: Results of Parametric Studies-P/t$\sqrt{V}$ vs. Angular Distortion

CHAPTER THREE

RESIDUAL STRESSES IN COMPOUND SHAPES FORMED BY LASER LINE HEATING

3.1 Introduction

It is a well-known phenomenon that any forming of a metal will impose residual stress in that metal. The failure of a component is often abetted if not caused directly by residual stresses. When no external load is applied nor any external restraint is present residual stresses can still be present. One cause of these residual stresses is a differential temperature in the metal. It is believed that the deflections resulting from line heating are caused by a combination of plastic and elastic behavior. Since residual stresses are limited by the yield strength of the material, a measurement of the residual stresses in a compound shape should indicate the relative contribution of elastic strain to the total deflection. Furthermore, for critical components where failure would cause the loss of the system, minimizing or removing residual stresses might be required. This is particularly true if the compound shapes are to be welded.

3.2 Theoretical Relationships

Metals are susceptible to residual stresses caused by uneven plastic strains. Masubuchi [6] developed some fundamental relationships for analyzing residual stresses in welds. Assuming perpendicular stresses are not significant the following development should apply to line heating. It should be recognized, however, that since the heating from a laser is localized to the surface of the plate, some through thickness residual stresses probably exist. The following derivation is taken from reference [6].

a. Total strain results from elastic and plastic components:

$$\varepsilon_x = \varepsilon_{x(e)} + \varepsilon_{x(p)}$$

$$\varepsilon_y = \varepsilon_{y(e)} + \varepsilon_{y(p)}$$

$$\gamma_{xy} = \gamma_{xy(e)} + \gamma_{xy(p)}$$

where ε_x, ε_y, γ_{xy} are components of the total strain

$\varepsilon_{x(e)}$, $\varepsilon_{y(e)}$, $\gamma_{xy(e)}$ are components of the elastic strain

$\varepsilon_{x(p)}$, $\varepsilon_{y(p)}$, $\gamma_{xy(p)}$ are components of the plastic strain

b. From Hooke's Law

$$\varepsilon_{x(e)} = 1/E(\sigma_x - \nu\sigma_y)$$

$$\varepsilon_{y(e)} = 1/E(\sigma_y - \nu\sigma_x)$$

$$\gamma_{xy(e)} = 1/G(\tau_{xy})$$

where E is Young's Modulus

G is the Shear Modulus

ν is Poisson's Ratio

c. Stresses must satisfy equilibrium conditions:

$$\partial\sigma_x/\partial x + \partial\tau_{xy}/\partial y = 0$$

$$\partial\tau_{xy}/\partial x + \partial\sigma_y/\partial y = 0$$

d. Total strain must satisfy compatibility:

Letting $E' = \frac{\partial^2\varepsilon_{x(e)}}{\partial y^2} + \frac{\partial^2\varepsilon_{y(e)}}{\partial x^2} - \frac{\partial^2\gamma_{xy(e)}}{\partial x\partial y}$

and $R' = -\left(\frac{\partial^2 \varepsilon_{x(p)}}{\partial y^2} + \frac{\partial^2 \varepsilon_{y(p)}}{\partial x^2} - \frac{\partial^2 \gamma_{xy(p)}}{\partial x \partial y}\right)$

Then $E' + R' = 0$ by compatibility.

If R' is non-zero (uneven plastic strain distribution), then elastic (residual) stresses must exist to satisfy compatibility. Implications of the above are:

(1) If plastic strains are linear with respect to displacement, no residual stresses occur.

(2) Residual stresses cannot be determined by measuring the stress change during external loading or unloading.

(3) Residual stresses $\sigma_x, \sigma_y, \tau_{xy}$ can be calculated if $\varepsilon_{x(e)}, \varepsilon_{y(e)}, \gamma_{xy(e)}$ are determined.

The residual stress is measured by measuring the change in elastic strain after cutting a specimen. Residual stresses can then be calculated using the following equations:

$$\sigma_x = -E/(1-\nu^2)(\varepsilon_x + \nu\varepsilon_y)$$
$$\sigma_y = -E/(1-\nu^2)(\varepsilon_y + \nu\varepsilon_x)$$

where the above strains are experimentally measured. By measuring the strains, at the same location, on both top and bottom of the specimen, one can determine the approximate contribution of planar and bending stresses to the total residual stress. The average of the strains through the plate will give the planar stresses. The difference in strains through the plate will give the contribution from bending.

3.3 Experimental Procedure

Twenty strain gages were attached to the sine curve fabricated as one of the experiments in reference [2]. A photograph and parameters used to make it is shown in Appendix A. Ten strain gages were placed on both sides at the same x-y coordinate. The plate is a 12" x 12" x 1/2" mild steel plate. Since the primary deflection is perpendicular to laser beam path (parallel to the y axis), the focus of the experiment was determining the residual stress in the x direction. Two gages per side were placed parallel to the beam path to determine if a "poisson" effect caused strain in the y direction. Figure 3.3-1 shows the plate geometry and gage placement.

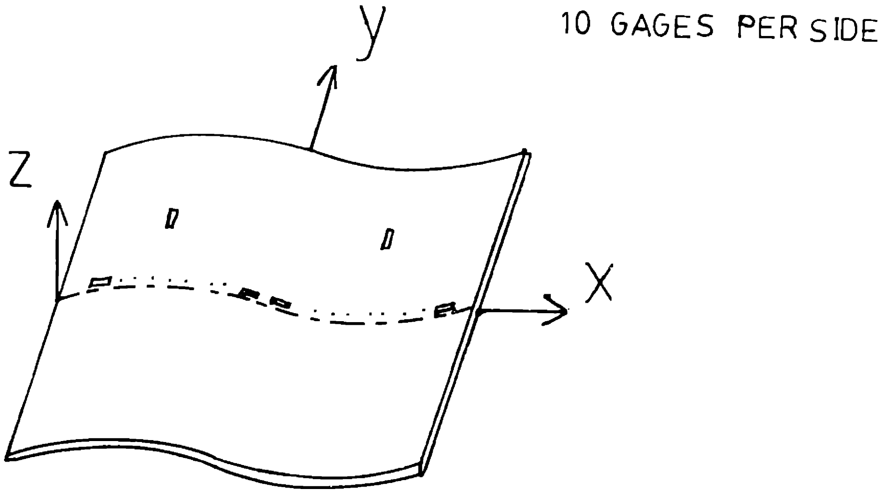

Figure 3.3-1: Placement of Strain Gages on the Sine Shape

All gages were BLH Electronics SR-4 type FAE-25-35-S6EL. Each had a gage factor of 2.02 ± 1%, a resistance of 350 ± .5 ohms. K had a value of +0.26 and the gage length was 6.35 mm (1/4 in) long.

A Vishay Instruments Model P-350A Digital Strain Indicator with two SB-1 Switch and Balance units was used to measure all strains. This instrument allows the measurement of ten strain gages per switch unit. One-half, full, or one-quarter balanced bridge circuits can be selected. For this experiment, the one-quarter bridge configuration was used. In this mode temperature effects can be automatically compensated by connecting an extra lead from one of the strain gage connections to an internal dummy resistor (350 ohm) within the strain indicator. A 5000 micro-strain (μin/in) internal calibrator and a gage factor input circuit allows the compensation of the measured resistances for the wire resistance.

Each strain gage is balanced to "zero" strain indication with the Switch and Balance unit prior to cutting the specimen. After cutting the specimen, the main indicator control is varied to rebalance the bridge circuit and the strain in microinches-per-inch is read directly off the Strain Indicator unit. Table 3.3-1 shows the major specifications of the Indicator unit [7].

Range	± 50,000 microinch/inch polarity reversible.
Sensitivity	Variable. Null meter deflects from zero to full scale with 40-4000 μin/in at gage factor = 2.
Readability	1μin/in.
Accuracy	±0.1% of reading or 5 μin/in whichever is greater for R=120 ohms, GF=2. ±0.3% of reading or 5 μin/in, whichever is greater for R=120 ohms, GF=1.5 to 4.5.
Gage Factor	Continuously variable from 0.1 to 10.0.
Bridge Excitation	1.5 VRMS at 1000 Hz square wave.

Table 3.3-1: Vishay Instrument Strain Indicator and Balance and Switch Unit Specifications

3.4 Experimental Results

Table 3.4-1 shows the results of strain measurements of the sine shape. Longitudinal spacing is relative to the y axis. Unless otherwise specified all gages are transversly placed relative to the y axis. Microstrain differences and averages are between the top and bottom of the specimen.

DIST. FROM CENTERLINE	MICROSTRAIN TOP	MICROSTRAIN BOTTOM	MICROSTRAIN DIFFERRENCE	MICROSTRAIN AVERAGE
-4	+121	+90	+30	+106
-3(LONG)	-182	-394	-212	-288
-3(TRANS)	-582	-458	-1040	-620
-2	-560	-620	-60	-590
-3/8	-245	-468	-223	-357
+3/8	-218	-440	-222	-329
+2	-136	-288	-152	-212
+3(LONG)	-462	-618	-156	-540
+3(TRANS)	-1498	+1359	-2857	-695
+4	-20	-180	-160	-100

Table 3.4-1: Experimental Measurements of Micro-Strain for the Sine Shape Formed by Laser Bending

At point x = -3 the ratio of strain in the longitudinal to transverse direction is: -182/-582 = 0.31. At point x = +3, the ratio is: -462/-1498 = 0.308. Both values are approximately poisson's ratio for steel ($\nu \equiv 0.3$) showing that bending of this plate in the direction parallel to the laser pass is primarily a "poisson" effect. This concept will be extremely important in the analyses of the deflections of the complex shapes and the subsequent development of the algorithms for them. Furthermore, on the basis of these results, the values of the elastic strain in the y direction at all points on the plate will be assumed to be: $\varepsilon_{y(e)} = \nu \cdot \varepsilon_{x(e)}$ during the residual stress calculations.

The residual stresses due to bending and planar effects now can be calculated using the following equations:

$$\sigma_x = -E/(1-\nu^2)(\epsilon_x + \nu \cdot \epsilon_y)$$

$$\sigma_y = -E/(1-\nu^2)(\epsilon_y + \nu \cdot \epsilon_x)$$

$\epsilon_x = \nu \cdot \epsilon_y$ (based on experimental evidence)

For steel: $E = 2.9 \times 10^7$ psi and $\nu = 0.3$. The equations become:

$\sigma_x = -6.37 \times 10^1(\epsilon_x)$ where ϵ_x is the measured

$\sigma_y = -1.16 \times 10^2(\epsilon_x)$ strain in μin/in.

Table 3.4-2 shows the residual stresses calculated from the experimental data given in Table 3.4-1 using the above equations. Figure 3.4-1 shows the results graphically.

DIST. FROM CENTERLINE	MICROSTRAIN DIFFERENCE	MICROSTRAIN AVERAGE	X-STRESS BENDING (KSI)	X-STRESS PLANAR (KSI)
-4	30	106	-1.91	-6.76
-3	-212	-288	13.5	18.4
-2	-60	-590	3.80	37.6
-3/8	-223	-357	14.2	22.8
+3/8	-222	-329	14.2	21.0
+2	-152	-212	9.69	13.5
+3	-156	-540	9.94	34.4
+4	-160	-100	10.2	6.37

Table 3.4-2: Bending and Planar Residual Stresses Determined for the Sine Shape Formed by Laser Bending

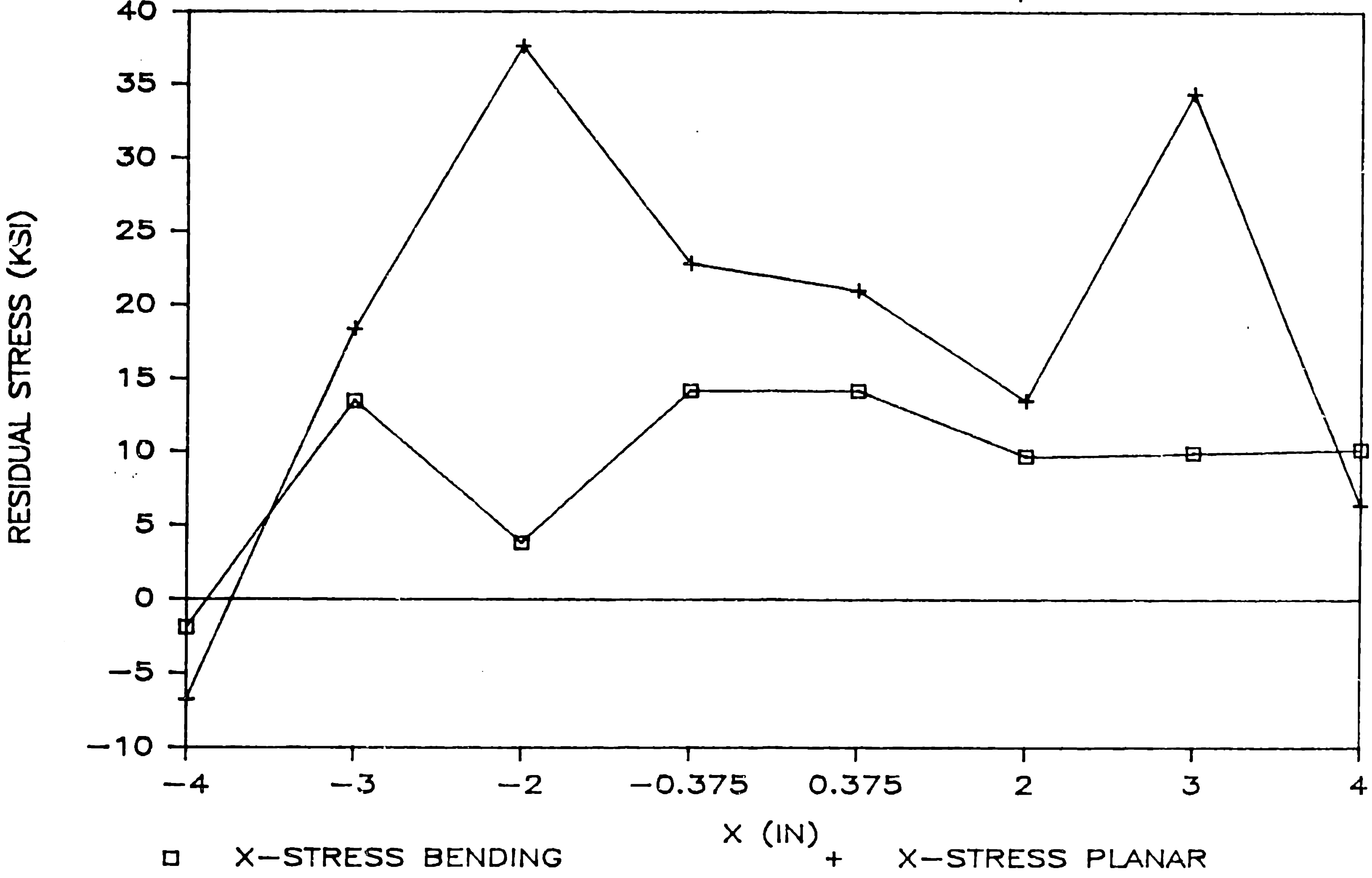

Figure 3.4—1: Bending and Planar

Residual Stresses for Sine Shape

The bending stress at x = +2 to the edge is approximately constant since the edge is clamped on that edge. The bending stress reaches a local minimum and the planar stress reaches a maximum at approximately the position of maximum magnitude of deflection where the rate of change of the deflection is a minimum. Therefore, for this shape, the bending residual stress is a minimum where the slope of the deflection (dz/dx) is a minimum. Likewise, the planar residual stress is a maximum where the magnitude of the deflection ($|z|$) is a maximum. Except for the region of external clamping of the plate, the bending stress is consistently less than the planar stress. The mean ratio between bending stress and planar stress for the positive deflection half-cycle ($X \leq 0$) is 0.43 and the mean ratio between bending stress and total residual stress is approximately 0.48. The fact that the bending residual stress represents about one-half of the total residual stress could indicate that significant changes in the magnitude of the deflection might occur if stress relieving is performed on the plate. Future experiments could confirm this hypothesis.

3.5 Summary and Conclusions

The results of the measurement of residual stresses in the sine shape appear to indicate the following:

a. The strain induced in the plate in a direction parallel to the laser pass is approximately poisson's ratio times the strain in the direction perpendicular to the heating path.

b. The bending residual stress is a minimum where the deflections are a maximum since the magnitude of the slope of the deflection is a minimum at that point. The planar residual stress is a maximum where the magnitude of the deflections are a maximum.

c. The bending residual stress constitutes, on the average, of about 50% of the total residual stress but varies on the plate from about 10% to about 80%.

d. Although clamping the plate appears to make uniform the bending stress distribution, clamping does not appear to affect significantly the planar stress more than about one beam diameter (~1.5 inch) away from the restraint.

e. The planar stress is approximately symetrical about the centerline of the plate less the effect from artificially restraining one side.

f. No local variance was visible in the planar stress due to multiple laser passes. This indicates that for overlapping or close proximity laser line passes, the stress is distributed about the plate in accordance with the geometry of the shape.

g. The highest y direction residual stress was observed to be about the yield strength of the metal (~65 ksi).

CHAPTER FOUR

PHASE II LASER LINE HEATING EXPERIMENTS

4.1 Introduction

This set of experiments was part of the second phase in the sequence whose objective is the development of a closed-loop controlled process for laser bending of steel plates. The specific goals of these experiments, conducted at Naval Research Laboratories, were:

a. Verification of and testing the reproducability of previously obtained data.

b. Increasing the data base by investigating the behavior of 3/8 and 5/8 inch thick mild steel plate.

c. Testing a simple linear algorithm for predicting the deflections for simple curves as a function of plate thickness and heat delivered to the metals surface.

d. Quantitatively Investigating the effect of multiple laser passes at different locations.

e. Investigating the effect of surface preparation on the deflections through multiple pass-single location experiments.

As discussed in Chapter 2, reference [1] discusses the deflection of steel plates as a function of the heat delivered to the metals surface. The power delivered to the metal's surface is represented by the following parameters:

$$P/\sqrt{V} \quad \text{or} \quad P/t\sqrt{V}$$

where P is the laser power delivered to the metal, t is the plate thickness, and V is the bedplate/steel speed beneath the laser.

It is anticipated that even if the process of laser bending steel plates to produce complex shapes is controlled by a closed-loop system, initial bending to within twenty to thirty per cent of the final shape will be governed by the data base and/or developed algorithms. Final shaping and dewarping would be monitored by the optical laser/video system. A major goal of these experiments was to test a simple, linear algorithm to predict the one dimensional deflection of plates with thicknesses not previously within the data base. To examine the reproducability of this process, the deflections of 1/2 inch thick plate were measured and compared to that obtained during Phase I experiments.

Since the completed system/process may require multiple passes at the same or different locations on the plate, both multiple pass-single location (MPSL) and single pass-multiple location (SPML) experiments were conducted. It was expected that fundamental question would be answered concerning any interaction of passes from one location to another and interactions of multiple passes at the same location.

4.2 Experimental Procedure

In order to minimize the number of variables and to simulate a probable industrial environment, generated laser power was held constant at 7 kW with a beam diameter of about 1.5 inches. Beam spot geometry was the "top hat" discussed in reference [2]. Variation of the heat linear density delivered to the metal was accomplished by varying the plate speed past the stationary laser beam. No complex shapes were created in this series of experiments. Beam path locations were predetermined on the basis of:

a. Maximizing beam pass separation when independent measurements were desired and controlling the separation distance during SPML studies.

b. Obtaining no effects from the plate's edge parallel to the travel direction.

c. Allowable clearances on the bedplate mechanism with the steel plate.

All experiments were performed with 24" x 36" K-TEN20CF steel plates. Each was spray painted black. No clamping or forced cooldown was done. Deflections were measured with three dial gages of which two were placed on one side of the beam pass. Deflections were taken periodically during cooling until no change was observed (about 20 minutes per pass). Figure 4.2-1 shows the arrangement for a typical experiment.

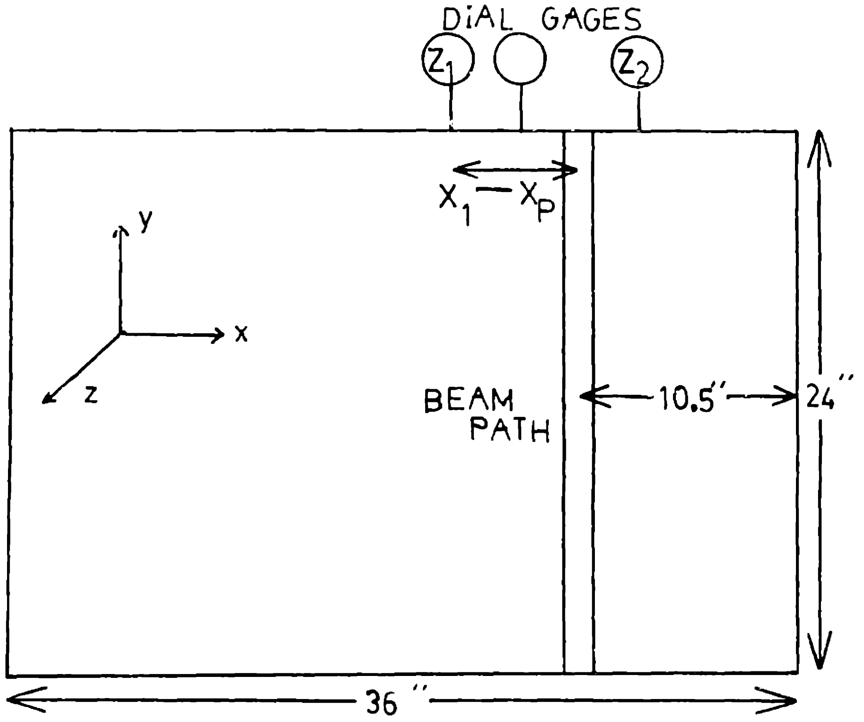

Figure 4.2-1: Typical Arrangement for Phase II Experiments Conducted at N.R.L. (September 1985)

4.3 Experimental Results

The three dial gage readings were plotted and, assuming the minimum deflection to be at the centerline of the pass, the angular deflection on both sides of the pass was determined from:

$$\theta_{1,2} = \mathrm{Tan}^{-1}\left[\frac{Z_{1,2} - Z_{1,2}\mathrm{min}}{X_{1,2} - X_p}\right]$$

$$\theta_f = \theta_1 + \theta_2$$

where $Z_{1,2}$ are the measured deflections at coordinate $X_{1,2}$, X_p is the coordinate of the centerline of the pass, and θ_f is the final total angular deflection.

For an ideal plate, the minimum deflection at the centerline of the beam pass, $Z_{1,2}min$, should be zero. In reality, deflections parallel to the beam path are superimposed on the plate resulting in a uniform (except at the edges) raising of the plate. This is probably due to the longitudinal residual stresses discussed in Chapter Three. Since only x direction deflections are desired, this overall plate translation in the z direction was removed by subtracting the minimum value which was found to be consistently greater than zero. The algorithms for complex shapes developed in the next chapter will include this effect.

The linear algorithm assumes that θ_f is a linear function of $P/\sqrt{V}$ between any 2 adjacent, previously determined data points. Furthermore, it assumes θ_f is a linear function of the thickness for a given $P/\sqrt{V}$ between any two adjacent thicknesses. Deflection angles for 3/8" thick plate was predicted using values of θ_f for 1/4" and 3/8" plates from figure 2.2-1 or table 2.2-1. 1/2" thick plate was subjected to values of $P/\sqrt{V}$ not previously within the data base although they are shown graphically in figure 2.2-1. Values of θ_f were predicted on the basis of linearity between bracketing values of θ_f within the data base (table 2.2-1). This was done to test the linearity of the curves within neighborhoods of the preexisting data and to test the reproducability of the process. Finally, 5/8" thick plate was subjected to three different $P/\sqrt{V}$ and the deflection angles measured. Table 4.3-1 gives the results of these experiments and the predicted values for 3/8" and 1/2" plates. Figures 4.3-1 and 4.3-2 are graphs of these measurements superimposed upon the results from Phase I experiments.

THICKNESS	$P/\sqrt{V}$	$P/t\sqrt{V}$	θ ACTUAL	θ PRED.
3/8"	1.28	3.41	0.28	0.50
	1.49	3.98	0.86	1.19
	1.75	4.67	1.23	1.20
	2.21	5.90	1.66	1.25
1/2"	1.49	2.98	0.47	0.42
	1.75	3.50	0.73	0.70
	2.21	4.43	1.04	1.02
5/8"	1.49	2.39	0.38	
	1.75	2.80	0.82	
	2.21	3.54	0.98	

Table 4.3-1: Test Results Obtained in Parametric Studies Conducted September 1985

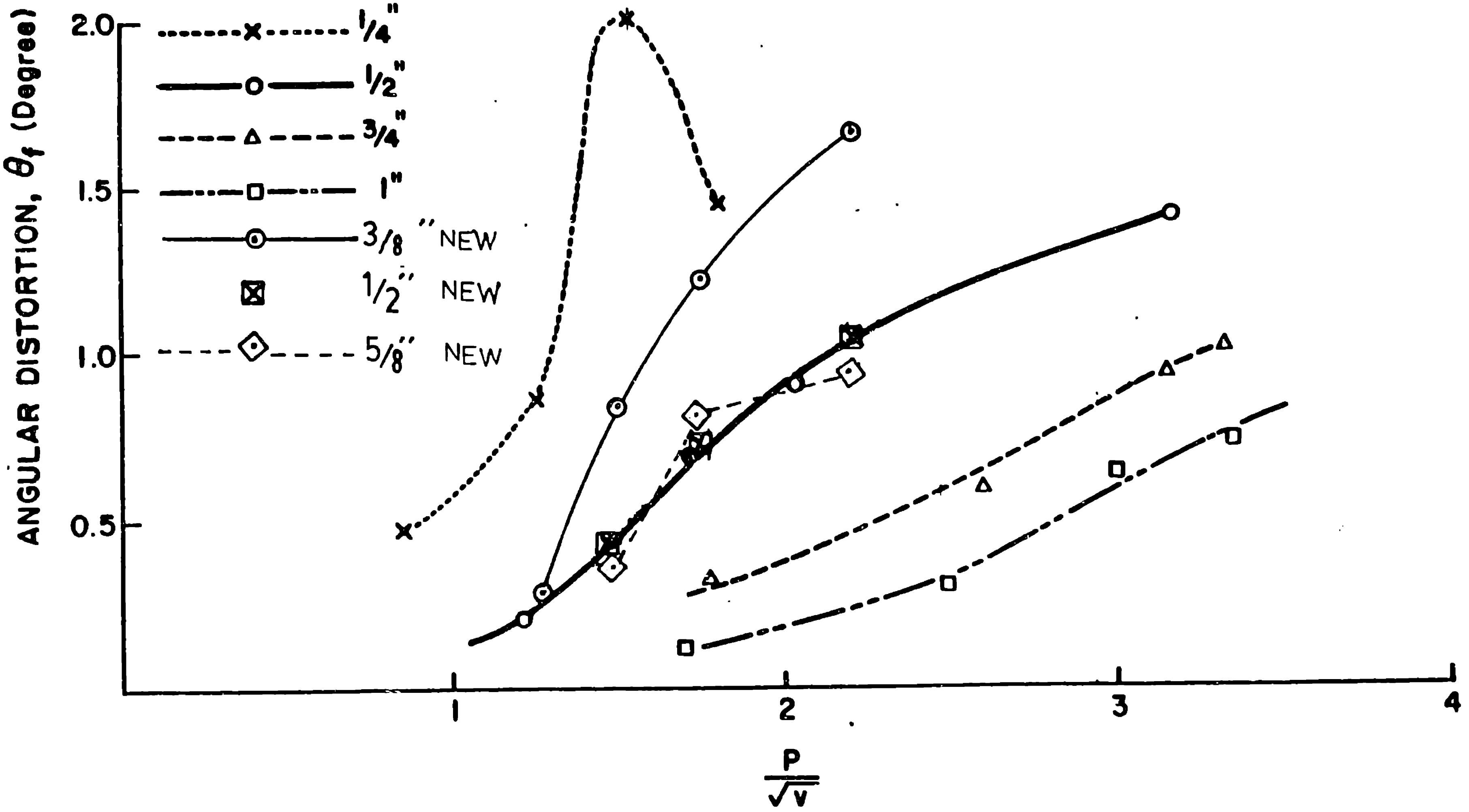

Figure 4.3-1: Results of Parametric Studies of September 1985
P/√V vs. Angular Distortion

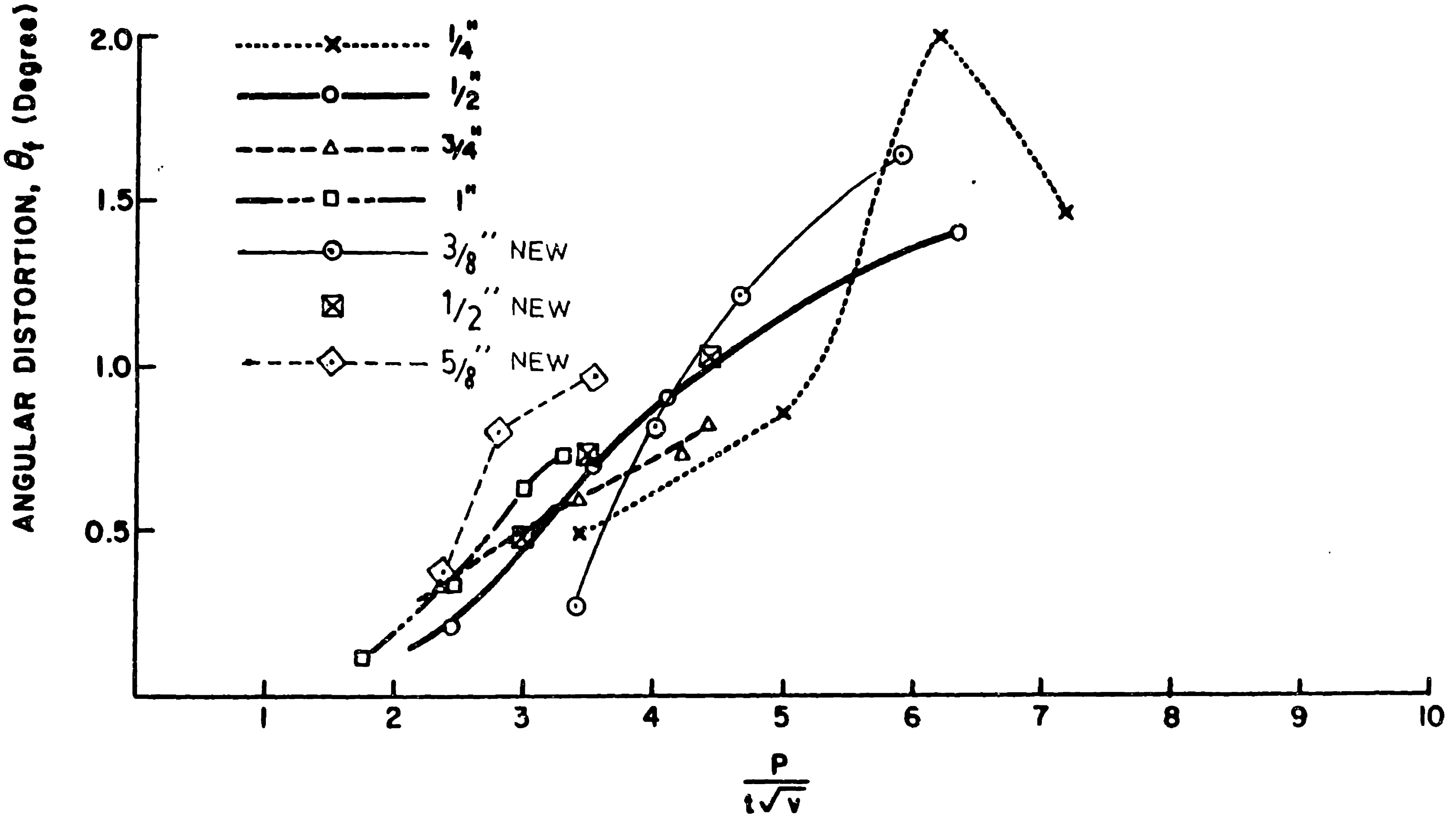

Figure 4.3-2: Results of Parametric Studies of September 1985 P/t$\sqrt{V}$ vs. Angular Distortion

On the basis of the experimental results, one can observe:

a. The close agreement between the previous and current results for the 1/2" plate indicating the reproducability of the process.

b. For 1/2" plating, a linear algorithm predicting deflections between data points previously obtained is reasonably accurate.

c. 1/4" plating should not be used to linearly predict the behavior of plates with a different thickness.

d. The measured deflection angles for the 5/8" plating were consistently higher than expected with or without the use of a linear algorithm. For this reason, it is recommended that additional experiments be performed on 5/8" plating prior to the integration of these results into the data base.

Experiments were performed to determine the effect of multiple passes on the same plate. $P/\sqrt{V}$ was held constant at 1.278 and the plate thickness was 3/8". The results are given in table 4.3-2. The cumulative (total) deflection angle as a function of the number of passes is shown in figure 4.3-3. The results show that for as little separation as one beam diameter (~1.5 inches) between passes the deflection is approximately constant. This implies that under the conditions of this experiment, superposition of angular deflection is a reasonable assumption in SPML mode.

PASS	DIST. TO NEAR. PASS (inches)	DIST. TO NEAR. END (inches)	θ_f (degrees)
A	-	10.5	.24
B	20.5	5	.23
C	5.75	10.8	.23
D	5.75	16.3	.38
E	3.0	13.5	.33
F	2.88	7.88	.31
G	1.50	7.25	.33

Average Angular Deflection Per Pass is 0.3 Degrees

Table 4.3-2: The Effect of Pass Separation Distance on the Angular Deflection of 3/8" plate with $P/\sqrt{V} = 1.28$

Figure 4.3–3: Number of Passes vs.
Angular Deflection (t=3/8", $P/\sqrt{V}=1.28$)

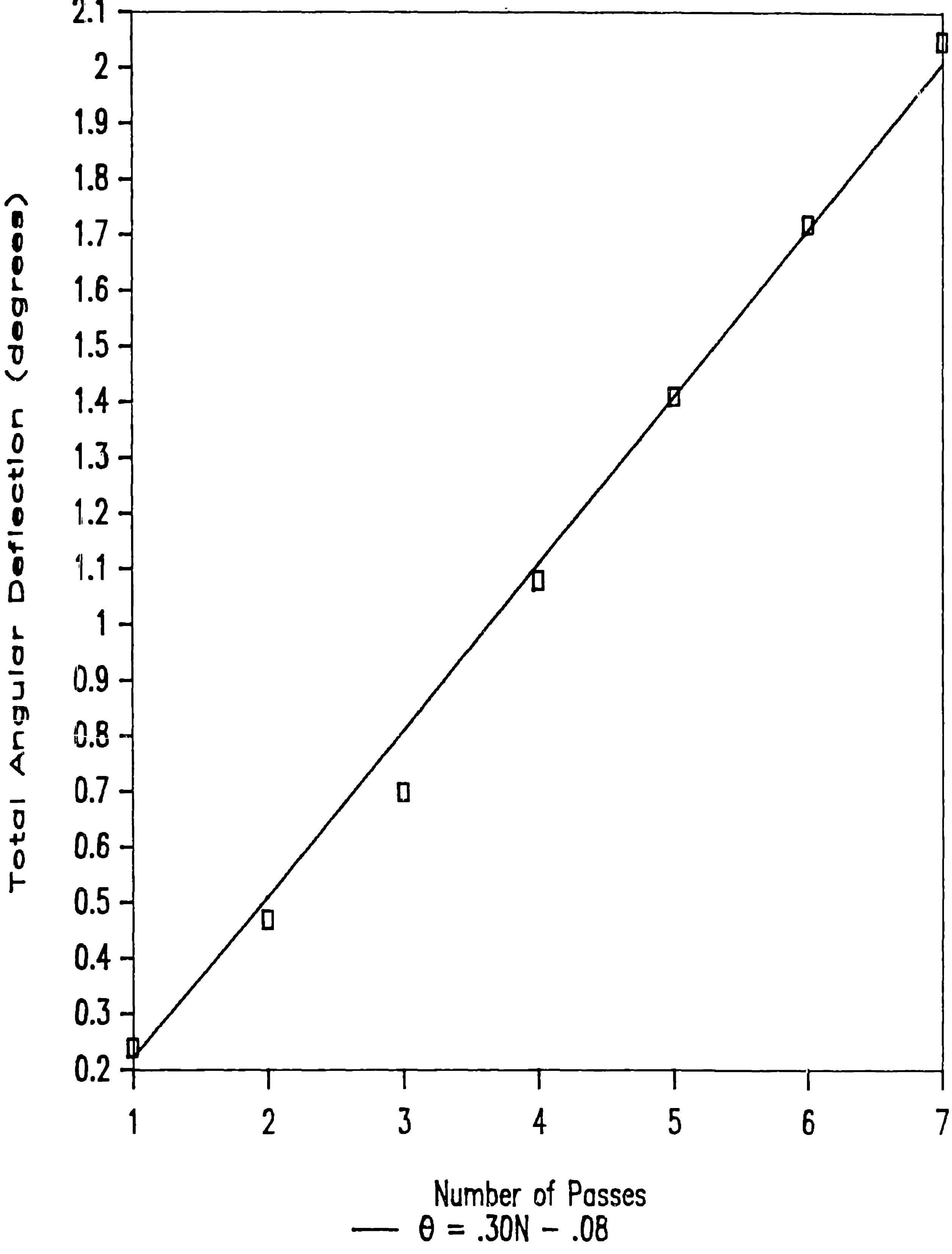

The last series of test in this sequence indicated that, without surface preparation (painting) after each pass in the MPSL mode, no significant deflection occurs after the initial pass. It should be emphasized that in these experiments the plate was allowed to cool to ambience after each pass. Since the absorption of ~10 micron radiation by a metal increases rapidly with increasing plate temperature, multiple passes at a single location might indeed cause significant deflection if the material is not allowed to cool significantly prior to the next pass. Further investigations of the effects of surface preparation are recommended. This should include, at a minimum, the use of alternative preparations such as white titanium oxide which is frequently used in laser scattering experiments and should include the MPSL processing without cooling after each pass.

4.4 Summary

The results of the series of Phase II experiments conducted at Naval Research Laboratories in Washington, D.C. contribute to the understanding of the behavior of metals when subjected to laser line heating. They also provided valuable data in the development of a closed loop control system. Specifically:

a. Results for 1/2" plating were verified showing the reproducability of the process.

b. Multiply located passes on the same plate cause deflections which are approximately linear with respect to the number of passes. This was confirmed using K-TEN20CF with beam path separation to as low as one beam diameter.

c. If no surface preparation is performed and the plate is allowed to cool to room temperature after each pass in the MPSL mode, no measurable deflection occurs after the first pass.

d. A linear algorithm is sufficient to predict deflections for a given thickness at power densities not within the data base. A linear algorithm using 1/4" data for predicting behavior of plates of other thicknesses is inaccurate.

Sufficient predictability and control has been shown to give encouragement that development of a closed loop laser bending system is practicable for simple shapes.

CHAPTER FIVE

AN ALGORITHMIC APPROACH TO PREDICTING DEFLECTIONS IN A COMPLEX SHAPE

5.1 Introduction

Very elaborate techniques have been developed or applied to the prediction of the behavior of metals undergoing line heating. In spite of this, to date, there exists no algorithm based on either engineering physics or a data base which can synthesize a complex, three dimensional shape. Recalling the discussion in Chapter Two about the overall goals of present research in laser bending, algorithms will be essential for automating a shape synthesizing process using line heat. This is also probably true for automating a metal straightening (dewarping) process. This is equally true for laser and flame line heating.

The "purest" algorithms are those which are based on a thorough understanding of the physics of the technique including the mechanisms of behavior of the object in question. This approach is usually possible only for simple systems where there are few primary variables. Even then, the use of very powerful computers or experimental equipment is often required. Any algorithmic based or assisted automated technique requiring the use of a main frame computer will probably not be cost effective for a manufacturer such as a shipbuilder.

The other major approach is to base the algorithm on empiracal data. This approach is often preferable to the "physics" approach since it allows the development of a process with potentially many primary variables and an incomplete knowledge of the science of the phenomenon. A main disadvantage of this approach is that it may be more expensive to develop the algorithm because of the number of experiments required to create a sufficiently large data base. In the long run, for producing an automated process for shaping steel by thermomechanical means, the later approach is best since it will reduce the complexity and cost of the hardware in the complete system. In fact, it is not unreasonable to strive for a system whose control system is maintained and driven by a microcomputer. Therefore, the algorithms should be as simple and compact as possible.

The main objective of this development is not to produce the most elaborate, comprehensive, or sophisticated algorithm for laser bending steel plates into complex shapes. Rather, it is to prove that simple linearized algorithms can be constructed which will produce with reasonable accuracy those shapes. Furthermore, these algorithms must be based on preexisting information on simple, single pass deflections already within the data base. Although the data base for simple angular deflections is substantial, the number of preexisting complex shapes is not. Therefore, it is fully expected that, as more experiments are performed on complex shapes and as more analysis is performed on the mechanisms of bending in response to line heating, the algorithms will be modified to become more general and more accurate. This paper develops one algorithm for each of the shapes considered. These are the parabaloid (dish), the parabolic hyperboloid (saddle), the cone, and the antisymmetric double paraboloid ("sine").

5.2 General Methodology

The algorithms created in this chapter are empirically based on only one sample of that particular shape. Although a strenuous attempt was made to include known physical phenomena, on occasion, underivable factors had to be included which may or may not remain the same for the same shapes constructed under different conditions. The same methodology was applied to the different shapes whenever possible. Linearity was assumed whenever excessive loss of accuracy did not result. Symmetry was determined from geometric properties of the shapes. A photograph of each of the analysed shapes is included in Appendix A. These are extracted from reference [2]. Also included with the photograph is a sketch of the pattern of laser passes and relevant parameters used to construct the shape. The deflections at specific points on the shape were measured with a dial gage. All data was compensated for the thickness of the plate and was normalized such that the deflection at the center of the plate (x,y = 0) was numerically zero. The coordinate system is cartesian with the center of the plate the center of the coordinate system. The width of the plate in the "x" direction is notated W_x and the width (height) of the plate in the "y" direction is notated W_y. Unless otherwise noted, the "top" of the plate is that side such that the laser path is in the +y to -y direction. For a perfectly continuous pure geometric shape, the entire shape can be generated by functions for the x = 0 and y = 0 contours. Figure 5.2-1 shows how the saddle shape can be generated with only the contours of x = 0 and y = 0 analytically determined. Throughout this chapter "z(x,y)" will represent the deflection at point (x,y) and z(0,y) and z(x,0) will represent the components of the deflection from the x = 0 and y = 0 contours, respectively.

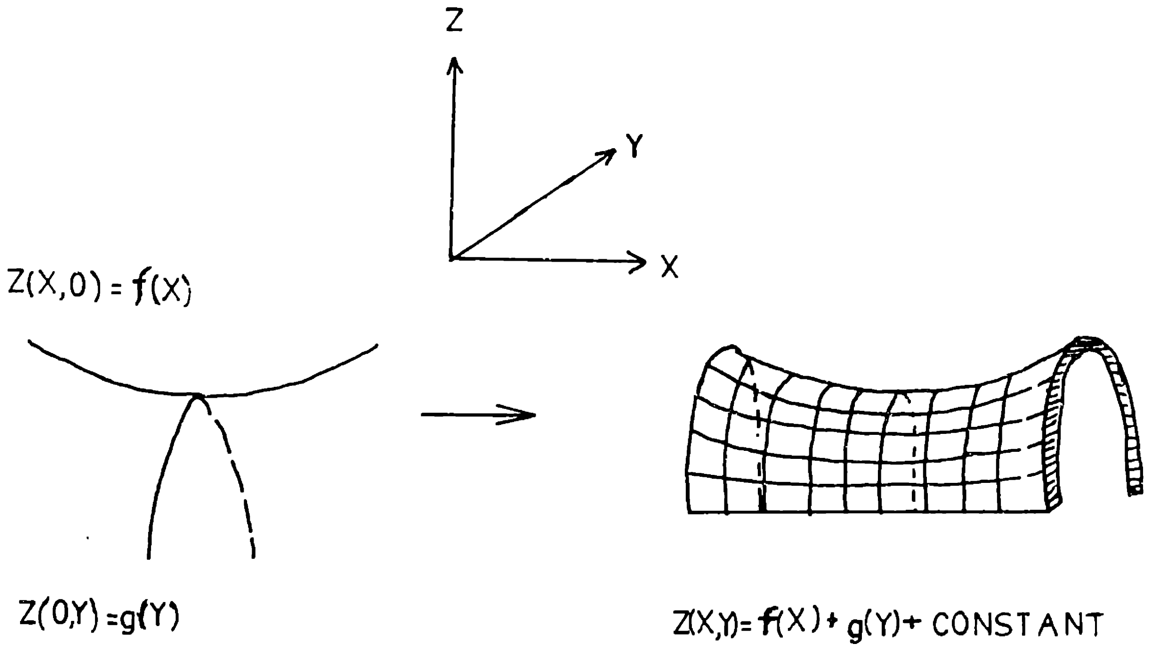

Figure 5.2-1: 3 Dimensional Shape Generated from Contour Lines

The total deflection at a point (x,y) is:

$$z(x,y) = f(x)|_{y=0} + g(y)|_{x=0} + \text{constant}$$

Since the curve is normalized such that $z(0,0) = 0$ the above constant is zero and:

$$z(x,y) = f(x)|_{y=0} + g(y)|_{x=0} \text{ or}$$

$$z(x,y) = z(x,0) + z(0,y).$$

Geometric symmetry simplifies algorithm generation. For example, geometric symmetry predicts for the perfect bowl and saddle: $z(x,y) = z(-x,y) = z(x,-y) = z(-x,-y)$;

For the sine shape: $z(x,y) = -z(-x,y)$;

For the cone shape: $z(x,y) = z(-x,y)$ only.

The above relationships are valid only if the center of the coordinate system is at the center of the shape as is assumed for all the analysis herein.

The actual complex shapes were prepared in such a way as to try to maintain the symmetry. This was done by the choice of beam pattern and the equality of laser irradiation. However, when the shapes were analyzed it was found that the symmetry was not always preserved. This could be due to uneveness in surface preparation or plate thickness, irregularities in laser power or bed plate speed, or unequal edge effects. These deviations of the real plates geometry from the ideal geometric shape can be categorized as:

a. Warping: Lack of fairness or smoothness for a particular z-contour line.

b. Asymmetry along an entire contour line or surface.

Figure 5.3.1(a)-1, which will be discussed in a later section, shows examples of both types of irregularity. Geometry and the pattern of laser passes should cause us to predict that for a given y = k line the deflection at +x is equal to the deflection at -x. However, the deflections in the $y \geq 0$, $x \geq 0$ quadrant appear consistently greater that the values in the $y \geq 0$, $x \leq 0$ quadrant. Warpage is also evident for the y = 5 line and from x = -3 to x = -4 on the y = 1 line. For all the shapes the edge effects are somewhat erratic. The dish was irradiated in such a way to minimize edge effects. Nonetheless, it still appears in several of the contour lines. For some of the other shapes not fabricated to minimize end effects the edge effects may or may not be considerable.

Due to these irregularities, the following general methodology was used to analyze the shapes:

a. The raw (actual) deflections were normalized such that z(0,0) = 0.

b. Using a fairing process with splines commonly used in naval architecture to smoothe hull shapes, the contour lines were "dewarped". This process was performed such that the deflection was the same value at a point (n,k) approached from both a y = k and a x = n contour.

c. Deflections were averaged in such a way as to obtain geometric symetry predicted from the ideal curve.

d. The dewarped, symmetrized shape, called the model shape, (Z_m), was then used to generate the algorithm (Z_a). Although for each of the shapes the algorithmically determined deflections (Z_a) are compared with the measured values, the goal was to construct the modeled (dewarped and symmetrized) deflections (Z_m) to within about 10 % accuracy. This procedure can be justified by the fact that plate warpage and lack of complete symmetry always cannot be controlled or predicted using a real process. Secondly, these algorithms are designed to initialize the automated process. That is, these algorithms should be capable of obtaining "in the ball park" deflections. It is assumed that the closed loop feedback system will be capable of fine tuning the shape which would include dewarping and symmetrizing the shape as required by the application of the shape. It is estimated at this time that approximately 70 to 85 % of the desired shape's deflection will be obtained by use of the algorithm and/or the data base. The remaining deflection will be controlled by the feedback system.

The process of constructing the model shape consists of using the single pass θ_f (as a function of $P/\sqrt{V}$) from reference [2], the number and pattern of laser passes, generalized effects from the edges, near-pass coupling effects and, as required, correlating factors to generate the $y = 0$ and $x = 0$ contours. These contours are then used to predict the deflection at any given point within the plate in the manner described above.

The slopes of the x = 0 and y = 0 model contours were not constant. In most of the shapes the contours were divided into three regimes with their own governing equations. These regimes are the flattened area near the maximum or minimum, the edge and corresponding nearby region, and that portion between the other two regimes. In several cases the last two regimes had the same slope and were then considered to have two regimes. To improve the accuracy near the origin where flattening of the shape was prominent, a single point deflection is predicted half-way between the origin and the borderline between regime one and two.

Some method had to be developed which would correlate the angular deflection within the data base for a single laser pass, the number of passes on that portion of the plate and a factor accounting for beam path coupling effects and edge effects which were distributed over all the plate. Defining "k" to be the distributed angular deflection:

$$k = \frac{n \cdot \theta_f \cdot [W_x - (1+\nu) \cdot B.D.][W_y - (1+\nu) \cdot B.D.]}{2 \cdot W_x \cdot W_y} \text{ where}$$

n is the number of laser passes on that line or plane of symmetry;

θ_f is the angular deflection (Figure or Table 2.2-1);

W_x and W_y are the widths of the plate;

B.D. is the beam diameter;

ν is poisson's ratio.

For steel with the laser beam diameter of 1.5, $(1+\nu)$B.D. is approximately equal to 2. The equation becomes:

$$k = \frac{n \cdot \theta_f \cdot (W_x - 2)(W_y - 2)}{2W_xW_y}$$

The factor of two above comes from the definition of θ_f. The distributed deflection slope is given by:

$\Delta z/\Delta q = \mathrm{Tan}(k)$ where q is the generalized coordinate.

For example, a 1/2" thick plate with width of 24" and height of 18" is symmetrically irradiated with 20 passes on one side to produce a dish. The beam power is 6.3 kW including optical losses and bed plate/steel speed is 12 ipm. Then $P/\sqrt{V} = 2.02$ and from table 2.2-1, $\theta_f = 0.90$. From the above equation:

$$k = (20)(0.9)(22)(16)/(2)(24)(18) = 7.33^{\circ}$$

$$\mathrm{Tan}(k) = \mathrm{Tan}(7.33^{\circ}) = 0.1286 = \Delta z/\Delta q$$

The distributed deflection angle is the basis of the algorithms of all the shapes. $Z_a(x,0)$ and $z_a(0,y)$ are assumed to be functions of the Tan(k) parameter. It should be stated at this time that the Tan(k) parameter is more accurate than superposition $(n \cdot \theta_f/2)$ for three dimensional curvature with many passes. However, for simple one dimensional passes such as those described in chapter four and references [1] and [2], superposition appears to be more accurate.

5.3 Shape Analysis and Algorithm Generation

5.3.1 Dish Shape

a. Derivation of the Model and Algorithm

The dish shape was produced by irradiating a plate on one side longitudinally, transversely, and diagonally to the $y = 0$ coordinate line. This pattern is shown in Appendix A with relevant plate and heating parameters. Table 5.3.1-1 gives the measured and normalized (raw) deflections and figures 5.3.1-1 to 4 are graphs of the measured data.

Using the fairing and symmetrizing procedure described in the previous section, model contours are produced. Table 5.3.1-2 and figure 5.3.1-5 show the model deflections.

Recall that the distributed deflection slope is given by:

$$\Delta z/\Delta q = \tan(k) = \tan[n\theta_f(W_x-2)(W_y-2)/2W_xW_y]$$

For this dish: $n = 30$; $W_x=W_y=10"$; $\theta_f \equiv 0.7$ which gives

$$k = 6.72^\circ \text{ and } \tan(k) = \tan 6.72^\circ = 0.1178$$

Since the geometry of the dish which was used to generate the model has x/y symmetry, the $y = 0$ and $x = 0$ contours are the same curve. Using this fact and the value of tan(k) above, the following equations can be used to construct the model dish.

X	Y=-5 DEFL	Y=-4 DEFL	Y=-3 DEFL	Y=-2 DEFL	Y=-1 DEFL	Y=0 DEFL
-5	0.929	0.757	0.637	0.500	0.441	0.298
-4	0.794	0.643	0.505	0.361	0.277	0.235
-3	0.646	0.494	0.342	0.224	0.136	0.140
-2	0.521	0.419	0.291	0.152	0.065	0.065
-1	0.481	0.363	0.205	0.078	0.025	0.020
0	0.350	0.262	0.205	0.073	0.010	0.000
1	0.411	0.277	0.202	0.085	0.044	0.024
2	0.602	0.383	0.254	0.187	0.112	0.089
3	0.732	0.491	0.372	0.301	0.227	0.215
4	0.854	0.710	0.573	0.452	0.392	0.371
5	1.097	0.890	0.673	0.575	0.485	0.462

X	Y=0 DEFL	Y=1 DEFL	Y=2 DEFL	Y=3 DEFL	Y=4 DEFL	Y=5 DEFL
-5	0.298	0.333	0.395	0.503	0.609	0.823
-4	0.235	0.245	0.290	0.397	0.535	0.787
-3	0.140	0.185	0.187	0.286	0.440	0.597
-2	0.065	0.069	0.117	0.205	0.336	0.472
-1	0.020	0.018	0.069	0.186	0.310	0.462
0	0.000	0.006	0.065	0.153	0.278	0.395
1	0.024	0.030	0.070	0.177	0.298	0.416
2	0.089	0.100	0.135	0.253	0.359	0.525
3	0.215	0.227	0.252	0.357	0.481	0.611
4	0.371	0.387	0.415	0.515	0.587	0.719
5	0.462	0.473	0.531	0.590	0.715	0.839

Table 5.3.1-1: Measured and Normalized Raw Deflection Data for the Dish Shape

Figure 5.3.1—1: Raw Deflection Data

for the Dish Shape (y≥0)

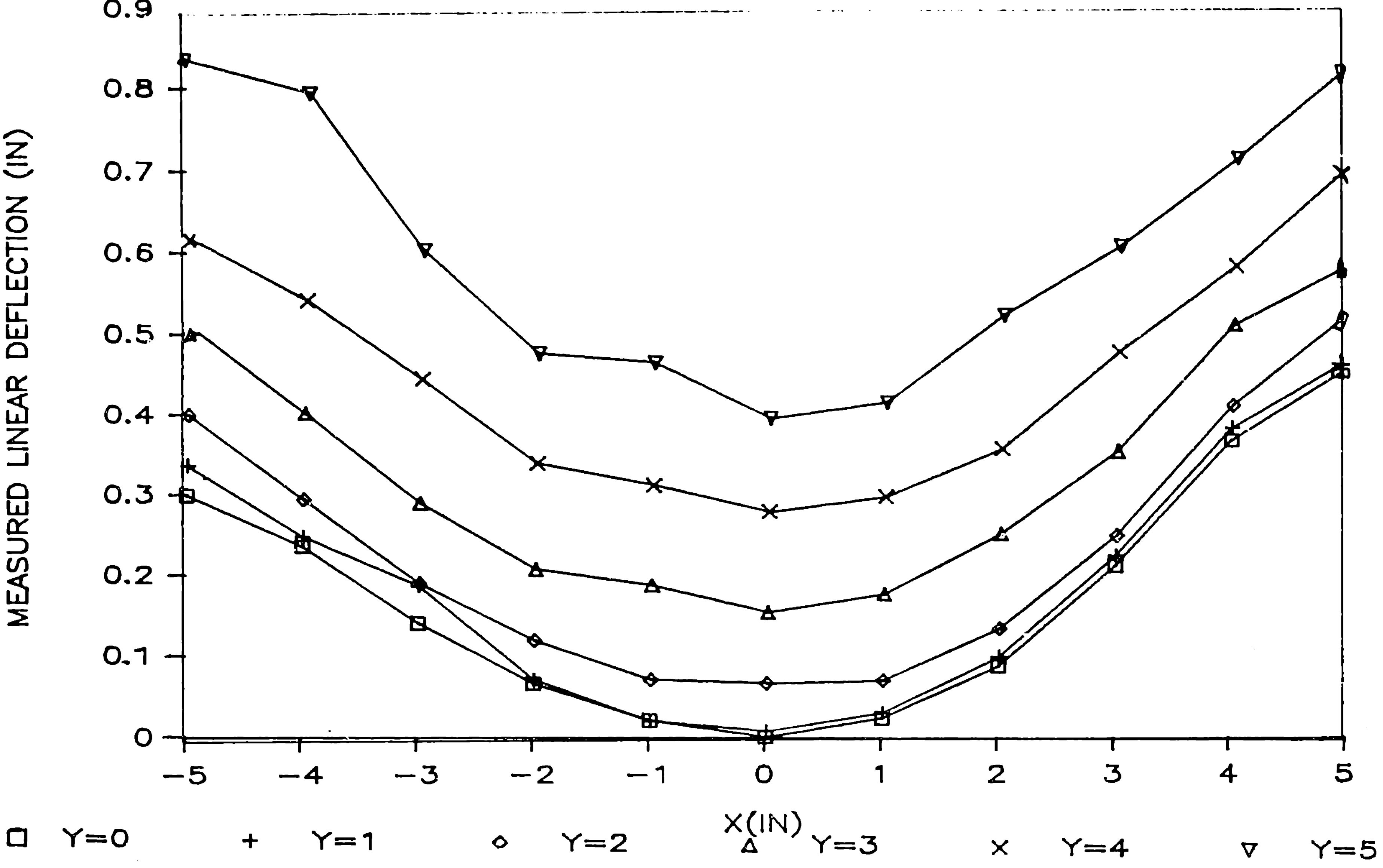

Figure 5.3.1—2: Raw Deflection Data

for the Dish Shape (y≤0)

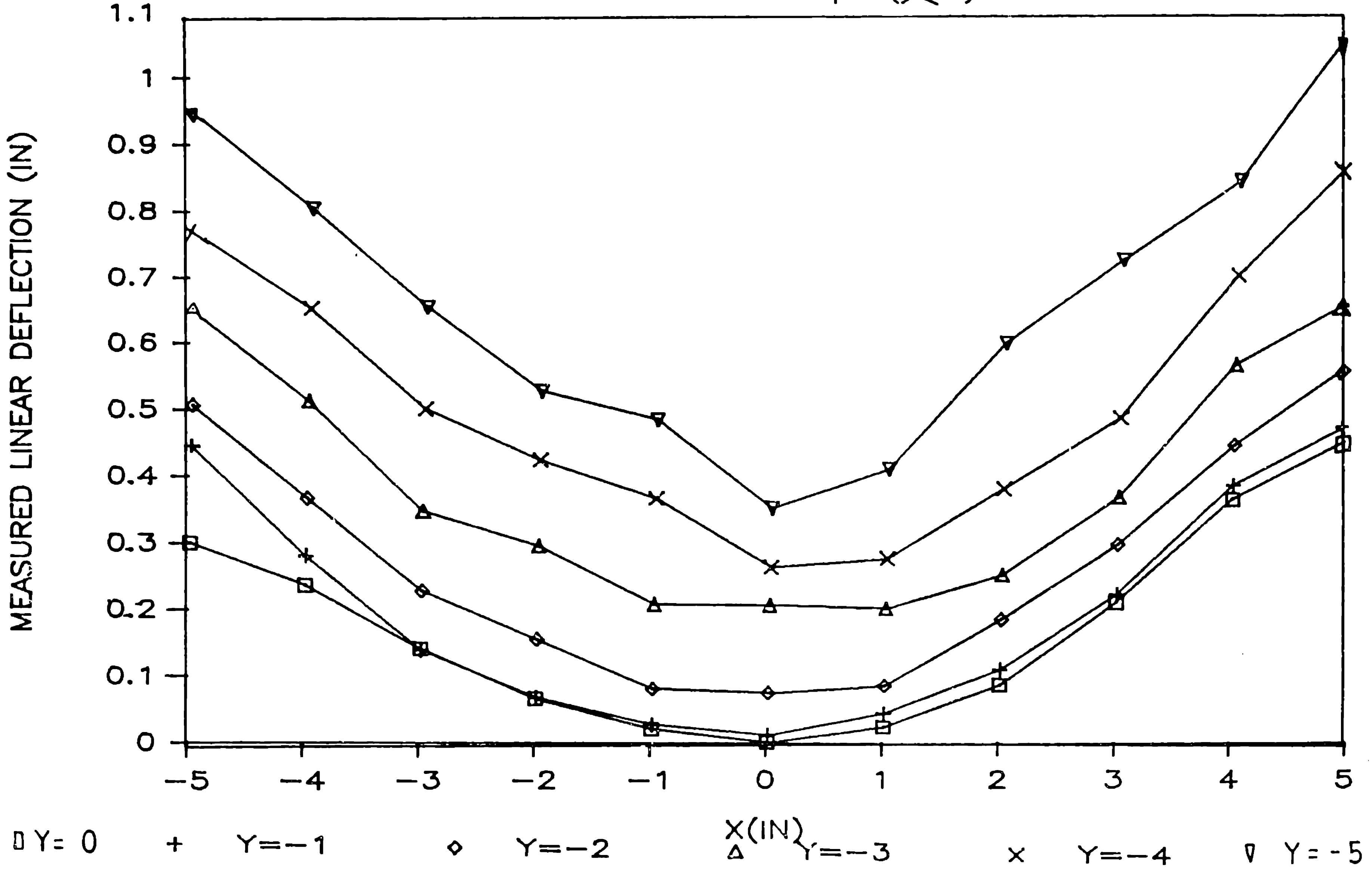

Figure 5.3.1—3: Raw Deflection Data
for the Dish Shape (X≥0)

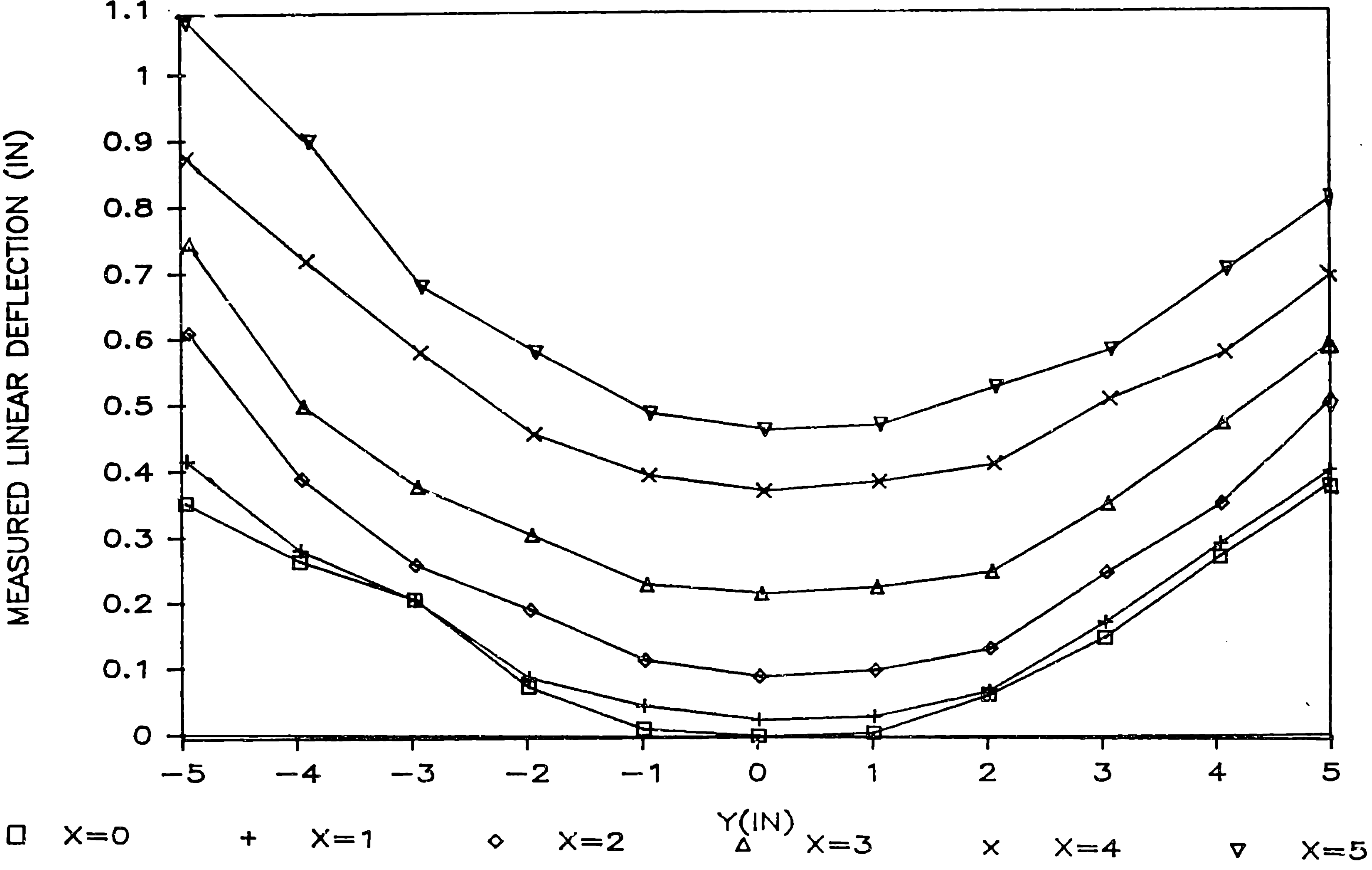

Figure 5.3.1—4: Raw Deflection Data

for the Dish Shape (X≤0)

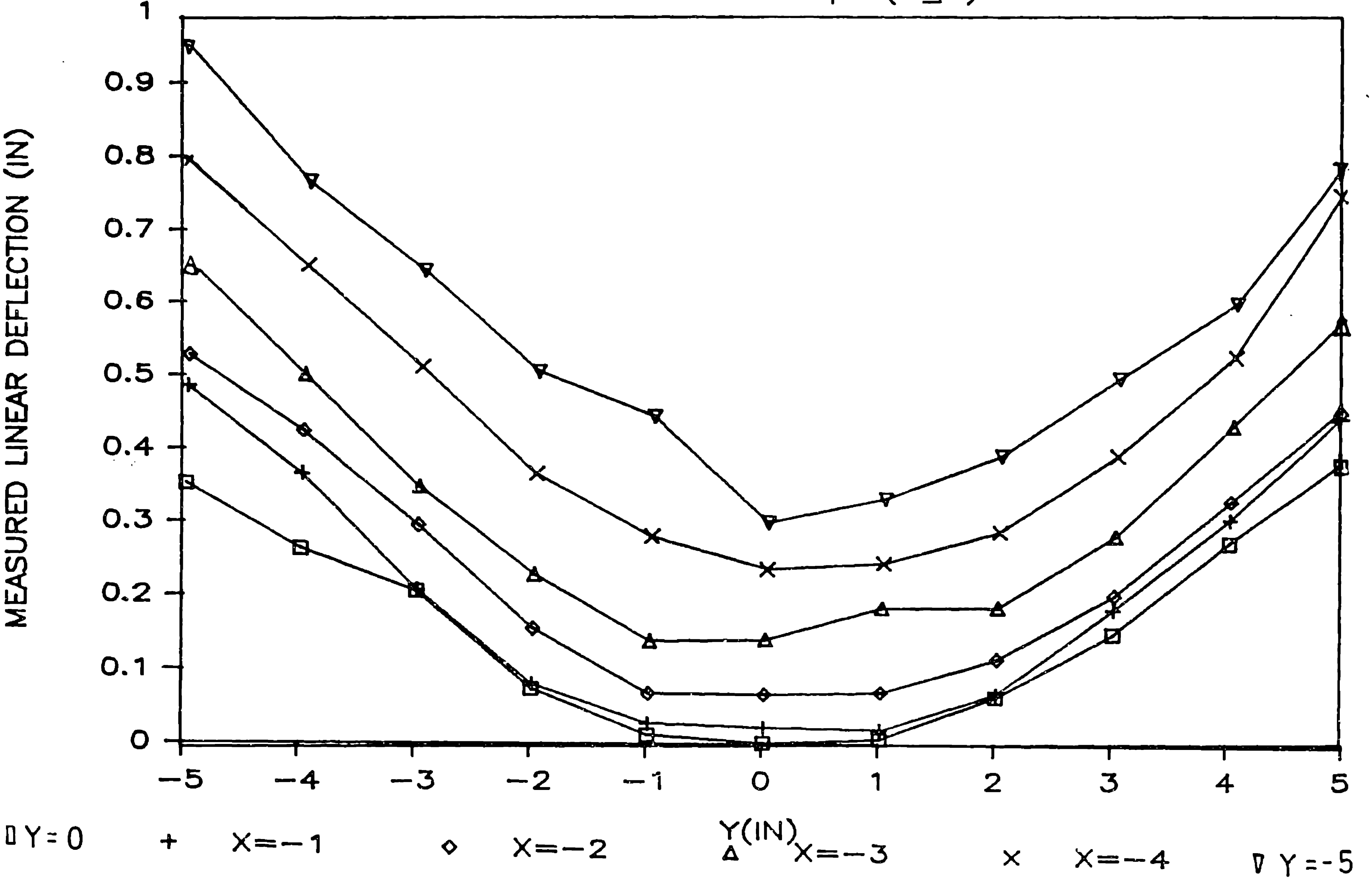

Figure 5.3.1—5: Model Deflections

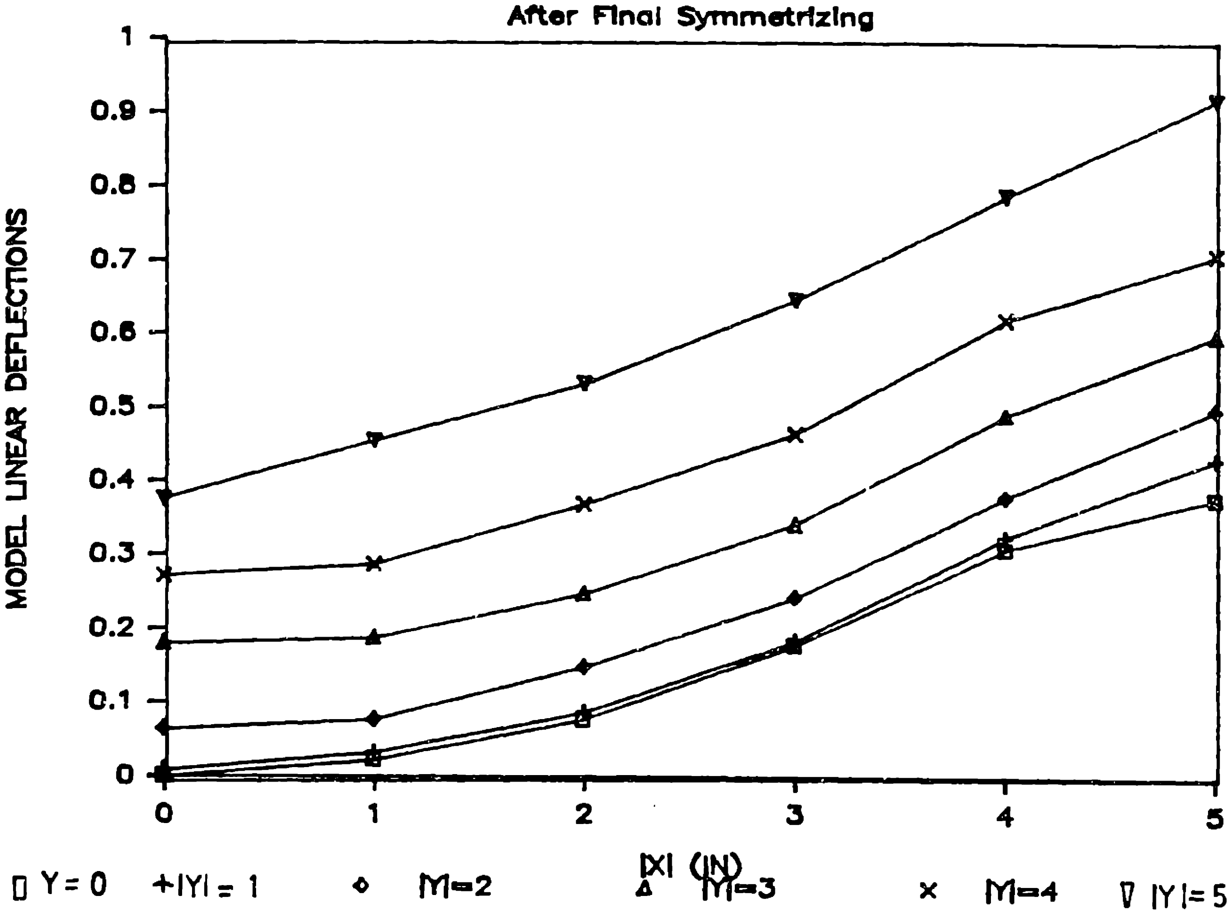

X	Y=+/-5 DEFL.	Y=+/-4 DEFL.	Y=+/-3 DEFL.	Y=+/-2 DEFL.	Y=+/-1 DEFL.	Y=0 DEFL.
+/-5	.922	.711	.601	.501	.433	.380
+/-4	.789	.621	.492	.380	.326	.310
+/-3	.647	.465	.342	.243	.183	.178
+/-2	.531	.368	.248	.148	.086	.077
+/-1	.453	.286	.187	.076	.032	.022
0	.373	.270	.179	.063	.008	.000

Table 5.3.1-2: Model Deflections After Final Symmetrizing

$$z_a(x,0) = (\mathcal{V}/2)\tan(k)|x| \qquad x = 0.1W_x$$

$$z_a(0,y) = (\mathcal{V}/2)\tan(k)|y| \qquad y = 0.1W_y$$

$$z_a(x,0) = \mathcal{V}\tan(k)|x| \qquad 0.1W_x < |x| \leq 0.2W_x$$

$$z_a(0,y) = \mathcal{V}\tan(k)|y| \qquad 0.1W_y < |y| \leq 0.2W_y$$

$$z_a(x,0) = \tan(k)[|x| - .2W_x(1-\mathcal{V})] \qquad .2W_x < |x| \leq .4W_x$$

$$z_a(0,y) = \tan(k)[|y| - .2W_y(1-\mathcal{V})] \qquad .2W_y < |y| \leq .4W_y$$

$$z_a(x,0) = \tan(k)[.75|x| + .2W_x\mathcal{V} - .1W_x] \qquad .4W_x < |x| \leq .5W_x$$

$$z_a(0,y) = \tan(k)[.75|y| + .2W_y\mathcal{V} - .1W_y] \qquad .4W_y < |y| \leq .5W_y$$

The multiplicative factor of .75 in the slope of the last series of equations accounts for edge effects. Figure 5.3.1-6 shows the algorithmic and model deflections for $|q| = 0$. To find the deflection at any point on the plate one now only has to add $z_a(x,0)$ and $z_a(0,y)$ for the particular coordinate (x,y).

b. Comparison of the Algorithm, Model, and Measured Deflections

Table 5.3.1-3 gives the model and algorithmic deflections and the deviations in per cent between them. The average deviation between z_m and z_a is about 8.5% which is within the goal of 10%. Outside one beam diameter radius of the center where flattening is greatest, the average deviation is about 7.5%. Figures 5.3.1-7 and 5.3.1-8 show the predicted and model curves for the dish shape. Figures 5.3.1-9 and 5.3.1-10 show the predicted and measured curves.

Figures 5.3.1-11 and 5.3.1-12 show a "3-D" perspective of the dish shape. Figure 5.3.1-11 shows the measured deflections while figure 5.3.1-12 show a 3 times magnification of the measured deflections to better show the shape and warpage.

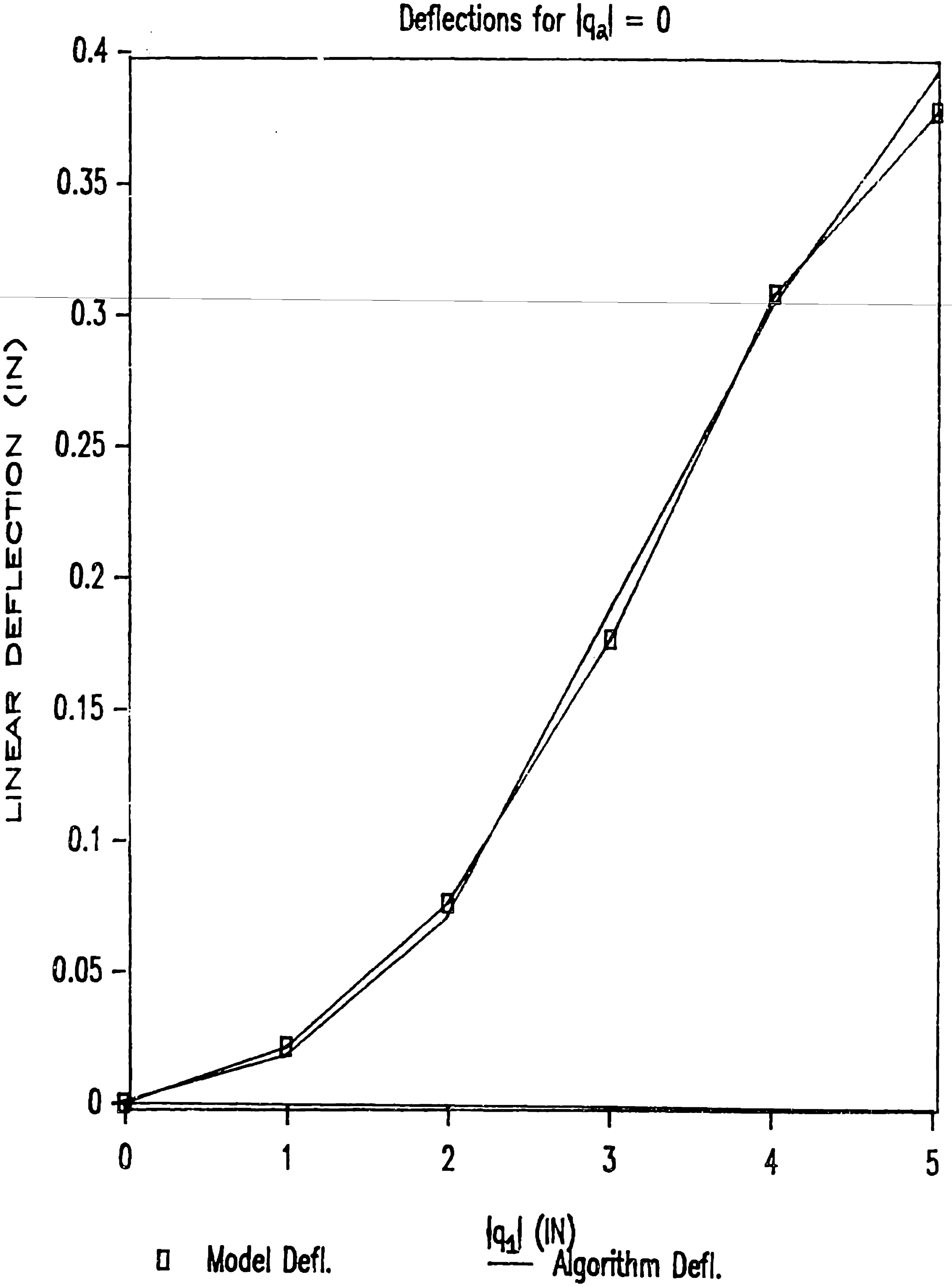

Figure 5.3.1–6: Model and Algorithm

X (+/-)	Y (+/-)	Z mdl	Z alg	DEVIATION %
0	0	0	0	0
1	0	.022	.018	18
2	0	.077	.071	7.8
3	0	.178	.189	5.8
4	0	.310	.306	1.3
5	0	.380	.395	3.8
0	1	.008	.018	56
1	1	.032	.035	8.6
2	1	.086	.089	3.4
3	1	.183	.206	11
4	1	.326	.324	0.6
5	1	.433	.412	4.8
0	2	.063	.071	11
1	2	.076	.089	15
2	2	.148	.142	4.1
3	2	.243	.260	6.5
4	2	.380	.377	0.8
5	2	.501	.466	7

Table 5.3.1-3: Model and Algorithm Deflections

X (+/-)	Y (+/-)	Z mdl	Z alg	DEVIATION %
0	3	.179	.189	5.3
1	3	.187	.206	9.2
2	3	.248	.260	4.6
3	3	.342	.378	9.5
4	3	.492	.495	0.6
5	3	.601	.584	2.8
0	4	.270	.306	11.8
1	4	.286	.323	11.5
2	4	.368	.377	2.4
3	4	.465	.495	6.1
4	4	.621	.612	1.5
5	4	.711	.701	1.4
0	5	.373	.395	5.6
1	5	.453	.413	8.8
2	5	.531	.466	12
3	5	.647	.584	9.7
4	5	.789	.701	22
5	5	.922	.790	14

Table 5.3.1-3: Model and Algorithm Deflections (continued)

Figure 5.3.1—7: Algorithm and Model

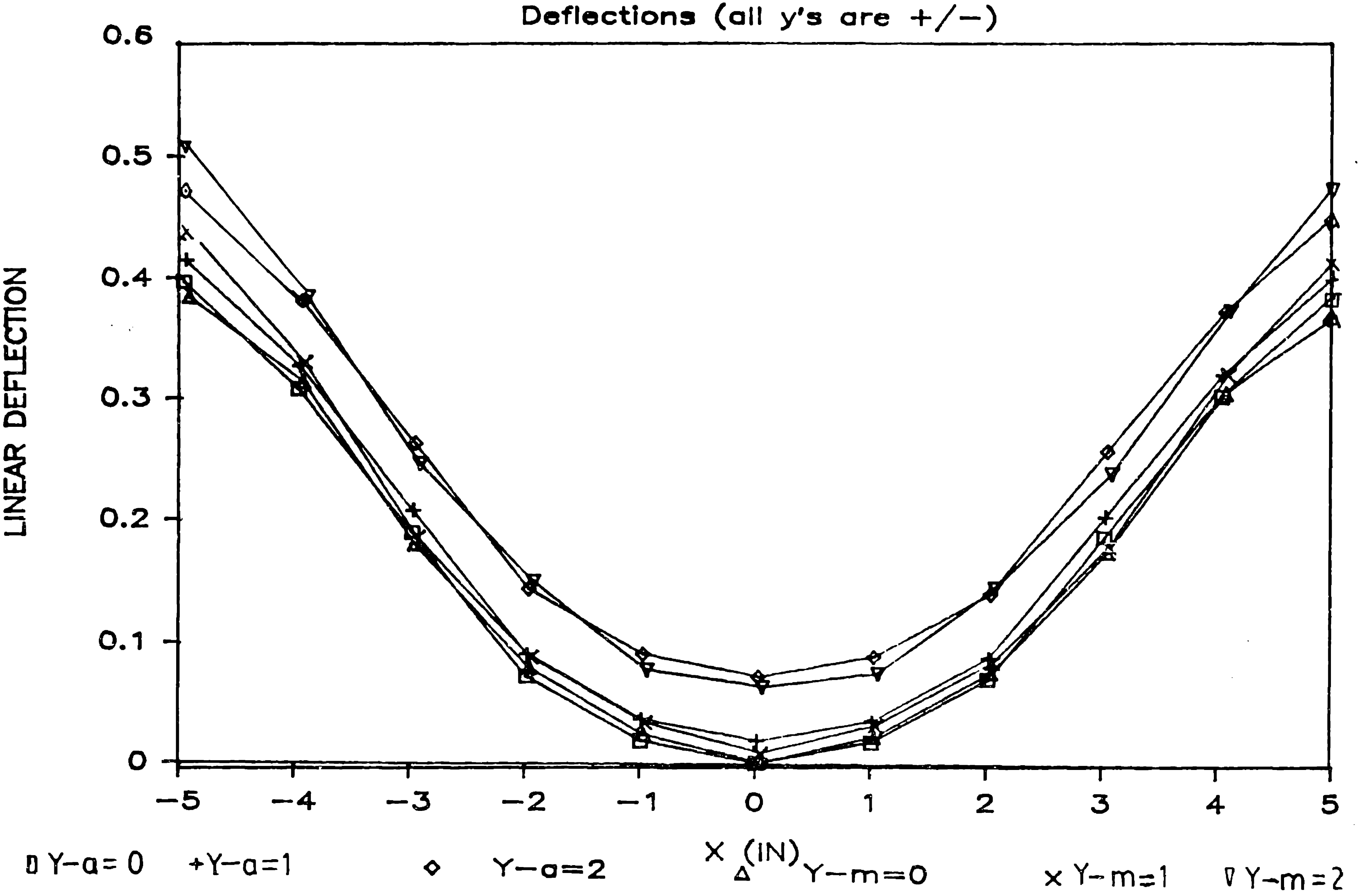

Figure 5.3.1—8: Algorithm and Model

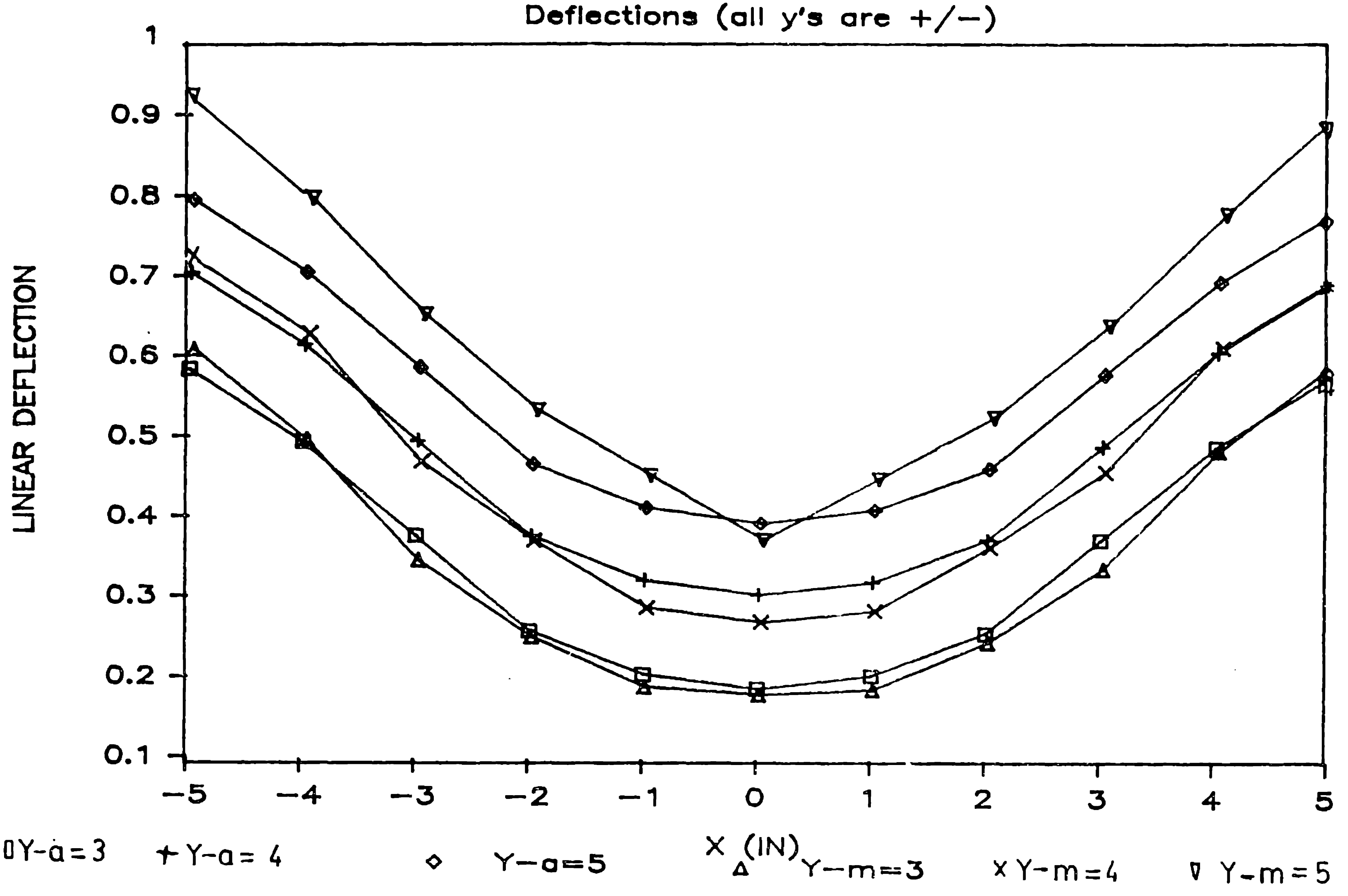

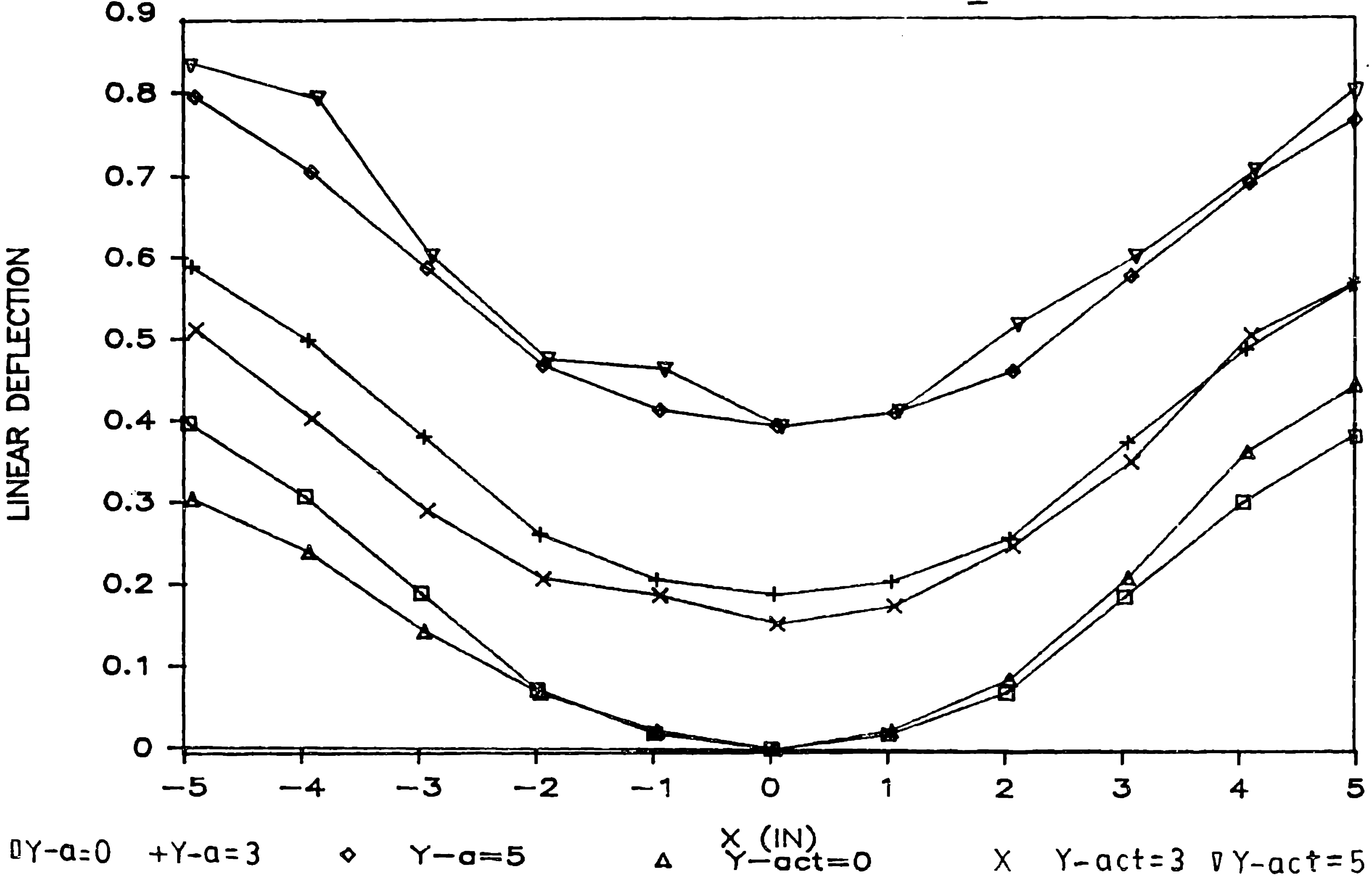

Figure 5.3.1—9: Algorithm and Actual

Deflections for Selected $Y \geq 0$

Figure 5.3.1—10: Algorithm and Actual

Deflections for Selected Y≤0

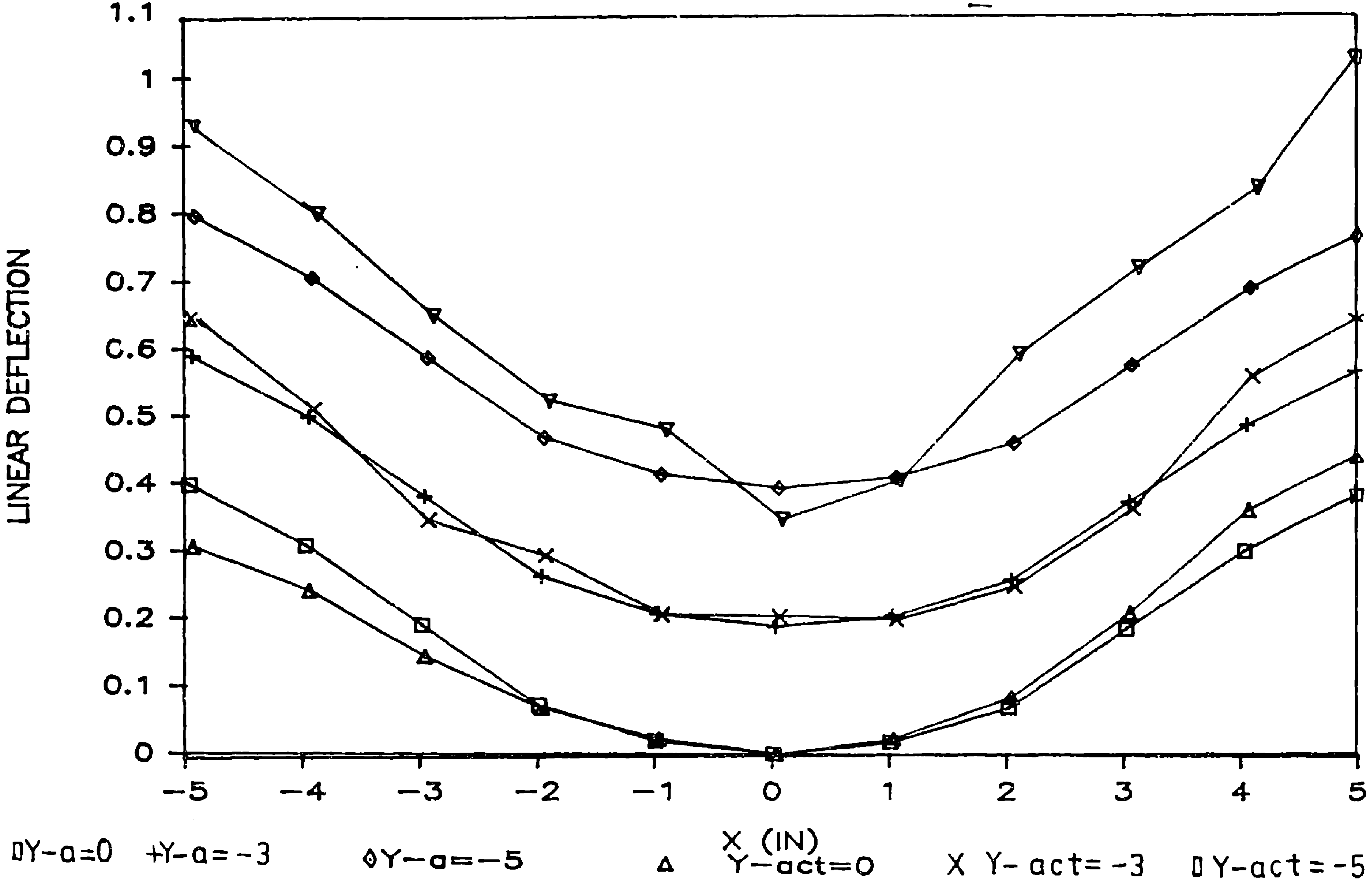

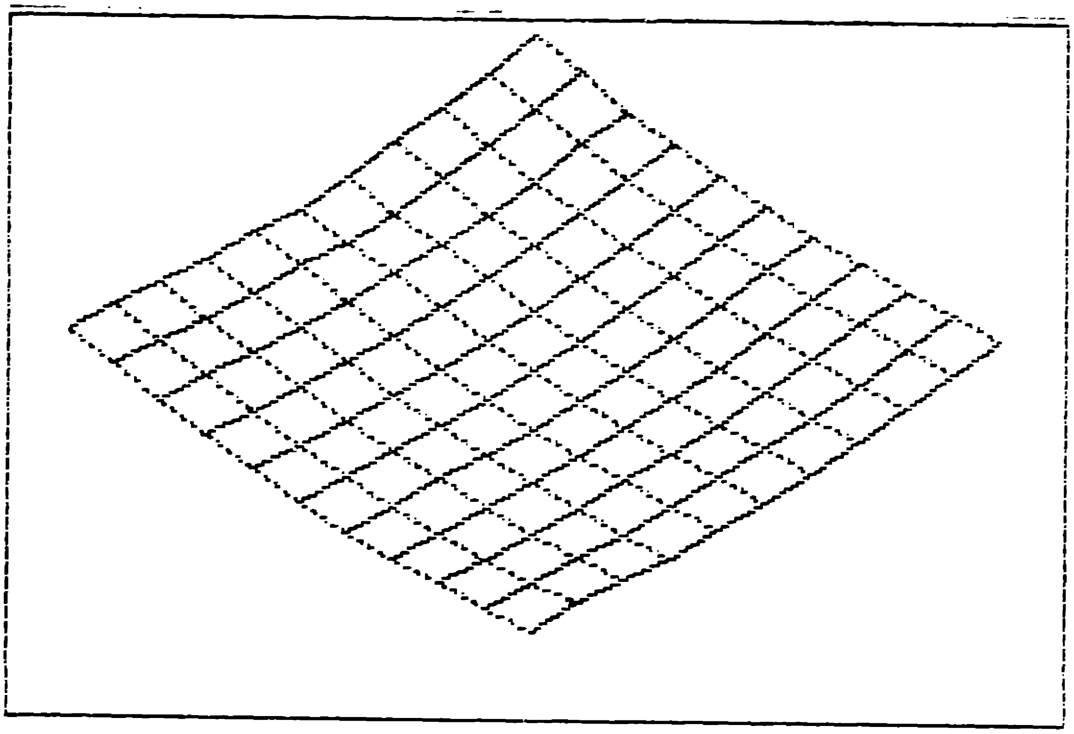

Figure 5.3.1-11: 3-D Perspective of the Dish Shape with Actual Deflections

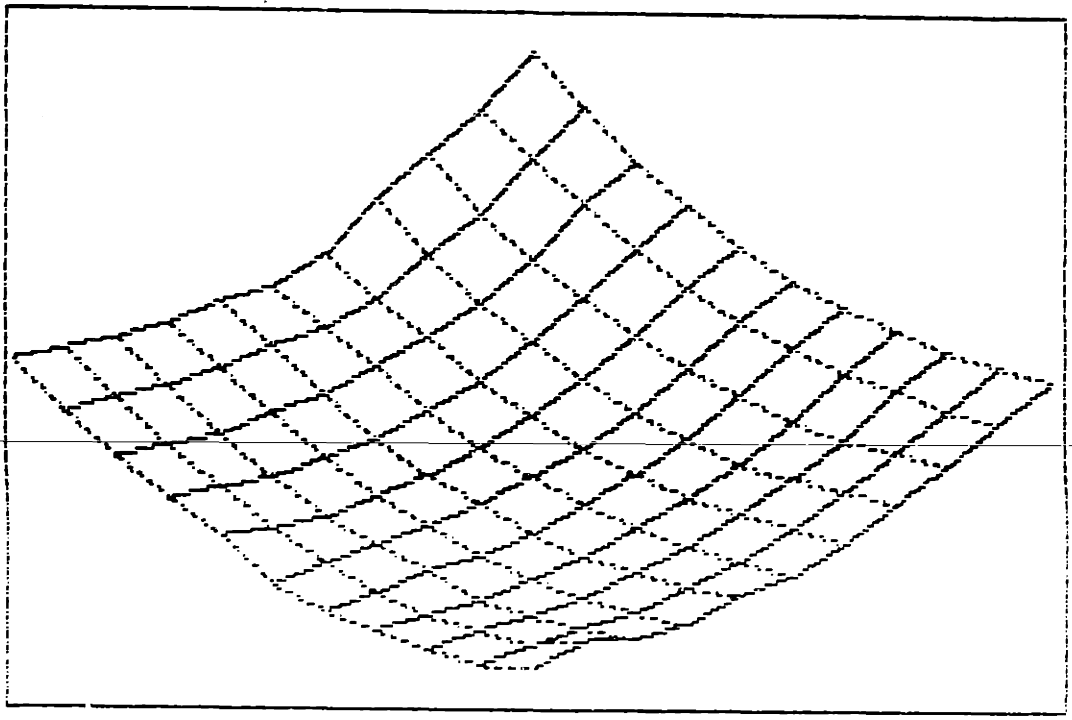

Figure 5.3.1-12: 3-D Perspective of the Dish with Deflections Magnified by 3 Times

5.3.2 Cone Shape

a. Derivation of the Model and Algorithm

The pattern of laser passes and relevant parameters used to produce the cone shape are given in Appendix A. Table 5.3.2-1 gives the actual, normalized data. Figures 5.3.2-1 to 3 are graphs of the raw data. In this case, imposed y-direction strains are present due to both the poisson effect and due to the non-orthogonality of the beam passes relative to the coordinate system. Therefore, longitudinal bending has a contribution approximately proportional to the sine of the angle between the y axis and the beam pass.

Analysis of the data seemed to indicate a significant coupling effect between beam passes. The x-direction deflections are significantly greater (2.5-5.75) than expected by either superposition ($n\theta_f/2$) or by the tan(k) parameter. This significant deviation from expected behavior may be an inertial effect. As the angle of the beam pass with the y axis increases, the closer the beam is to the corner of the plate. The much less inertia of the plate on the outboard side of the beam pass should imply that the majority of the angular deflection from the beam pass would be manifested on that outboard side. As the angle increases, the larger this effect would be. Another possible contributor to this "amplification" effect is the density of heating at the focus of the beam pattern. Geometric symmetry dictates that, for the model, $z(x,y) = z(-x,y)$.

X	Y=-9 DEFL	Y=-6 DEFL	Y=-3 DEFL	Y=0 DEFL
-12	.903	1.013	-	-
-11.125	-	-	.984	-
-10.188	-	-	-	.930
-9.125	-	-	-	-
-8.875	-	-	-	-
-8.0	.324	.374	.474	.390
-7.063	-	-	-	-
-4.0	-.034	.057	.113	.100
0	-.142	-.048	.008	.000
4.0	-.058	.079	.154	.176
6.938	-	-	-	-
7.875	-	-	-	-
8.0	.356	.105	.498	.577
8.875	-	-	-	-
9.875	-	-	-	.824
10.875	-	-	.841	-
12	.707	.823	-	-

Table 5.3.2-1: Raw Deflection Data for the Cone Shape

X	Y=0 DEFL	Y=3 DEFL	Y=6 DEFL	Y=9 DEFL
-12	-	-	-	-
-11.125	-	-	-	-
-10.188	.930	-	-	-
-9.125	-	.785	-	-
-8.875	-	-	.580	-
-8.0	.390	.509	-	-
-7.063	-	-	-	.388
-4.0	.100	.116	.083	-.001
0	.000	-.002	-.063	-.142
4.0	.176	.163	.123	.008
6.938	-	-	-	.378
7.875	-	-	.586	-
8.0	.577	.662	-	-
8.875	-	.736	-	-
9.875	.824	-	-	-
10.875	-	-	-	-
12	-	-	-	-

Table 5.3.2-1: Raw Deflection Data for the Cone Shape (cont)

Figure 5.3.2—1: Raw Deflection Data

for the Cone Shape(Y≥0)

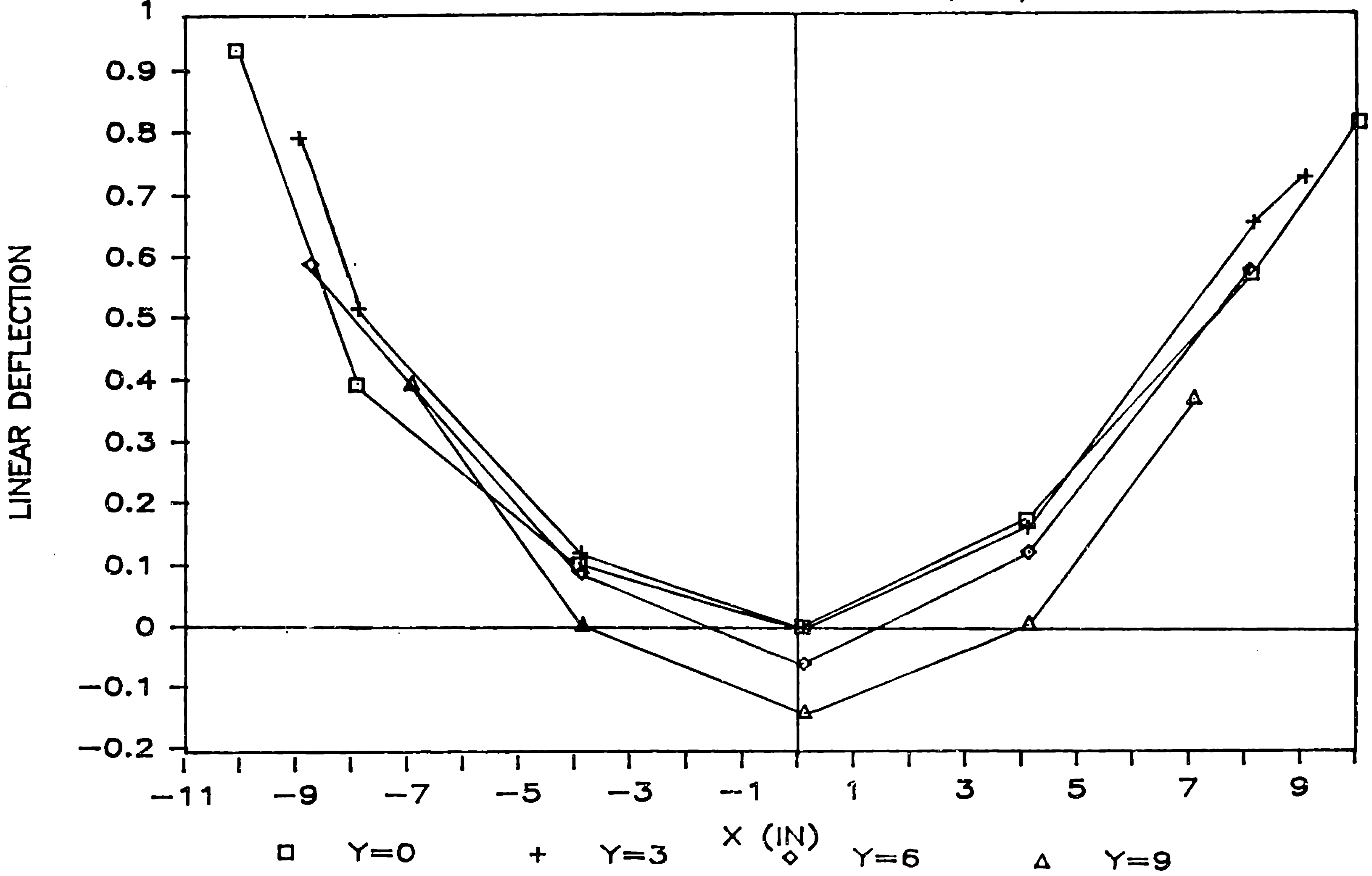

Figure 5.3.2—2: Raw Deflection Data

for the Cone Shape (Y≤0)

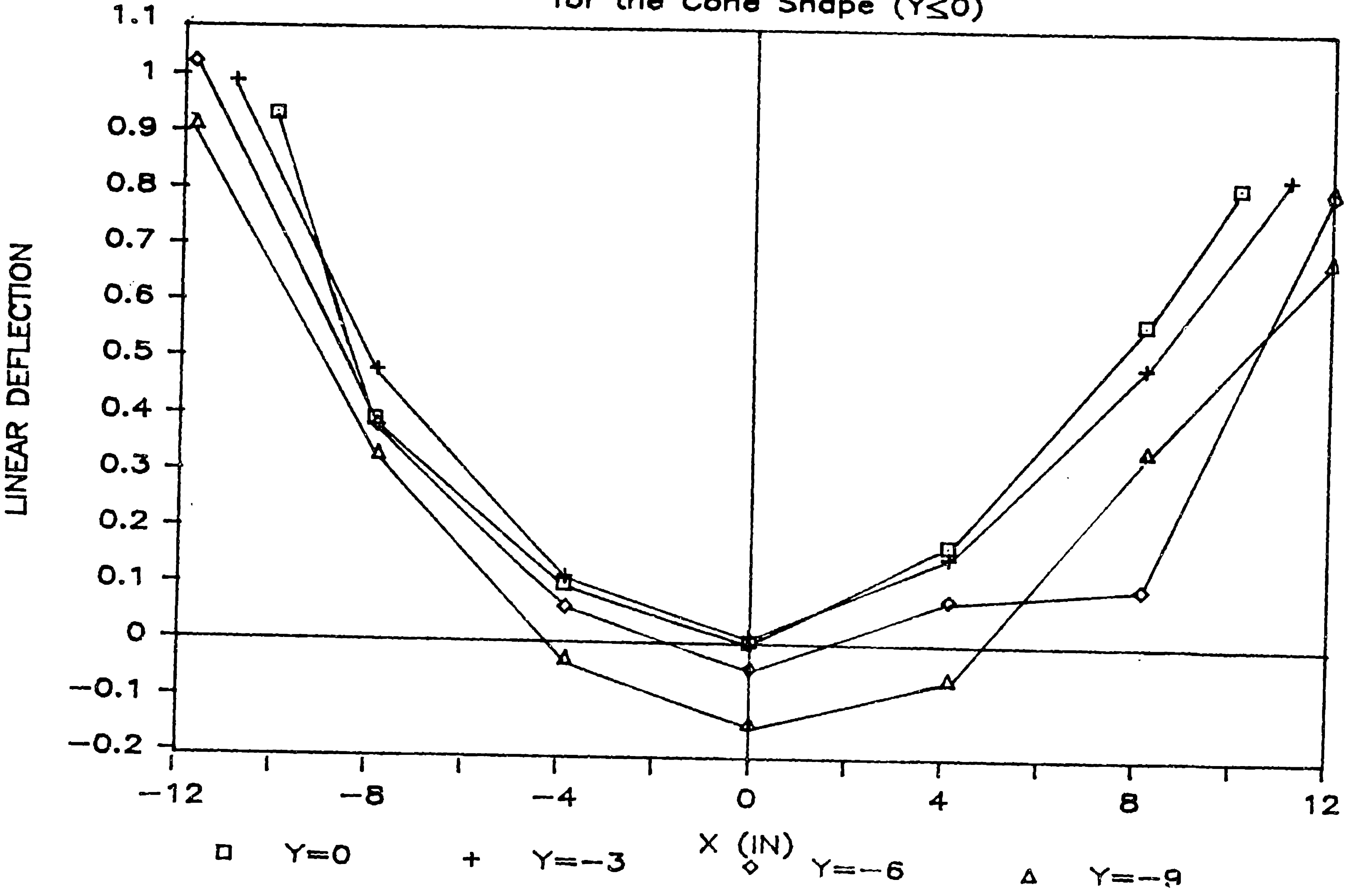

Figure 5.3.2—3 Raw Deflection Data

for the Cone Shape

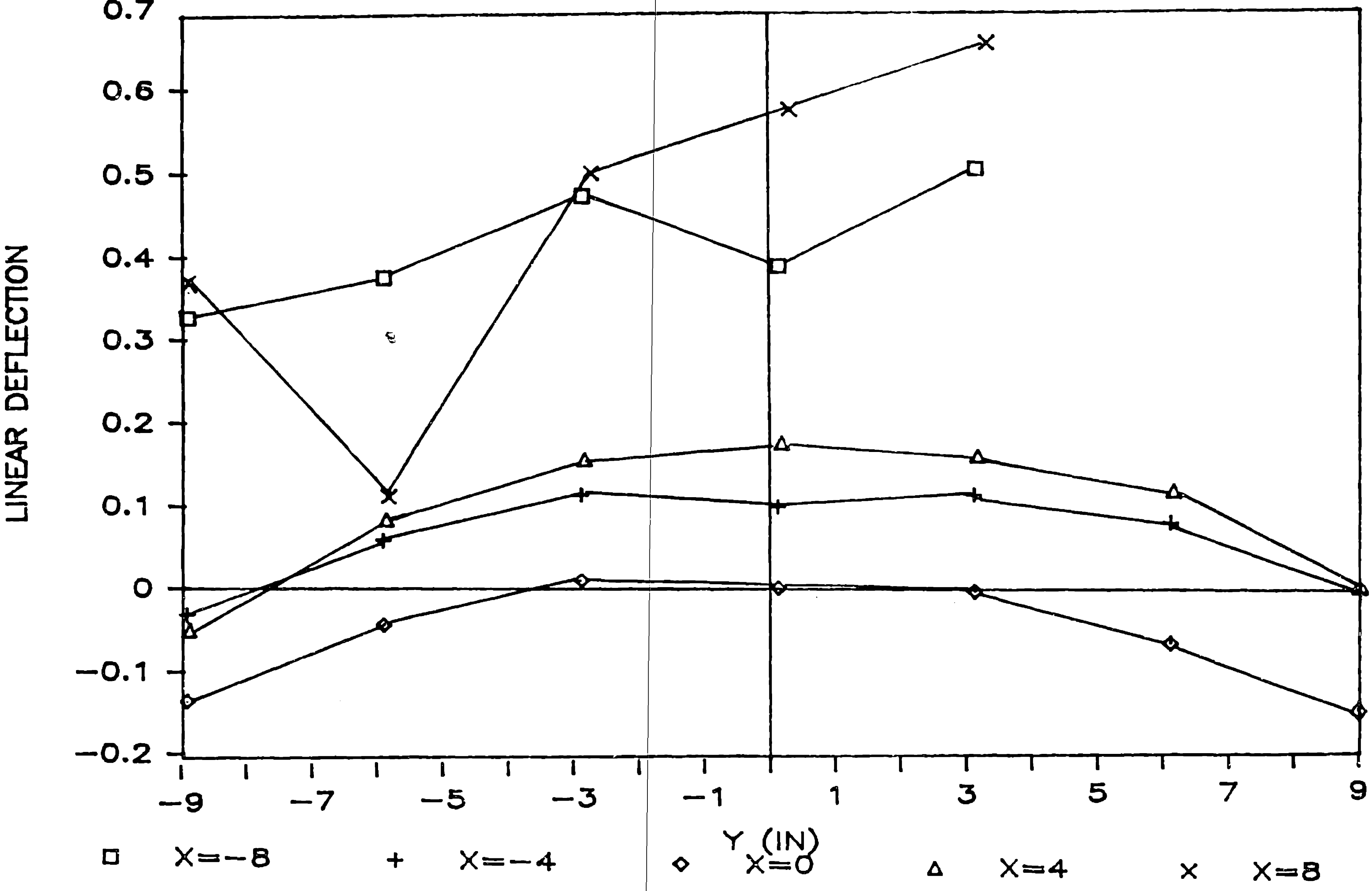

No symmetry exists across the $y = 0$ line. Table 5.3.2-2 and figure 5.3.2-4 and 5.3.2-5 give the symmetrized and dewarped model deflections. As one would predict from the geometry of a cone, the changes in deflection slopes as a function of x are significantly greater for the region of $Y > 0$ than for the region of $Y < 0$. For this reason one algorithm for each region was developed. Since the plate was cut as shown in Appendix A, the effective area term in the tan(k) parameter was formulated on the basis of the area enclosed by the perimeter of the shape minus 2 inches divided by the area of the plate. Using these values gives:

$$\tan(k) = \tan[(7)(.7)(282)/(2)(356.25)] = .0337$$

It was discussed above that an "amplification" factor was evident in the values of the deflection slopes of the model. One set of empiracal equations that satisfy the observed increases in deflection slope are:

$$f = 1 \qquad x < W_y\tan(a_1) + BD$$

$$f = W_x \sin(a_2)/k \qquad W_y\tan(a_1)+BD \leq x < W_y\tan(a_3) + BD$$

$$f = W_x\sin(a_3)/2\cdot k\cdot\nu \qquad W_y\tan(a_3) + BD \leq x \leq W_x/2$$

where f is the amplification factor; a_1, a_2, a_3 are the angles of the beam pass with the y axis; k is the distributed deflection angle; BD is the beam diameter; and ν is poisson's ratio. For the conditions under which this cone was made:

$$f = 1 \qquad x < 3.5''$$

$$f = 2.5 \qquad 3.5'' \leq x < 7.5''$$

$$f = 5.75 \qquad 7.5'' \leq x \leq 12''$$

X	Y=-9 DEFL	Y=-6 DEFL	Y=-3 DEFL	Y=0 DEFL	Y=3 DEFL	Y=6 DEFL	Y=9 DEFL
-12	.802	.915	-	-	-	-	-
-11	-	-	.907	-	-	-	-
-10	-	-	-	.859	-	-	-
-9	-	-	-	-	.758	-	-
-8	.268	.382	.483	.481	.583	.543	-
-7	-	-	-	-	-	-	.379
-4	-.049	.065	.131	.135	.137	.100	0
0	-.145	-.059	0	0	0	-.059	-.145
4	-.049	.065	.131	.135	.137	.100	0
7	-	-	-	-	-	-	.379
8	.268	.382	.483	.481	.583	.543	-
9	-	-	-	-	.758	-	-
10	-	-	-	.859	-	-	-
11	-	-	.907	-	-	-	-
12	.802	.915	-	-	-	-	-

Table 5.3.2-2: Model Deflections for the Cone Shape

Figure 5.3.2—4: Model Deflections

for the Cone Shape (Y≥0)

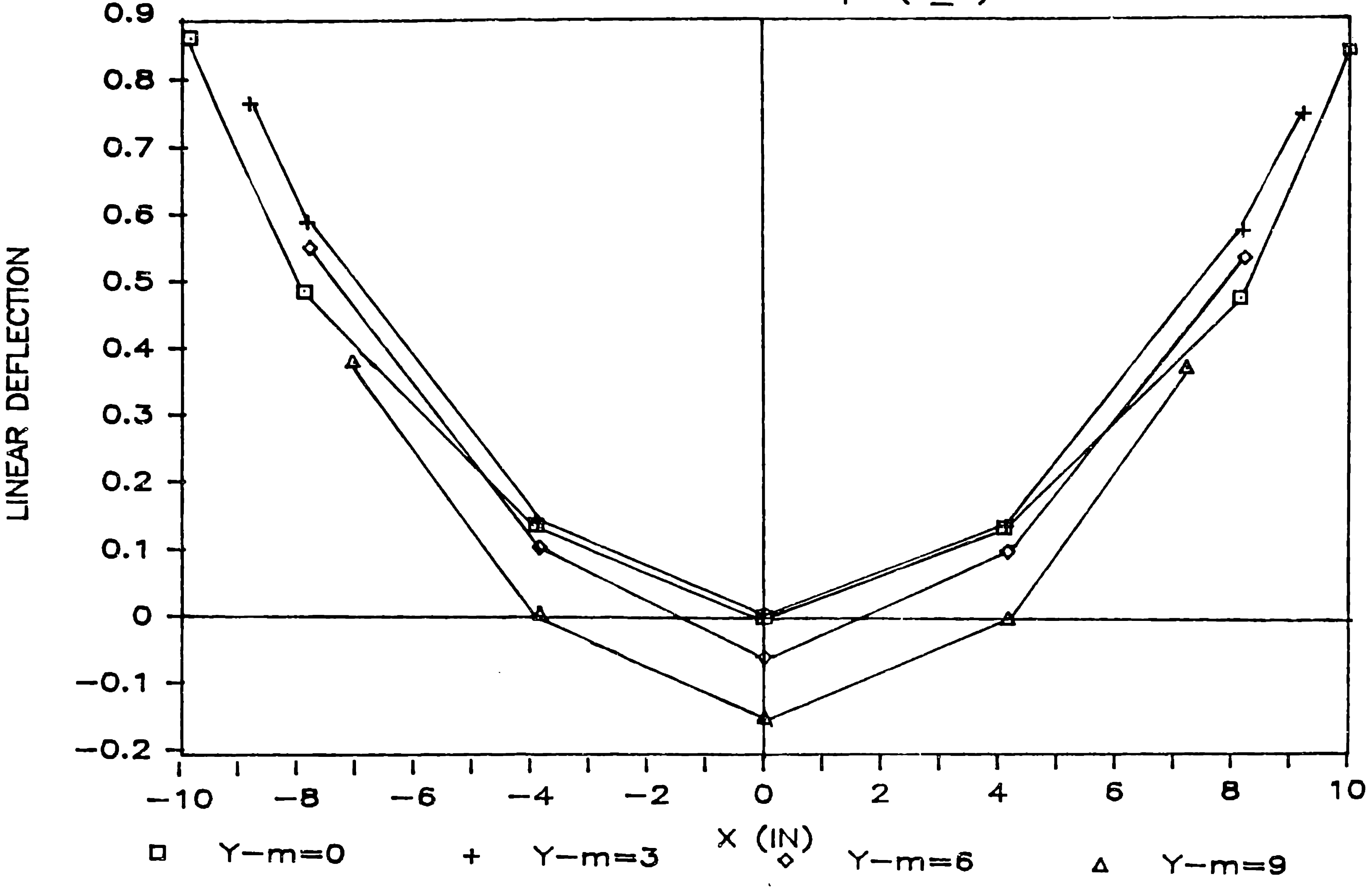

Figure 5.3.2—5: Model Deflections

for the Cone Shape (Y≤0)

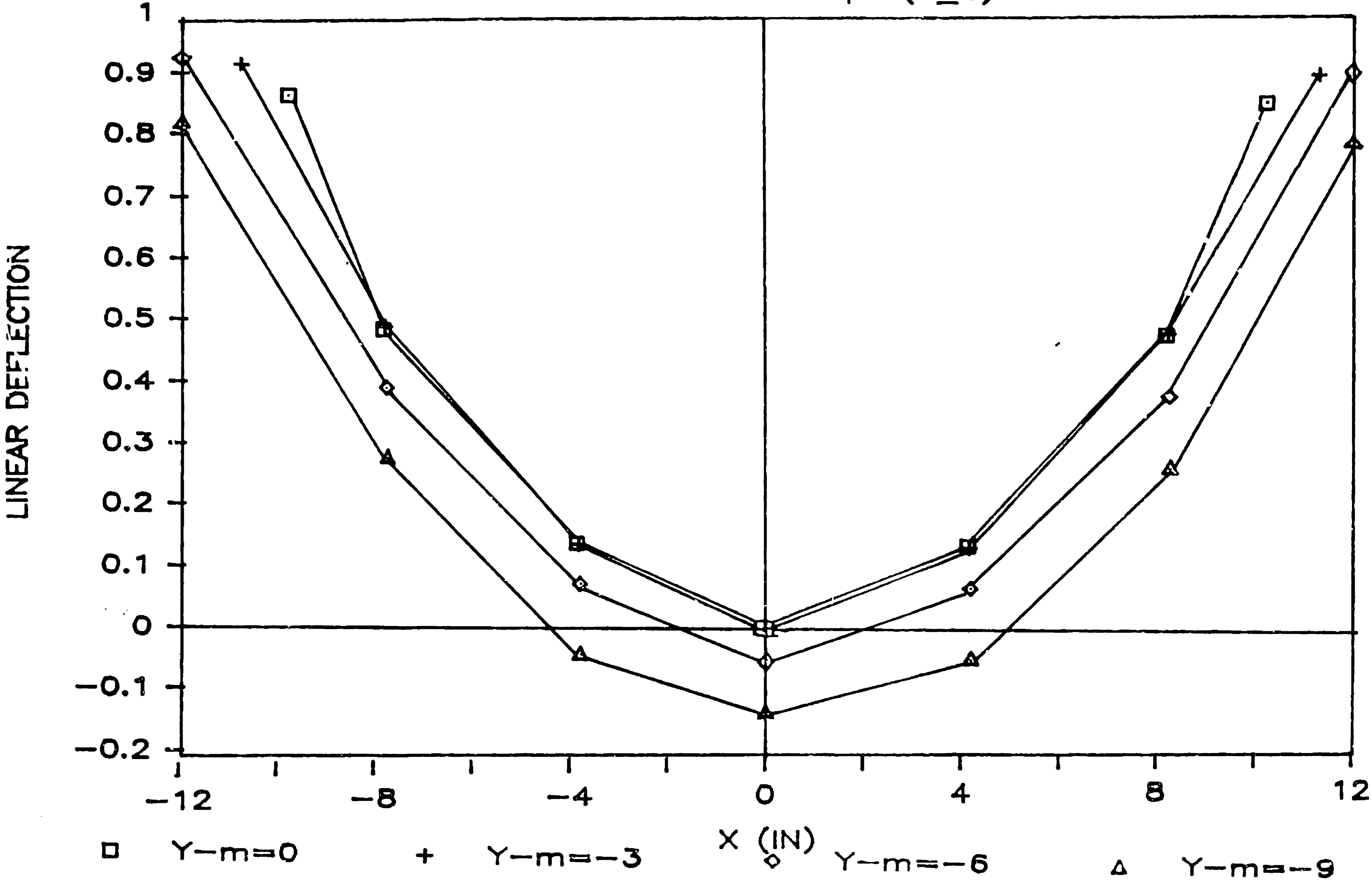

Directly inputting the above values for f into the equations, the algorithm's equations become:

$$z_a(0,y) = 0 \qquad -W_y/6 \leq y \leq W_y/6$$

$$z_a(0,y) = -(1-\nu)\tan(k)[|y| - 3] \qquad |y| \geq W_y/6$$

I. $y = 0$

$$z_a(x,0) = \tan(k)x \qquad 0 \leq x \leq W_x/6$$

$$z_a(x,0) = 2.5\tan(k)[x - 0.1W_x] \qquad W_x/6 < x \leq W_x/3$$

$$z_a(x,o) = \tan(k)[5.75x - 4W_x/3] \qquad W_x/3 < x \leq W_x/2$$

II. $y < 0$

$$z_a(x,0) = \tan(k)x \qquad 0 \leq x \leq W_x/6$$

$$z_a(x,0) = 2.5\tan(k)[x - 0.1W_x] \qquad W_x/6 < x \leq W_x/3$$

$$z_a(x,0) = \tan(k)[(1-\nu)(5.75)x-.758W_x] \qquad W_x/3<x\leq W_x/2$$

III. $y > 0$

$$z_a(x,0) = \tan(k)x \qquad 0 \leq x \leq W_x/6$$

$$z_a(x,0) = \tan(k)[3.675x - 2.675W_x/6] \qquad W_x/6<x\leq W_x/3$$

$$z_a(x,0)=\tan(k)[5.75(1- \frac{\nu}{(W_x/2)-x}) - 1.1375W_x +11.5\nu]$$

for $w_x/3 < x \leq W_x/2$

$$z_a(x,0) = \tan(k)[5.75x-1.1375W_x + 11.5\nu]$$

for $x = W_x/2$

$$z_a(x,0) = z_a(-x,0)$$

Figure 5.3.2-6 and 5.3.2-7 are graphs of the model and algorithm y = 0 and x = 0 contours.

Figure 5.3.2—6: Model and Algorithm

Deflections for Cone at Y=0 Contour

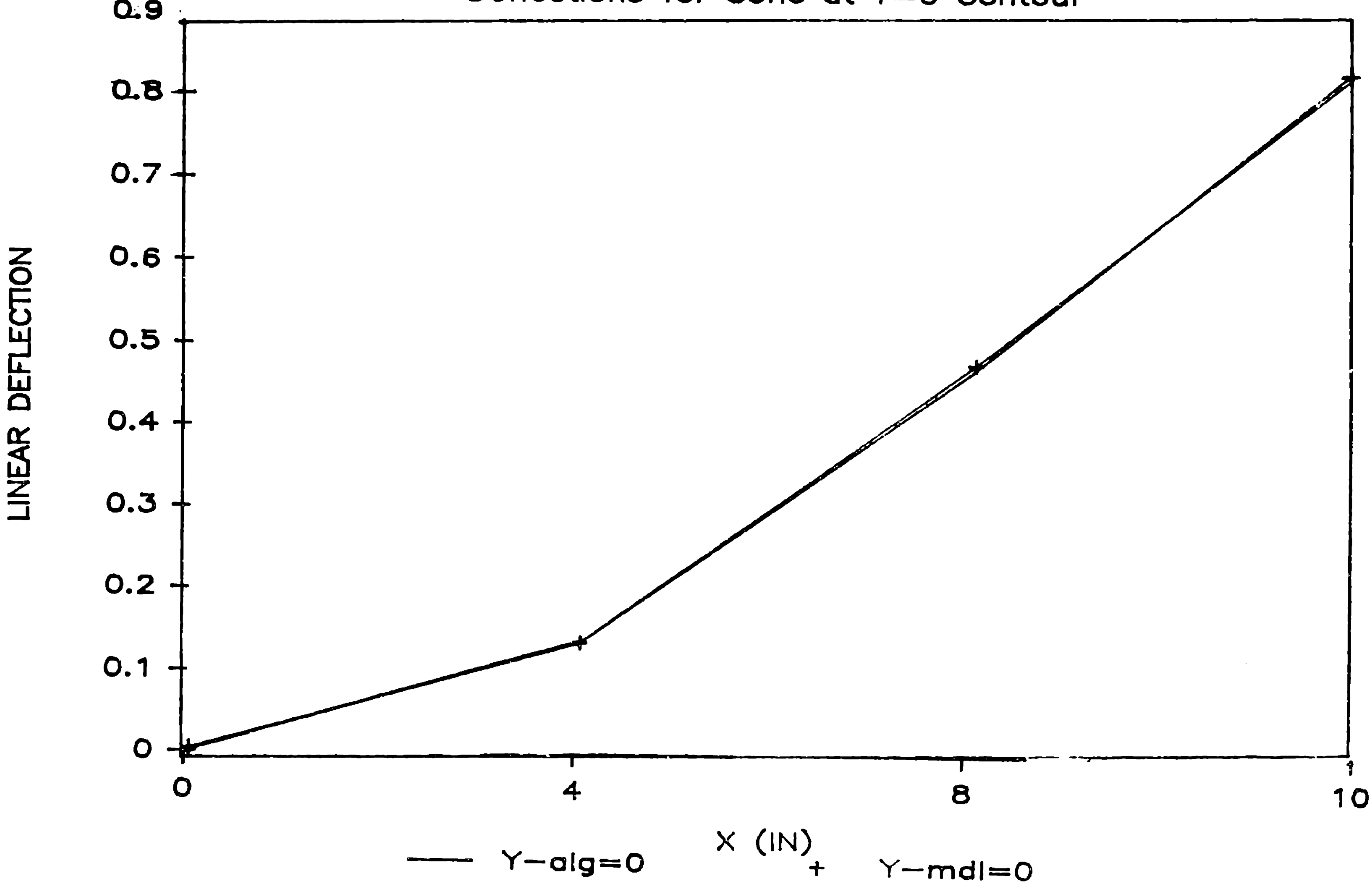

Figure 5.3.2—7: Model and Algorithm

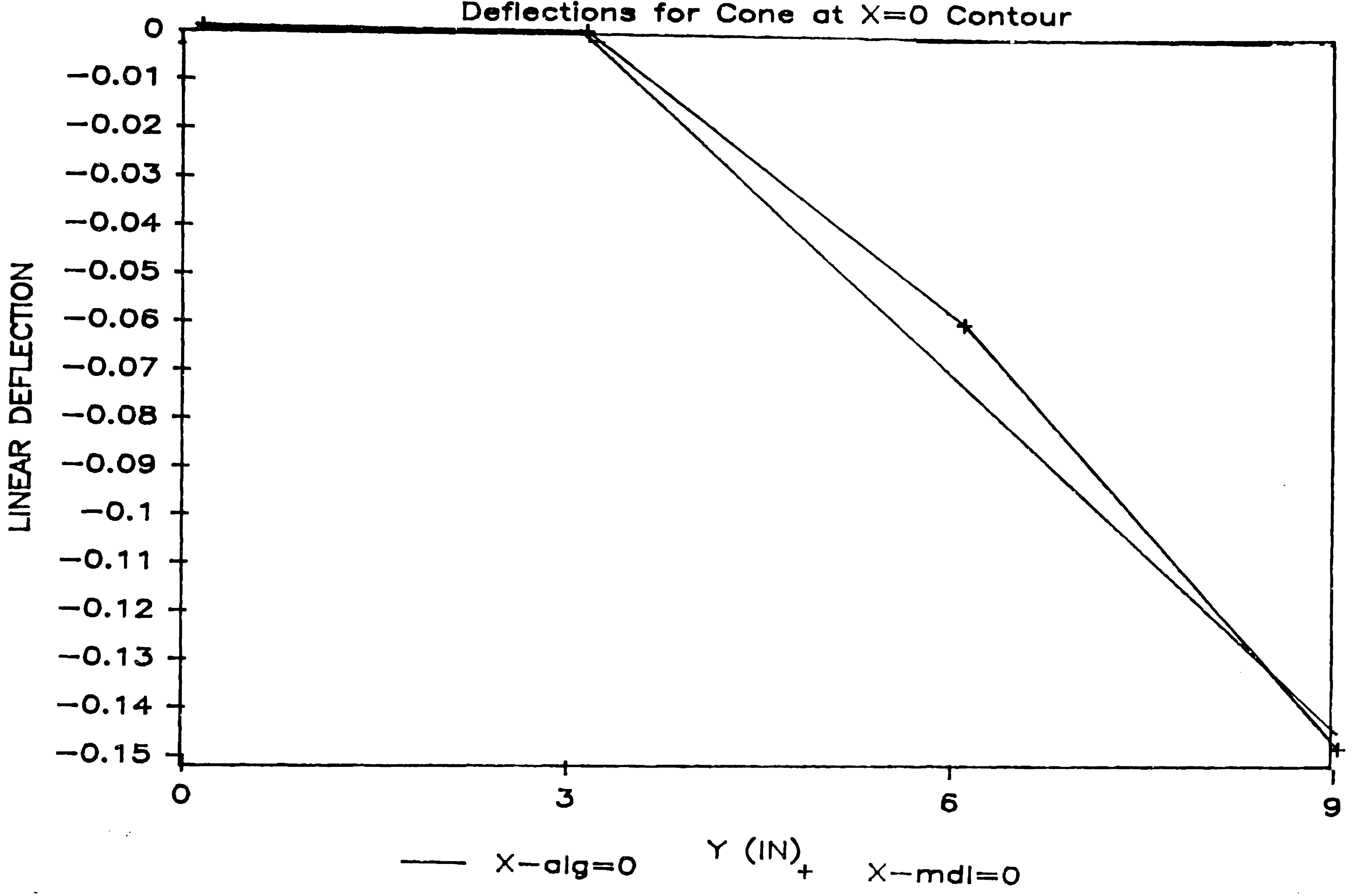

b. Comparison of the Algorithm, Model, and Measured Deflections

Table 5.3.2-3 shows the predicted and model deflections and the deviation between the two. The average deviation is 5.2%. Figures 5.3.2-8 and 5.3.2-9 compare the predicted and model curves. Figures 5.3.2-10 and 5.3.2-11 compare the predicted and measured values. Figure 5.3.2-12 shows a "3-D" perspective of the measured values.

X (+/-)	Y	Z-mdl DEFL	Z-alg DEFL	DEVIATION %
10	0	.859	.860	0.12
8	0	.481	.472	1.9
4	0	.135	.135	0
0	0	0	0	0
9	3	.758	.766	1.04
8	3	.583	.630	7.5
4	3	.137	.135	1.5
0	3	0	0	0
8	6	.543	.489	9.9
4	6	.100	.064	36
0	6	-.059	-.071	16.9
7	9	.379	.365	3.7
4	9	0	-.007	-
0	9	-.145	-.142	2.1

Table 5.3.2-3: Model and Algorithm Deflections

X (+/-)	Y	Z-mdl DEFL	Z-alg DEFL	DEVIATION %
11	-3	.907	.878	3.2
8	-3	.483	.472	2.3
4	-3	.131	.135	3.0
0	-3	0	0	0
12	-6	.915	.943	3.0
8	-6	.382	.401	4.7
4	-6	.065	.064	1.5
0	-6	-.059	-.071	17
12	-9	.802	.872	8.0
8	-9	.268	.275	2.5
4	-9	.049	.048	2.1
0	-9	-.145	-.142	2.1

Table 5.3.2-3: Model and Algorithm Deflections (continued)

Figure 5.3.2—8:Algorithm & Model

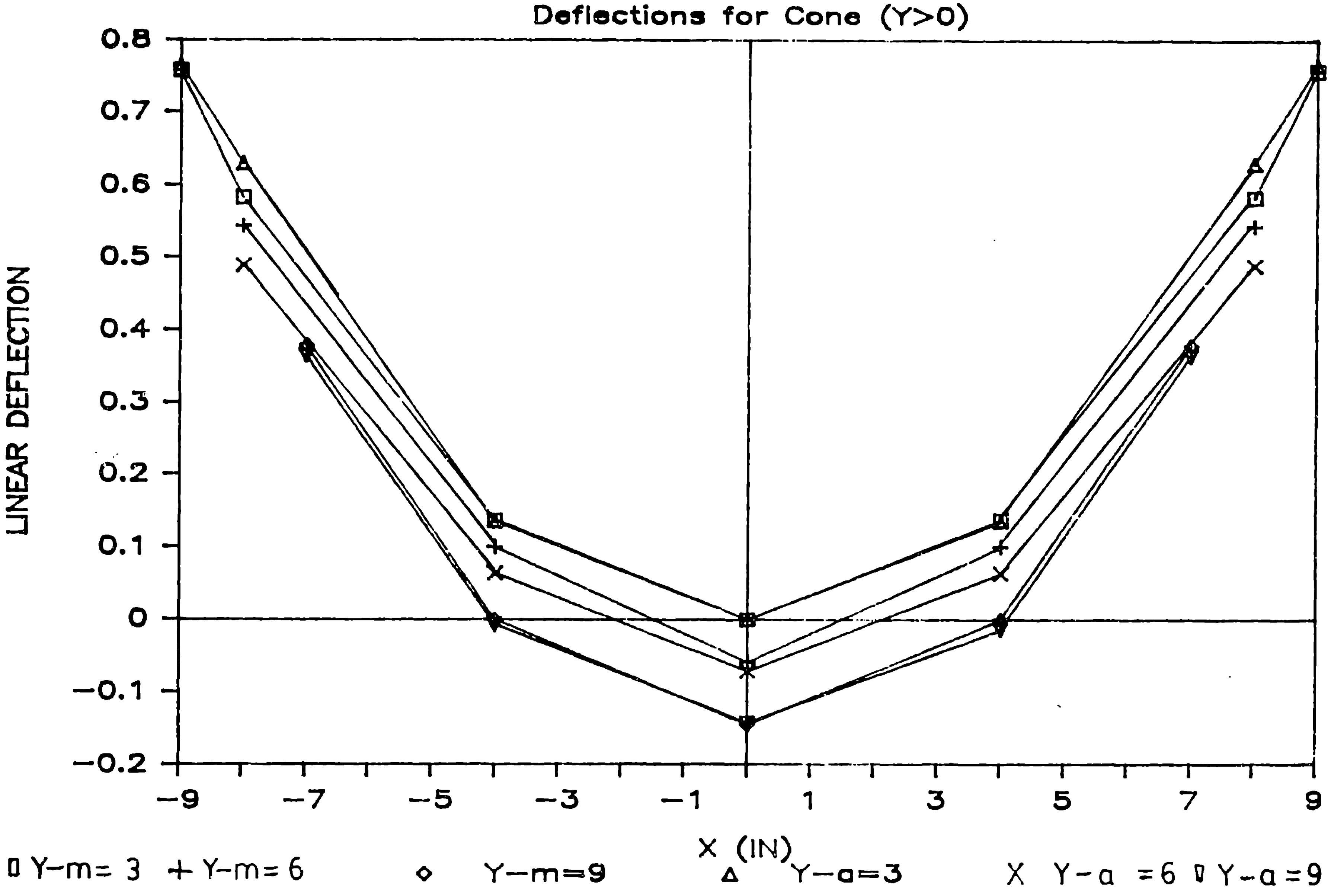

Figure 5.3.2—9:Algorithm & Model

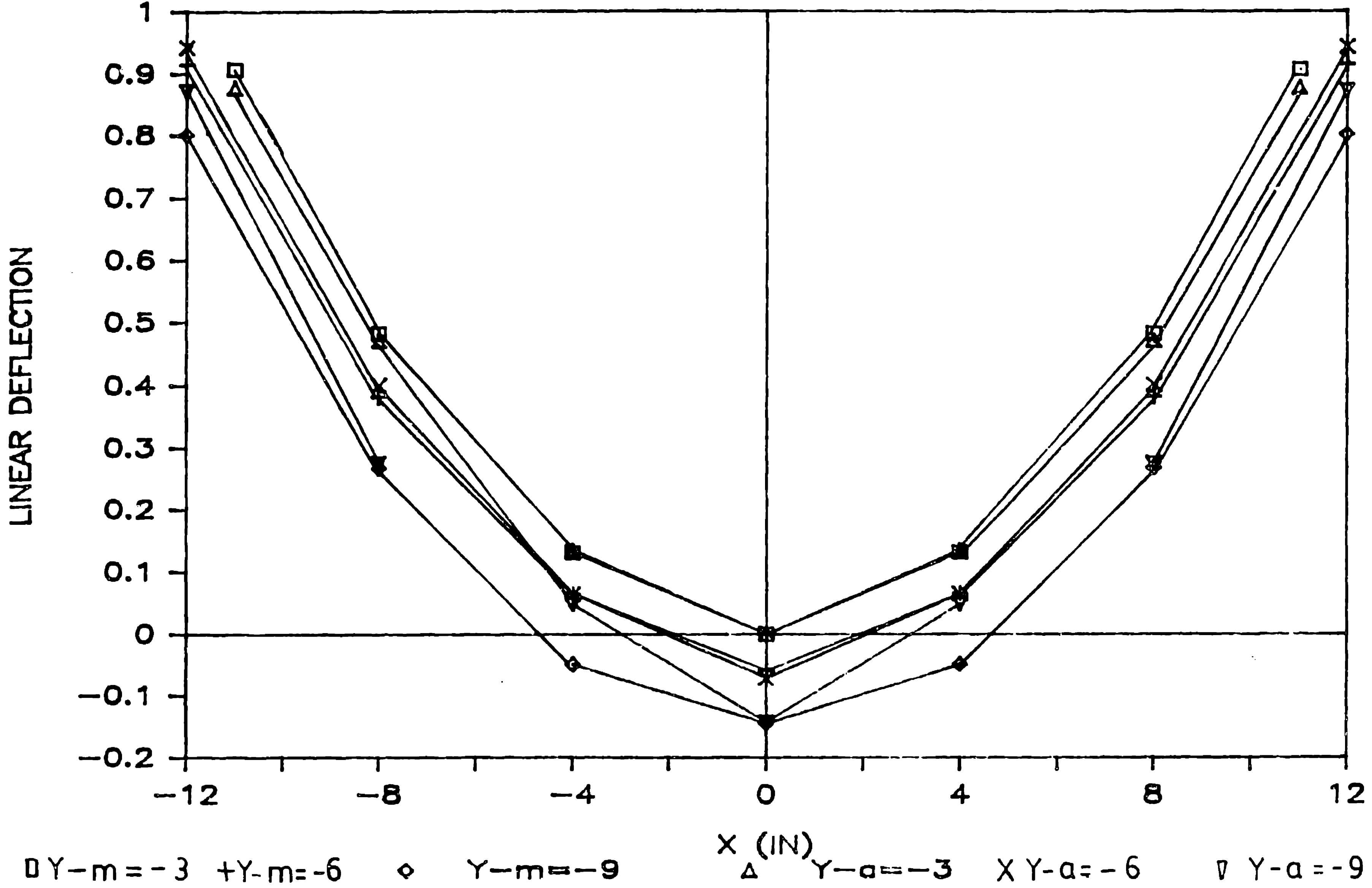

Deflections for Cone (Y<0)

Figure 5.3.2—10: Algorithm & Actual

Deflections for Cone (Y>0)

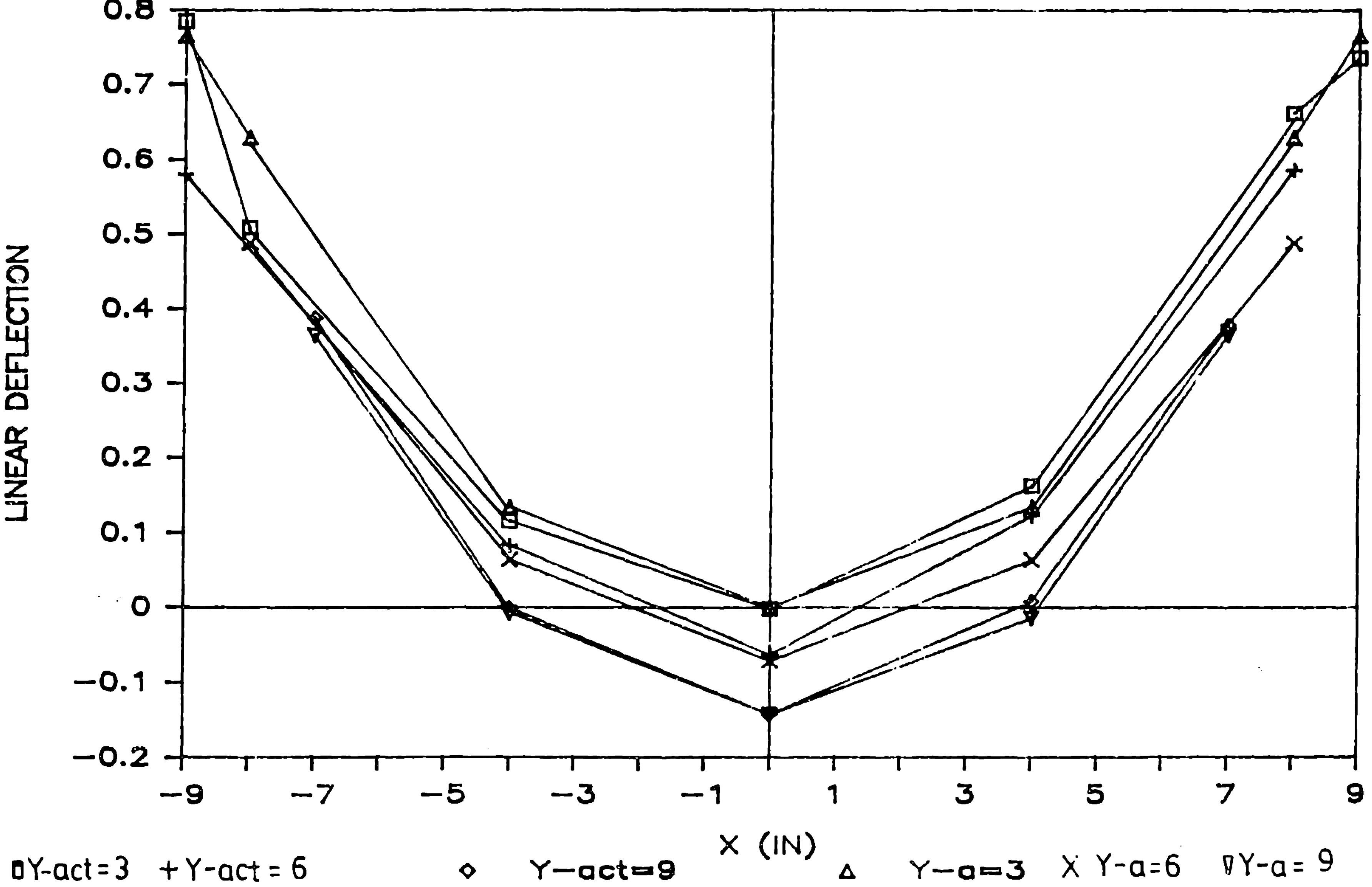

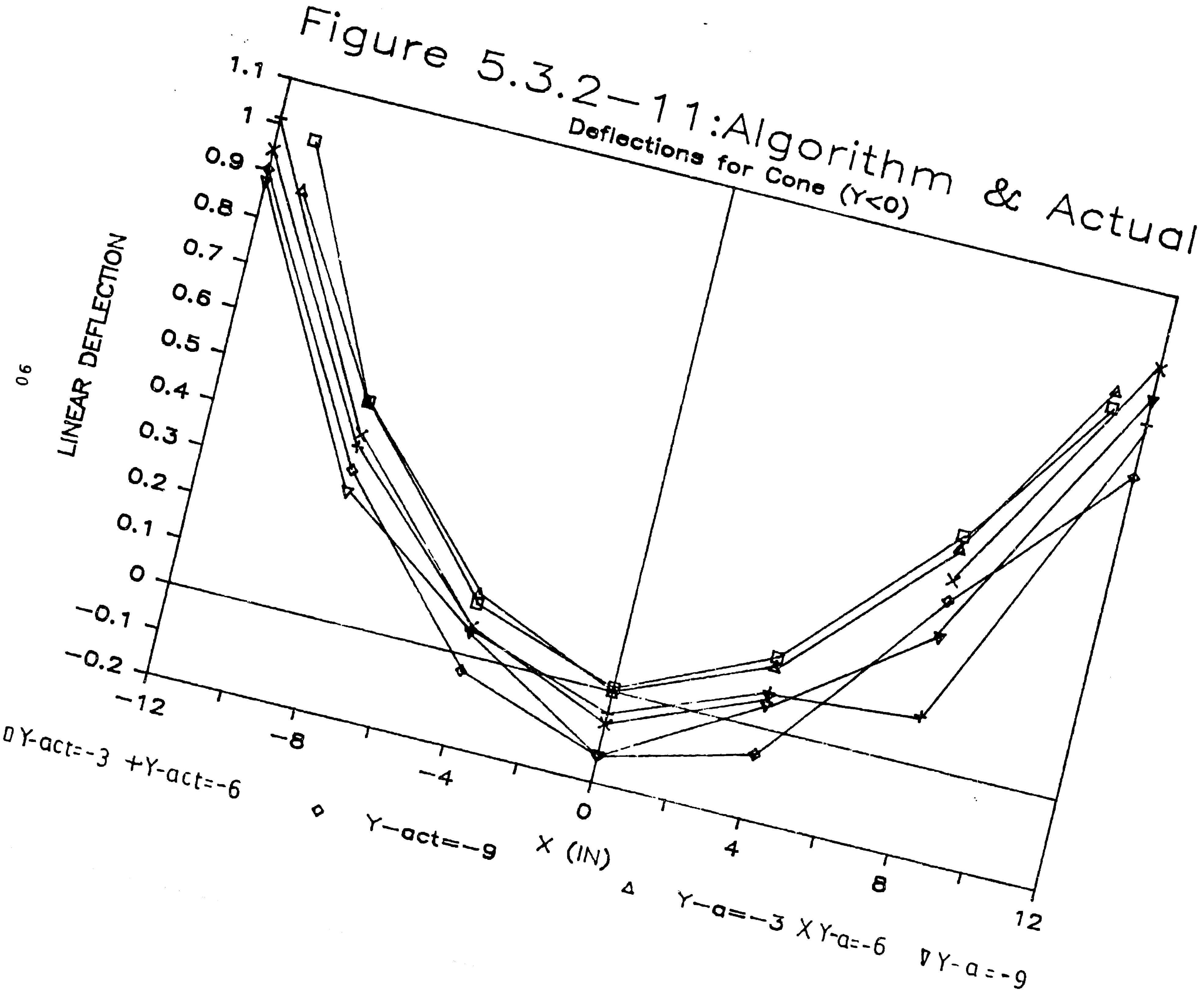

Figure 5.3.2–11:Algorithm & Actual

Deflections for Cone (Y<0)

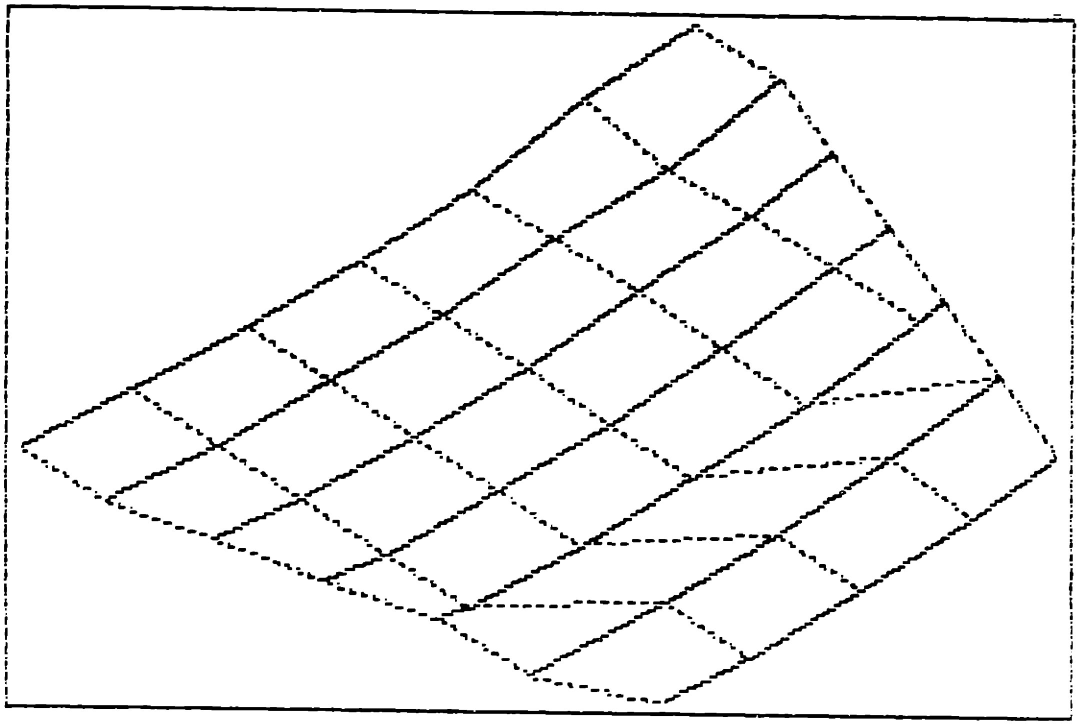

Figure 5.3.2-12: 3-D Perspective of the Cone Shape with Actual Deflections

5.3.3 Sine Shape

a. Derivation of the Model and Algorithm

Appendix A shows the parameters and the pattern used to form the "sine" shape. The coordinate system used in the development of the algorithm is 180^{o} from that shown in the photograph in the appendix. Table 5.3.3-1 gives the norlmalized, raw data. Figures 5.3.3-1 to 5.3.3-4 show the raw data. As can be seen from the graphs, the edge along the $x = +6$ line was clamped. Geometric symmetry dictates that $z(x,y) = -z(x,y)$ and $z(x,y) = z(x,-y)$. Deflections in a direction parallel to the beam passes were found. Their origin has been discussed previously. The clamping complicates the modeling and algorithm formation since it causes violation of the symmetry. Since all the shapes have and will assume unrestrained plates only the half-plate which is unclamped will be used for symmetrizing.

The first attempt to model the plate focussed to fitting a sine curve to the shapes. This proved to be too inaccurate. Instead, the shape was modeled as an antisymmetric double parabola. Table 5.3.3-2 and figure 3.5.3-5 shows the modeled data. The inflection point is approximately at $x,y = 0$. Significant coupling exists between the two sides of the plate. The result is that the portion of the plate containing the line connecting the two sides of the plate (each side irradiated on opposite sides) has an unexpected rate of change of curvature. This area acts as a

X	Y=-6 DEFL ACTUAL	Y=-4 DEFL ACTUAL	Y=-2 DEFL ACTUAL	Y=0 DEFL ACTUAL
-6	-.165	-.078	-.011	.001
-4	-.054	.024	.080	.094
-2	-.003	.046	.097	.108
0	-.072	-.055	-.009	0
2	-.177	-.157	-.132	-.123
4	-.146	-.169	-.148	-.142
6	-.092	-.092	-.077	-.050

X	Y=0 DEFL ACTUAL	Y=2 DEFL ACTUAL	Y=4 DEFL ACTUAL	Y=6 DEFL ACTUAL
-6	.001	-.039	-.106	-.177
-4	.094	.078	.046	-.104
-2	.108	.095	.053	-.040
0	0	-.010	-.038	-.102
2	-.123	-.126	-.148	-.172
4	-.142	-.143	-.150	-.174
6	-.050	-.039	-.060	-.065

Table 5.3.3-1: Raw Deflection Data for the Sine Shape

Figure 5.3.3—1 Raw Deflection Data

for the Sine Shape (Y≥0)

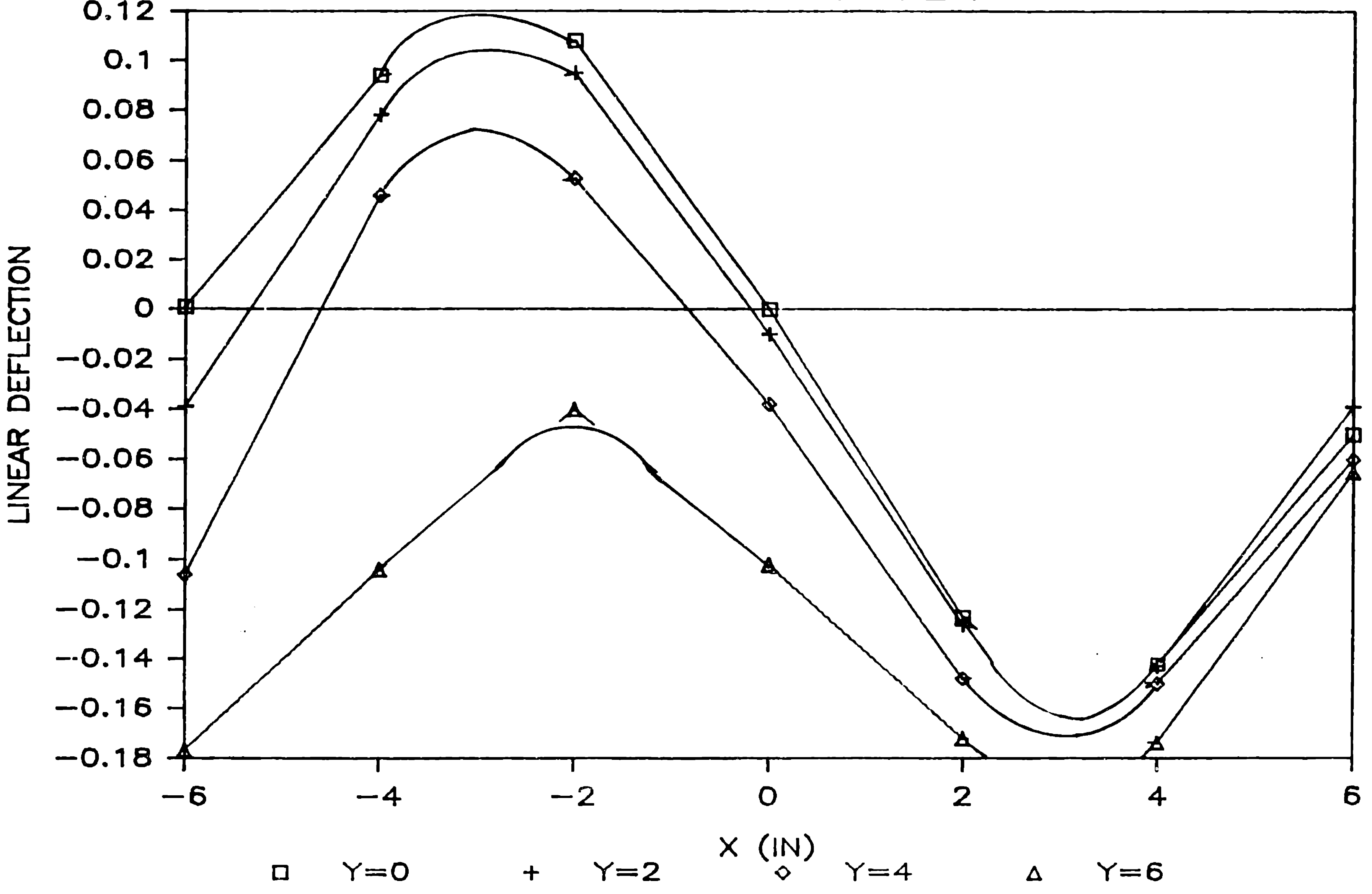

Figure 5.3.3—2 Raw Deflection Data

for the Sine Shape (Y≤0)

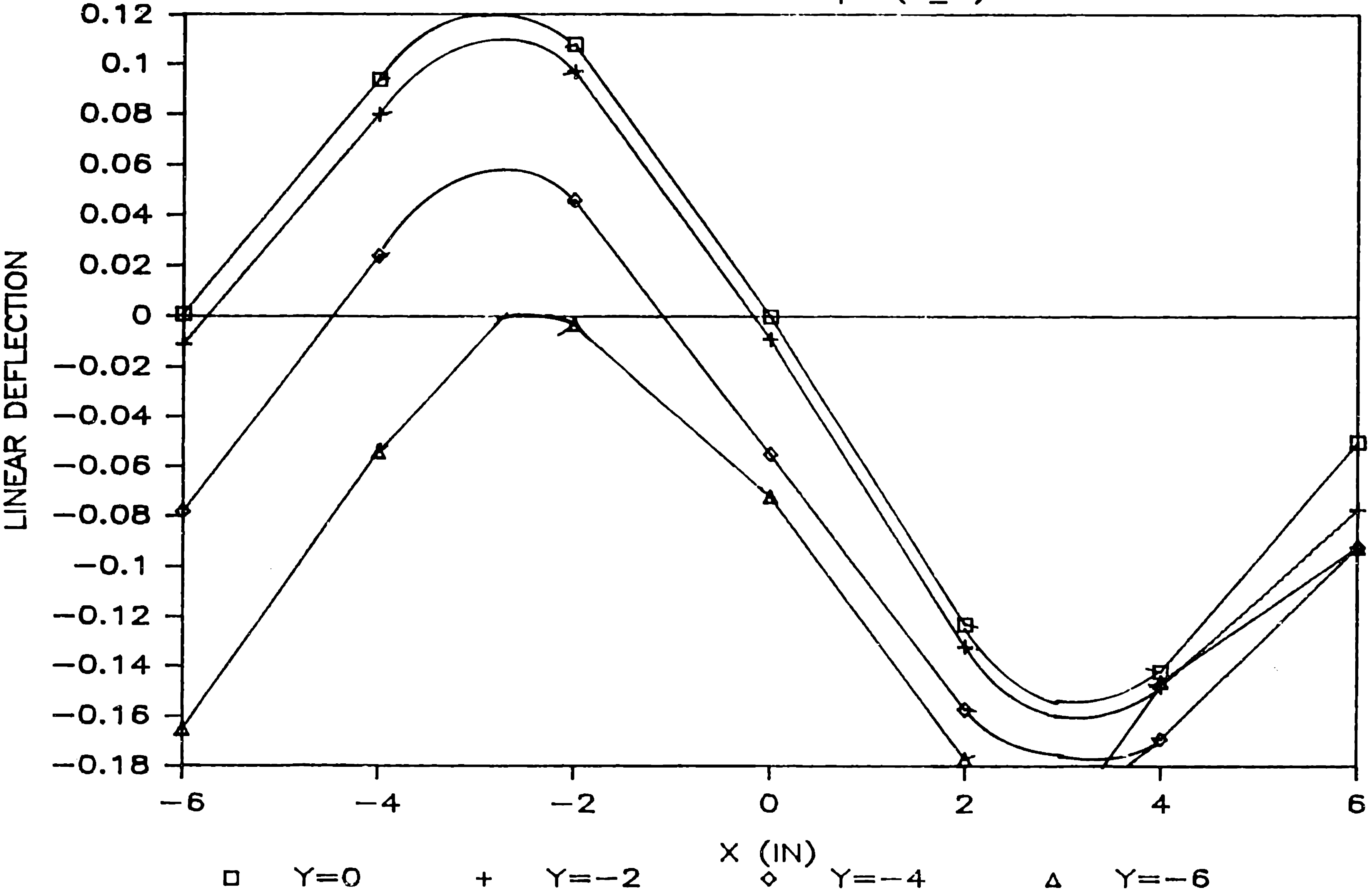

Figure 5.3.3-3 Raw Deflection Data

for the Sine Shape (X≥0)

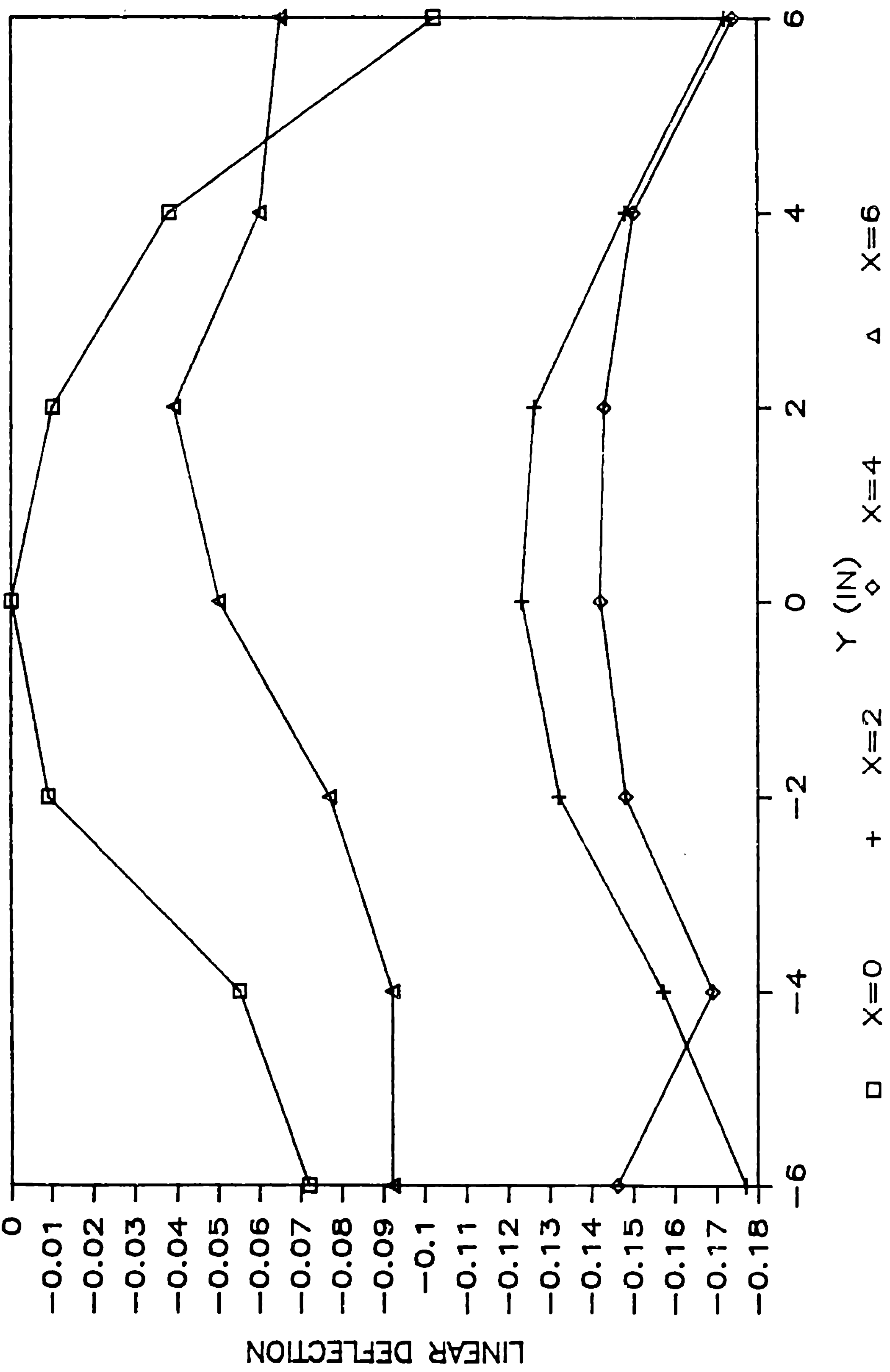

Figure 5.3.3—4 Raw Deflection Data

for the Sine Shape (X<0)

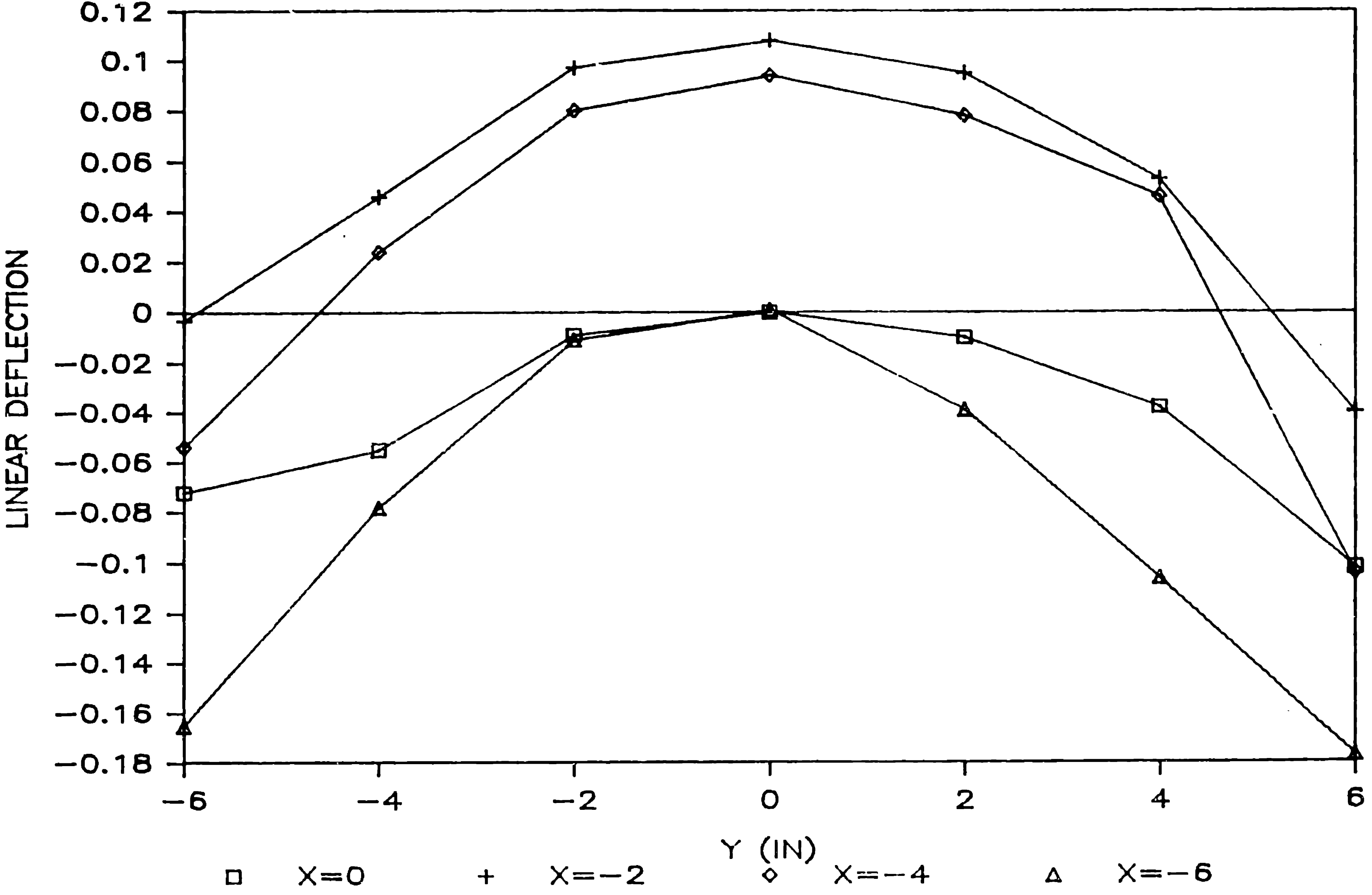

X	Y=-6 DEFL MODEL	Y=-4 DEFL MODEL	Y=-2 DEFL MODEL	Y=0 DEFL MODEL
-6	-0.171	-0.092	-0.025	0
-4	-0.010	0.037	0.080	0.090
-2	0.018	0.060	0.103	0.113
0	-0.085	-0.048	-0.010	0
2	-0.188	-0.156	-0.123	-0.113
4	-0.211	-0.179	-0.146	-0.090
6	-0.171	-0.092	-0.025	0

X	Y=0 DEFL MODEL	Y=2 DEFL MODEL	Y=4 DEFL MODEL	Y=6 DEFL MODEL
-6	0	-0.025	-0.092	-0.171
-4	0.090	0.080	0.037	-0.010
-2	0.113	0.103	0.060	0.018
0	0	-0.010	-0.048	-0.085
2	-0.113	-0.123	-0.156	-0.188
4	-0.090	-0.146	-0.179	-0.211
6	0	-0.025	-0.092	-0.171

Table 5.3.3-2: Model Deflections for the Sine Shape

Figure 5.3.3—5: Model Deflections

for the Sine Shape (Y's are +/—)

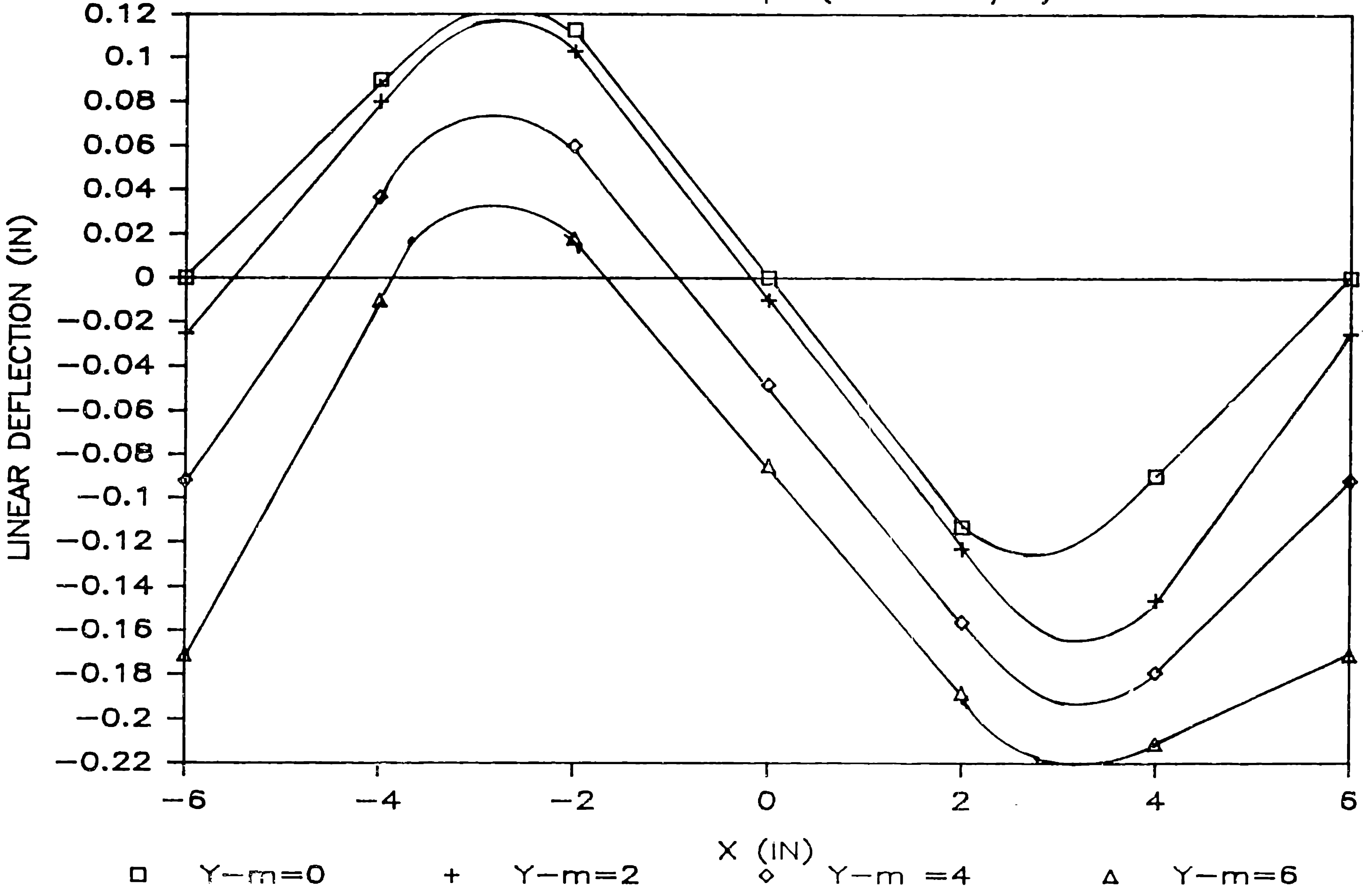

clamp. Therefore, for this reason, the tan(k) parameter must be modified by poisson's ratio from about $x = -BD$ to about $x = +BD$. The tan(k) parameter remains applicable to most of the interior of the plate.

The following equations form the heart of the algorithm for the sine shape:

$$\tan(k) = \tan[(4)(0.7)(100)/(2)(144)] = .0172$$

$$z_a(0,y) = -.25\tan(k)|y| \qquad |y| \le W_y/6$$

$$z_a(0,y) = -\tan(k)[|y| - 15/W_y] \qquad W_y/6 \le |y| \le W_y/2$$

$$z_a(0,y) = z_a(0,-y) \le 0$$

For the "negative" deflection half-cycle:

$$z_a(x,0) = -(1/\nu)\tan(k)x \qquad 0 \le x \le W_x/6$$

$$z_a(x,0) = -\tan(k)[x - W_x(\nu-1)/6\cdot\nu] \qquad W_x/6 \le x \le .94W_x/4$$

$$z_a(x,0) = \tan(k)[x - .846W_x] \qquad .94W_x/4 < x \le \nu\cdot W_x$$

$$z_a(x,0) = \frac{\tan(k)}{1.18\cdot\nu}[x - W_x/2] \qquad \nu\cdot W_x < x \le W_x/2$$

For all regions:

$$z_a(-x,0) = -z_a(x,0)$$

b. Comparison of the Algorithm, Model, and Measured Deflections

Table 5.3.3-3 gives the results of the algorithm and the model with their deviations. Note that this algorithm is somewhat inaccurate for computing the values at the edges. This is in part due to the clamping effect discussed earlier. The average deviation more than one beam diameter from the edges is 9.2%. Figures 5.3.3-6 and 5.3.3-7 show the model and algorithm deflections for x,y = 0. Figure 5.3.3-8 shows the model and algorithm deflections for x,y not equal to zero. The +/- y contour deflections for a given x are the same value for both the algorithm and model. Figures 5.3.3-9 and 5.3.3-10 show a comparison of the actual and algorithm deflections. Since the x = +6 edge is clamped which distorts the actual deflections, only the x < 0 deflections are compared. Figures 5.3.3-11 and 5.3.3-12 are 3-D plots of the sine shape.

X	Y (+/-)	Z-mdl (IN)	Z-alg (IN)	DEVIATION %
-6	0	.000	.000	0
-4	0	.090	.097	7.2
-2	0	.113	.115	1.7
0	0	.000	.000	0
2	0	-.113	-.155	1.7
4	0	-.090	-.097	7.2
6	0	.000	.000	0
-6	2	-.025	-.009	64
-4	2	.080	.089	10
-2	2	.103	.106	2.8
0	2	-.010	-.009	1.0
2	2	-.123	-.123	0
4	2	-.146	-.106	27
6	2	-.025	-.009	64

Table 5.3.3-3: Model and Algorithm Deflection for the Sine

X	Y (+/-)	Z-mdl (IN)	Z-alg (IN)	DEVIATION %
-6	4	-.092	-.043	53
-4	4	.037	.054	31
-2	4	.060	.072	16.7
0	4	-.048	-.043	8.5
2	4	-.156	-.158	1.2
4	4	-.179	-.140	21.8
6	4	-.092	-.043	53
-6	6	-.171	-.077	55
-4	6	-.010	.175	105
-2	6	.018	.037	51
0	6	-.085	-.077	9.4
2	6	-.188	-.192	2.1
4	6	-.211	-.175	17.1
6	6	-.171	-.077	55

Table 5.3.3-3: Model & Algorithm Defl. for Sine (cont)

Figure 5.3.3—6: Model and Algorithm

Deflections for the Sine at Y=0

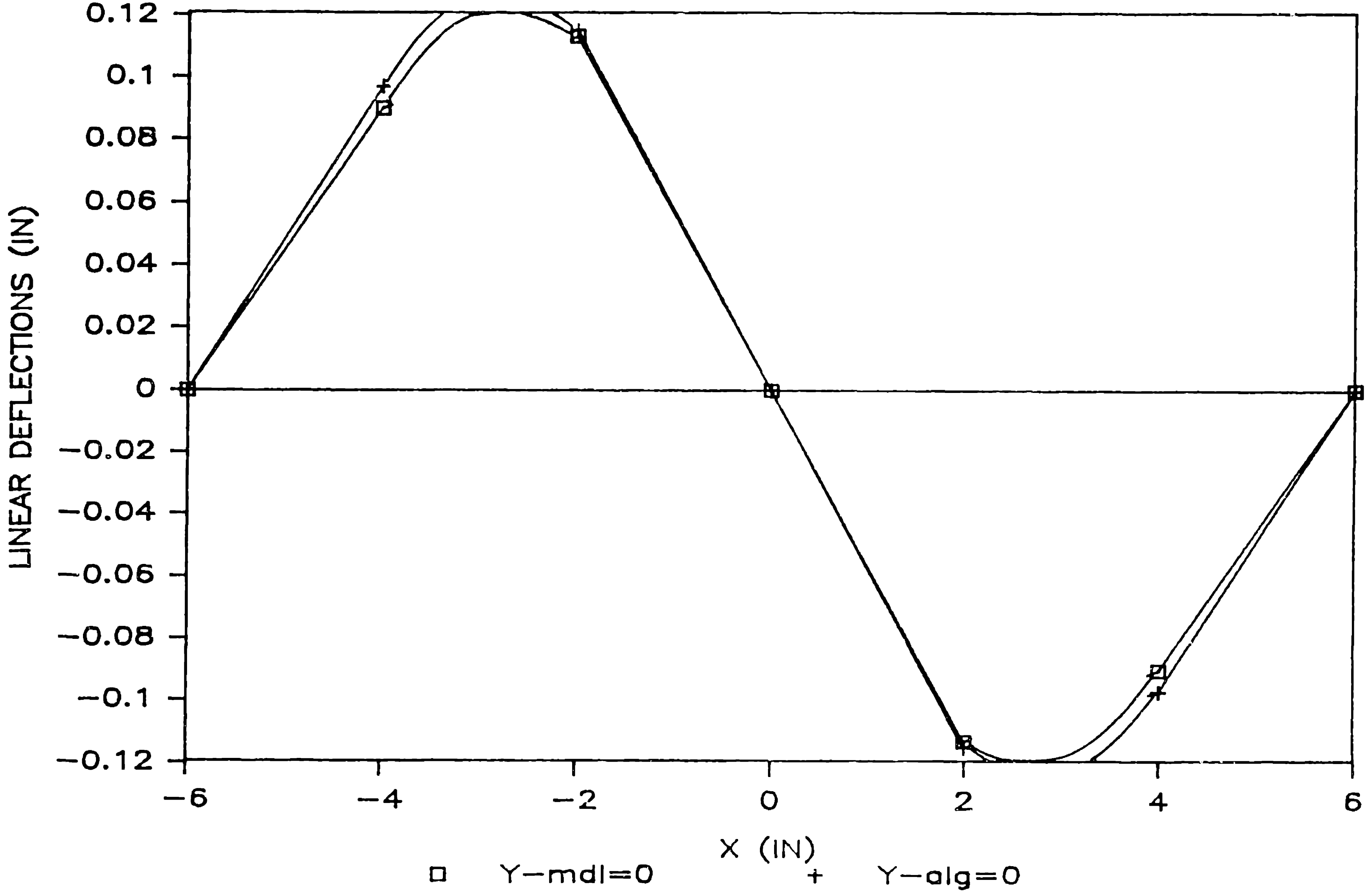

Figure 5.3.3—7: Model and Algorithm

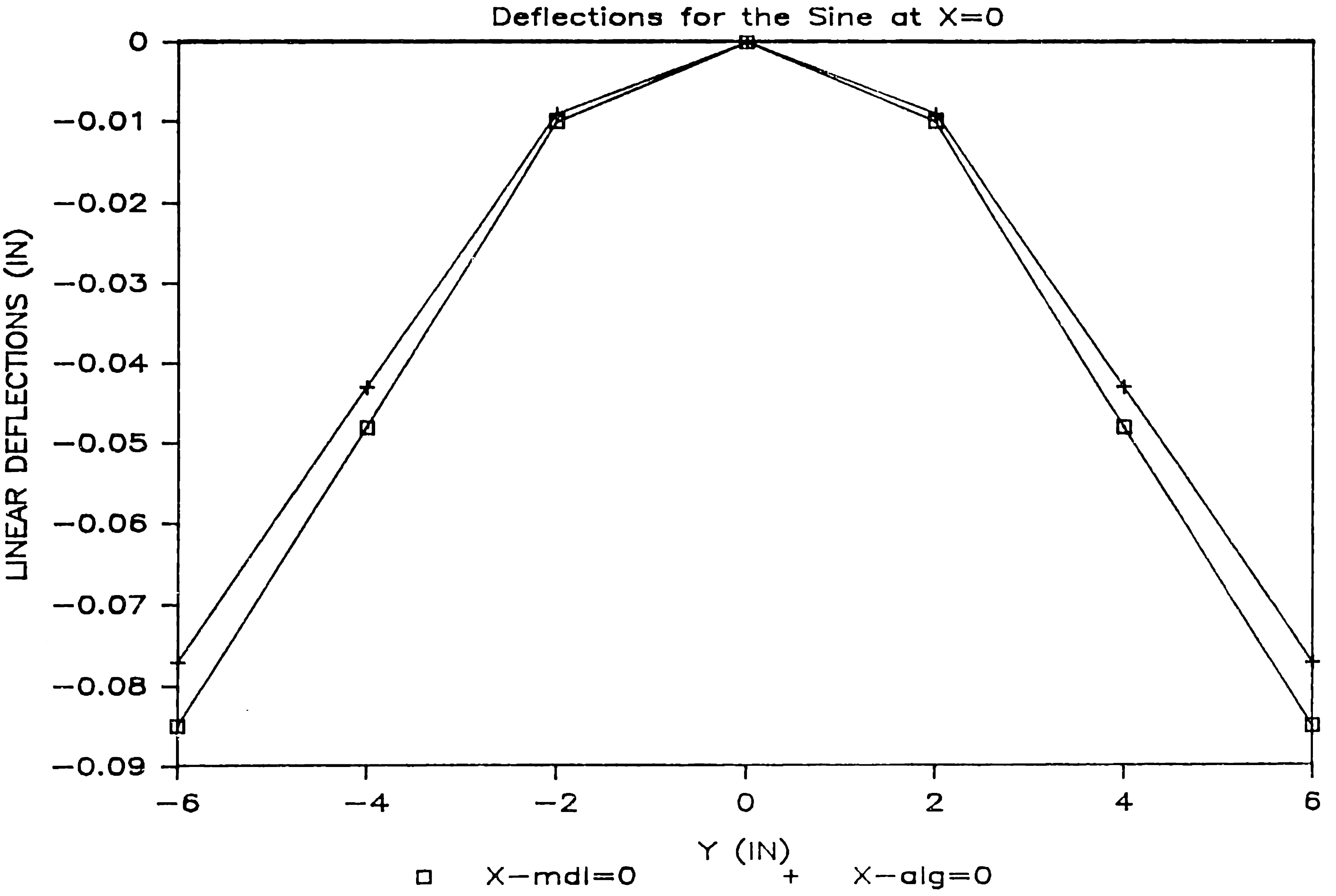

Figure 5.3.3—8: Model and Algorithm

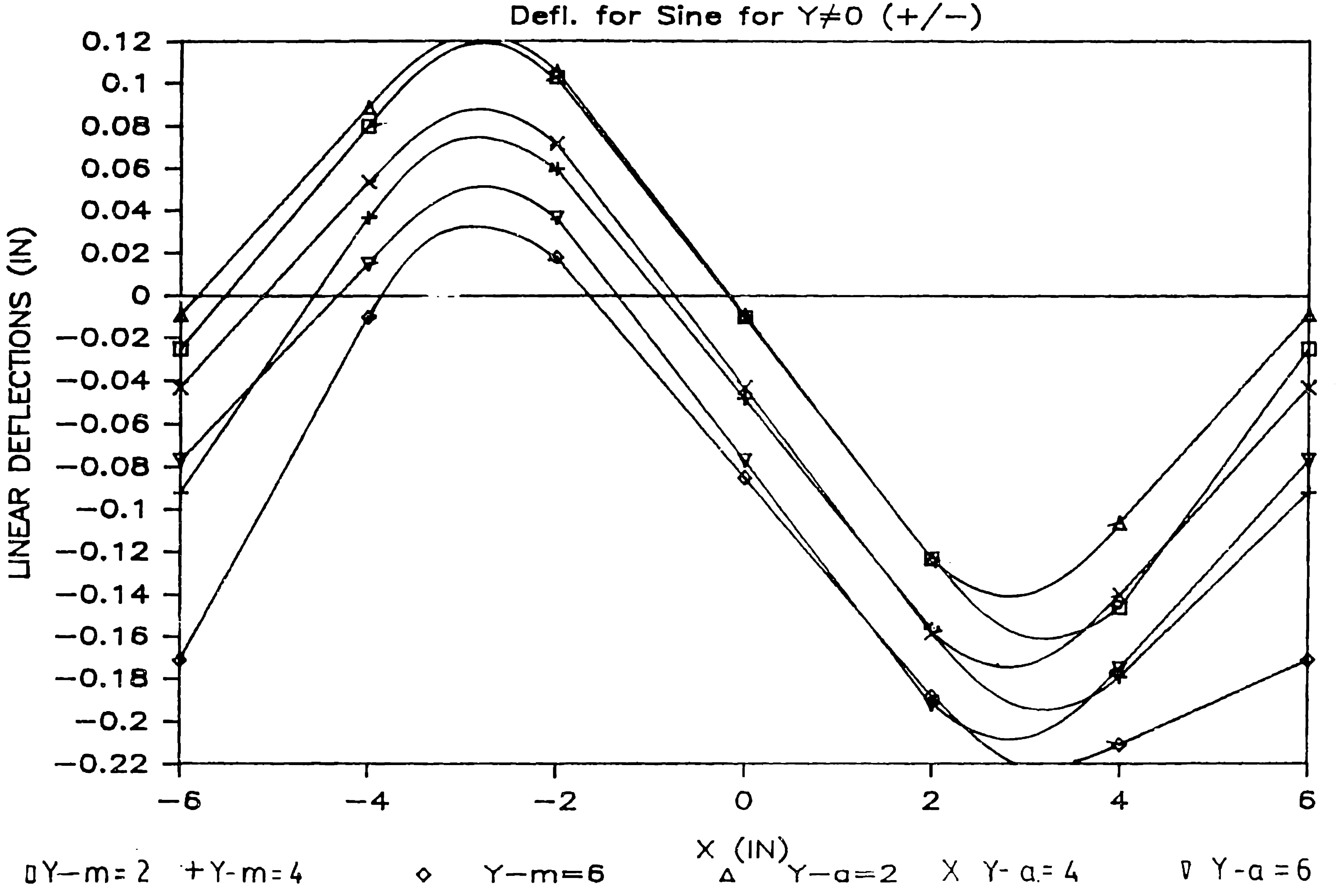

Figure 5.3.3—9: Algorithm & Actual

Deflection for the Sine (Y>0)

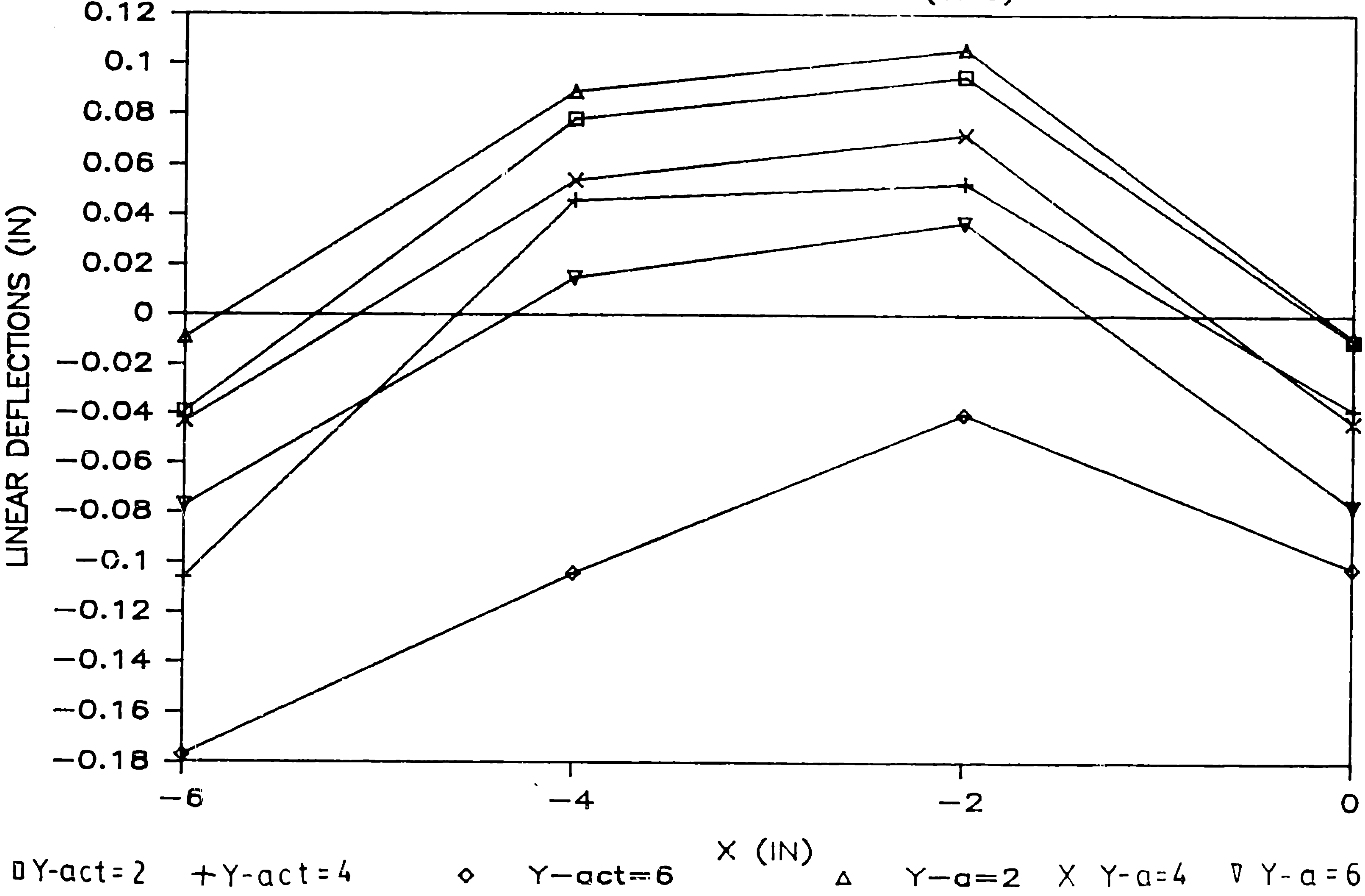

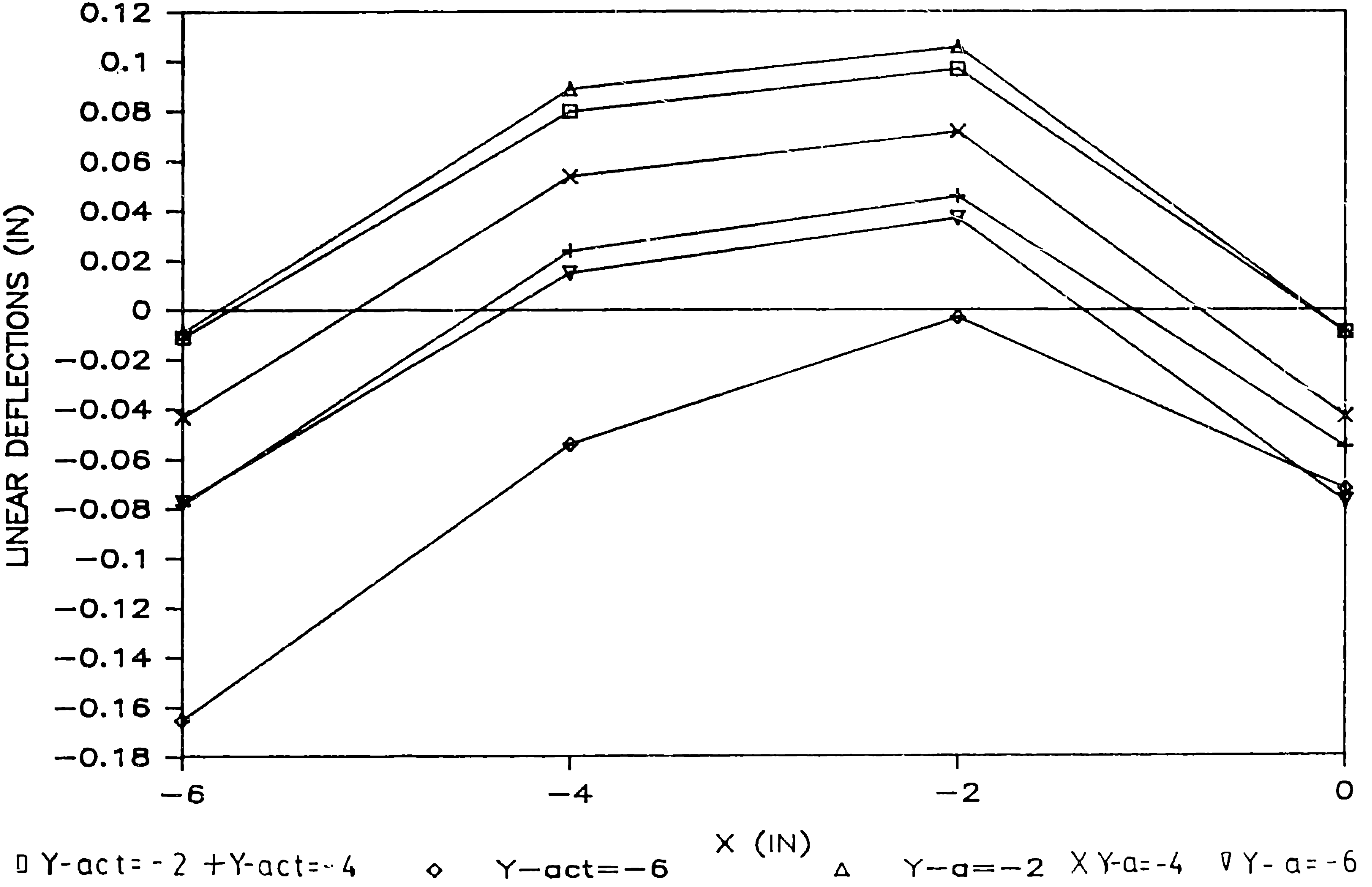

Figure 5.3.3—10: Algorithm & Actual
Deflection for the Sine (Y<0)

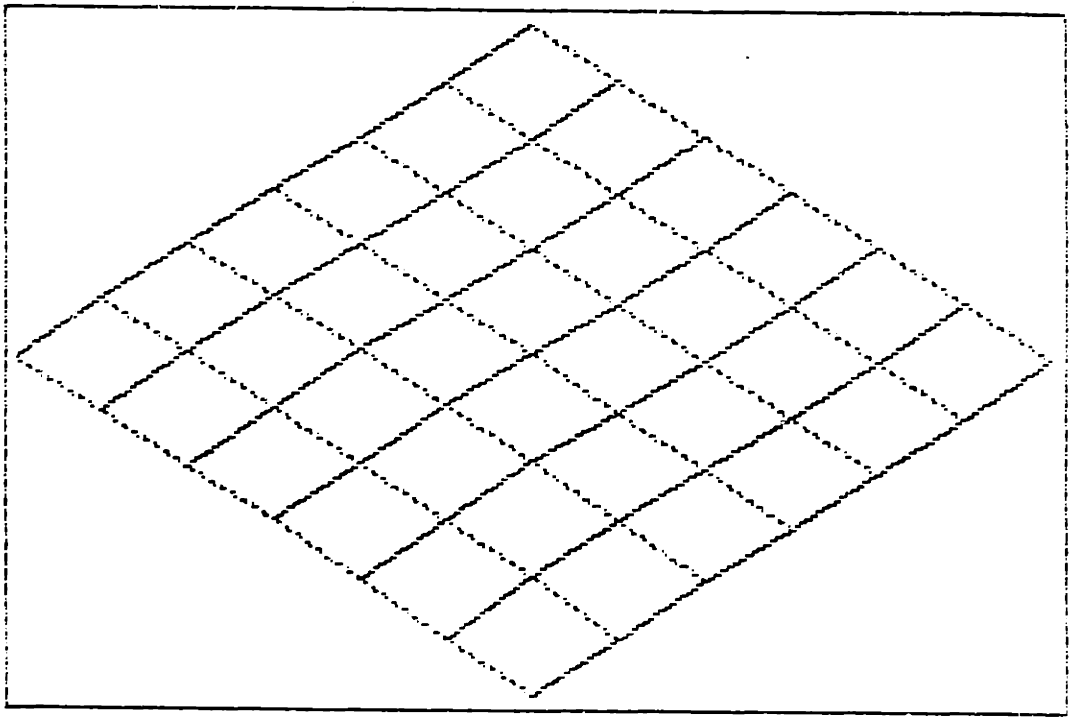

Figure 5.3.3-11: 3-D Perspective of the Sine Shape with Actual Deflections

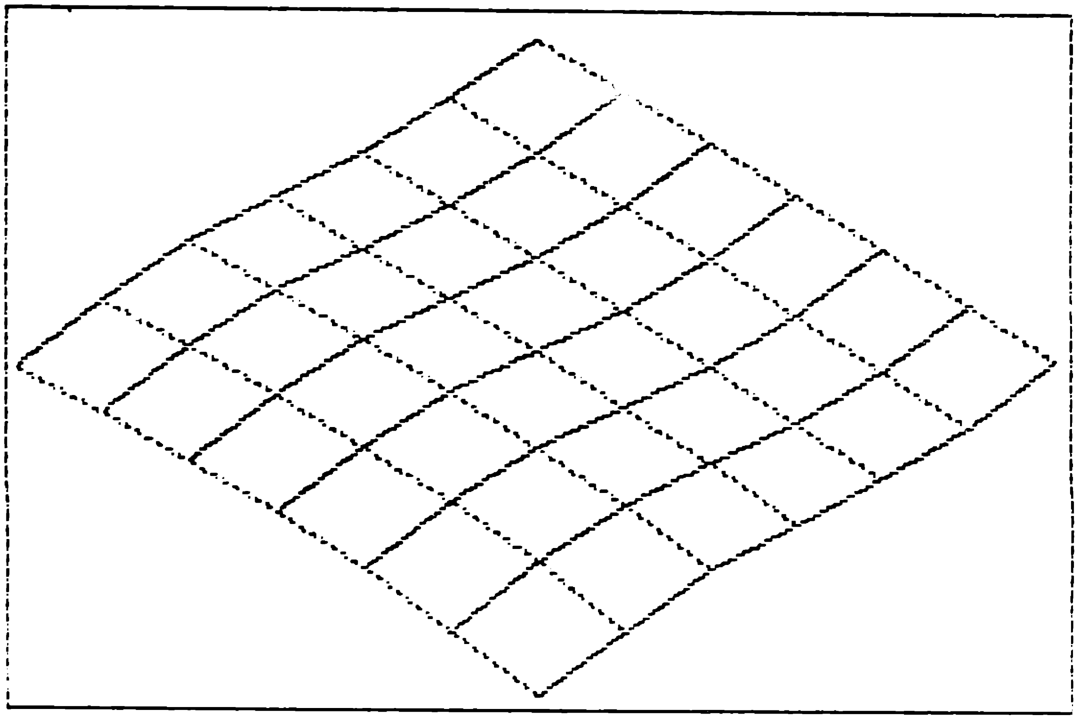

Figure 5.3.3-12: 3-D Perspective of the Sine Shape with Deflections Magnified by 3 Times

5.3.4 Saddle Shape

a. Derivation of the Model and Algorithm

Appendix A shows the parameters and pattern in which the plate was fabricated. Table 5.3.4-1 and figures 5.3.4-1 to 5.3.4-4 show the actual normalized deflections. For this shape, symmetry dictates that $z(x,y) = z(-x,y)$ and $z(x,y) = z(x,-y)$. Using the above rules of symmetry and the general methodology utilyzed for the other shapes, the model deflection data was determined and is given in table 5.3.4-2 and shown in figure 5.3.4-5.

Ideally, since the power delivered to each side of the plate is the same, the magnitudes of the deflections should be the same. This is not the case. The magnitudes of the deflections of the $X = 0$ contour are much more than predicted from the tan(k) parameter or superposition. It is believed that the poisson effect which has been discussed is responsible. The "top" plate irradiation imposes longitudinal deflections which enhance the deflections during the "bottom" plate irradiation. Therefore, the side which has been irradiated second will have more deflection than predicted by superposition or tan(k) for single side irradiation. This increase should be predictable from poisson's ratio and, in fact, the plate can be reasonably modeled over much of the area by assuming a multiplicative $(1 + \nu)$ factor with tan(k). It appears from the data that the second side passes do not reduce the first side ($y = 0$ contour)

X	Y=-5 DEFL ACTUAL	Y=-4 DEFL ACTUAL	Y=-3 DEFL ACTUAL	Y=-2 DEFL ACTUAL	Y=-1 DEFL ACTUAL	Y=0 DEFL ACTUAL
-5	-0.164	-0.052	0.158	0.174	0.258	0.237
-4	-0.198	-0.072	0.055	0.115	0.167	0.161
-3	-0.264	-0.127	-0.035	0.040	0.094	0.117
-2	-0.352	-0.186	-0.108	-0.036	0.031	0.039
-1	-0.403	-0.239	-0.152	-0.071	-0.010	0.004
0	-0.402	-0.275	-0.166	-0.078	-0.022	0.000
1	-0.401	-0.264	-0.164	-0.074	-0.007	0.012
2	-0.376	-0.241	-0.136	-0.036	0.023	0.044
3	-0.315	-0.195	-0.082	0.005	0.070	0.095
4	-0.240	-0.121	-0.010	0.077	0.117	0.156
5	-0.186	-0.065	0.021	0.104	0.157	0.215

X	Y=0 DEFL ACTUAL	Y=1 DEFL ACTUAL	Y=2 DEFL ACTUAL	Y=3 DEFL ACTUAL	Y=4 DEFL ACTUAL	Y=5 DEFL ACTUAL
-5	0.237	0.227	0.167	0.137	0.023	-0.068
-4	0.161	0.147	0.126	0.037	-0.066	-0.145
-3	0.117	0.085	0.055	-0.031	-0.139	-0.225
-2	0.039	0.009	-0.023	-0.090	-0.191	-0.303
-1	0.004	-0.015	-0.057	-0.132	-0.241	-0.358
0	0.000	-0.018	-0.057	-0.132	-0.242	-0.371
1	0.012	-0.003	-0.043	-0.111	-0.231	-0.352
2	0.044	0.036	-0.001	-0.071	-0.181	-0.298
3	0.095	0.102	0.067	-0.002	-0.107	-0.235
4	0.156	0.155	0.150	0.085	-0.030	-0.132
5	0.215	0.214	0.192	0.165	0.032	-0.075

Table 5.3.4-1: Raw Deflection Data for the Saddle Shape

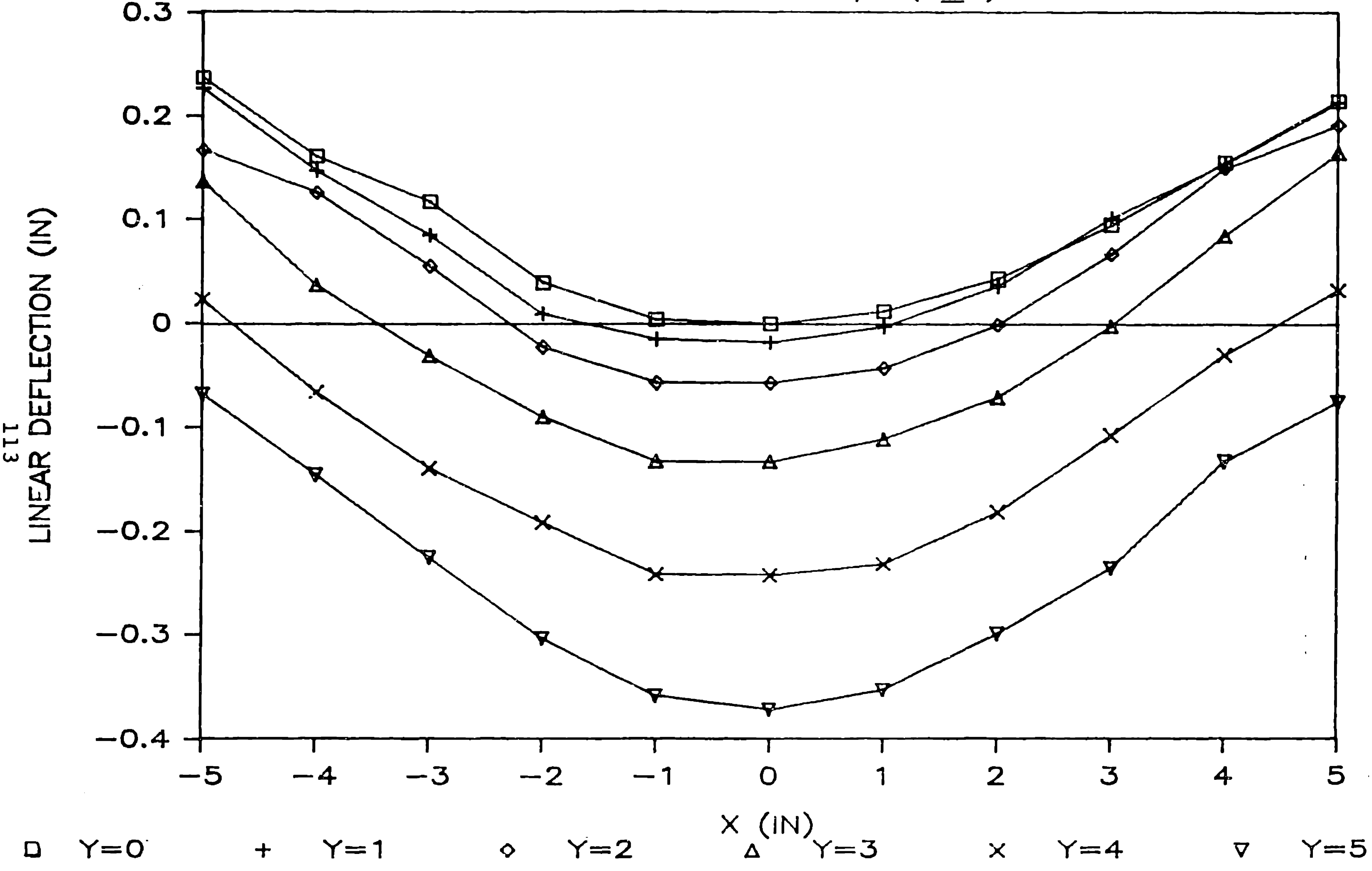

Figure 5.3.4—1: Raw Deflection Data
for the Saddle Shape (Y≥0)

Figure 5.3.4—2: Raw Deflection Data
for the Saddle Shape (Y≤0)

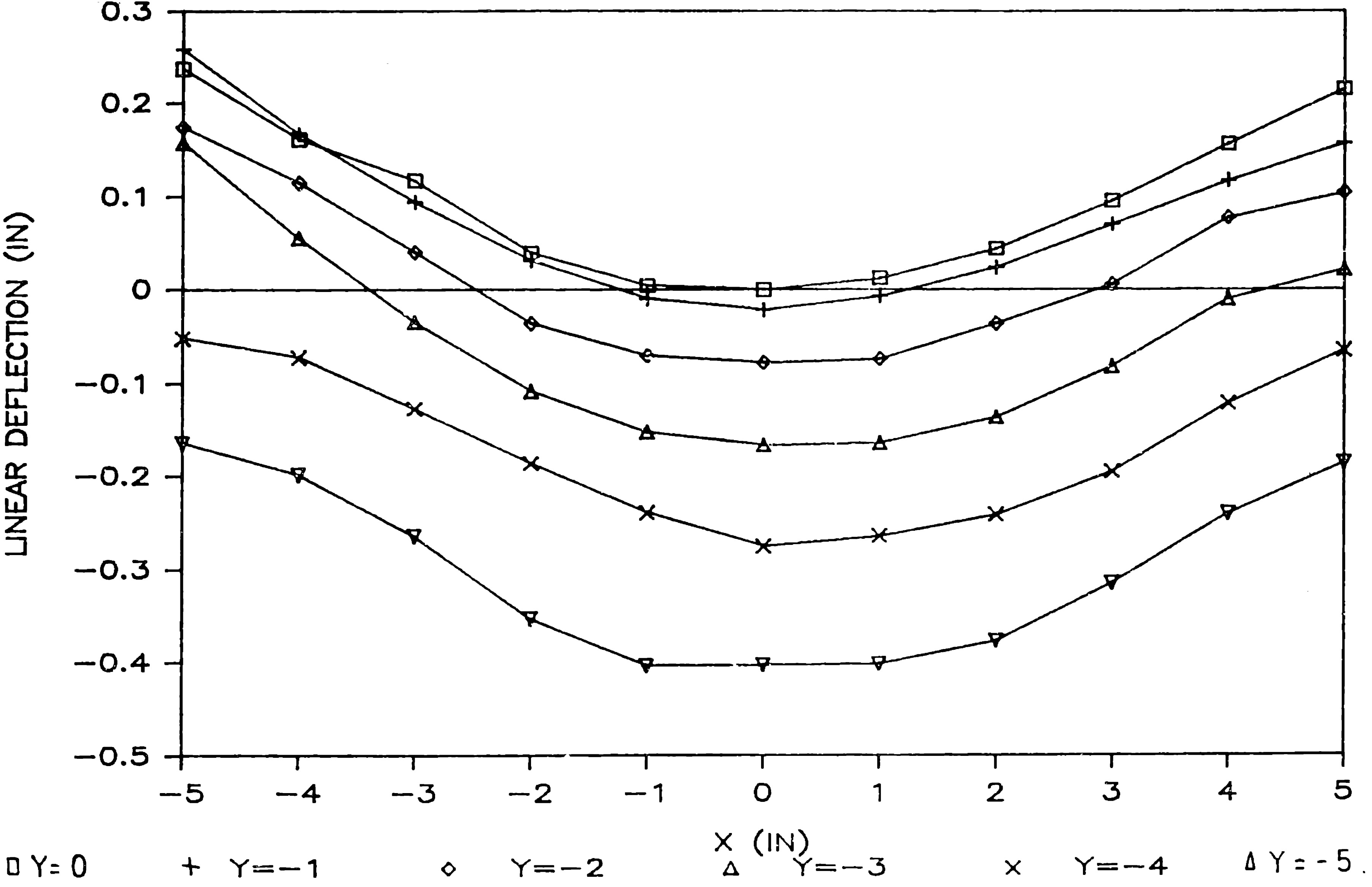

Figure 5.3.4—3: Raw Deflection Data

for the Saddle Shape (X≥0)

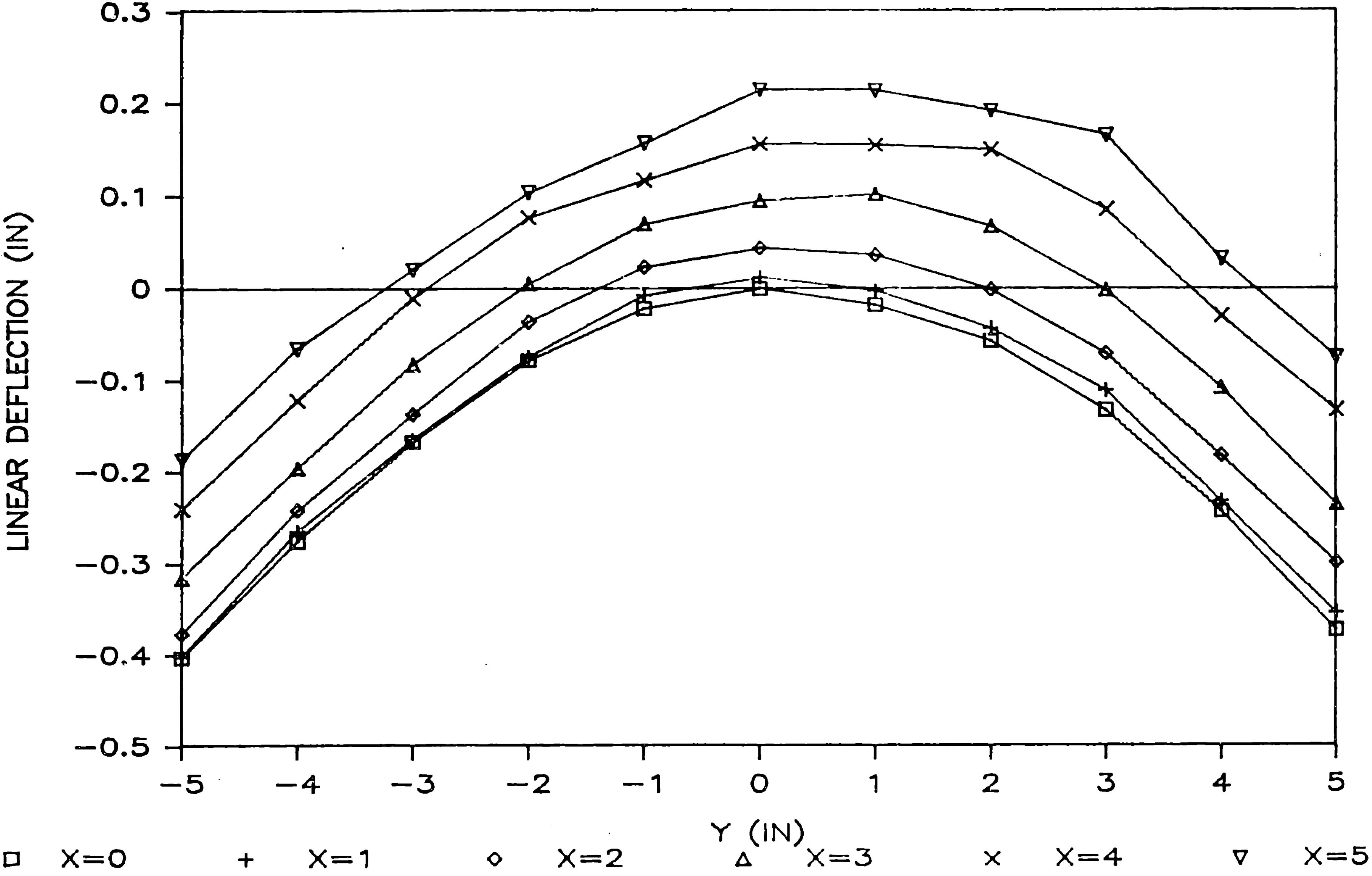

Figure 5.3.4—4: Raw Deflection Data

for the Saddle Shape (X≤0)

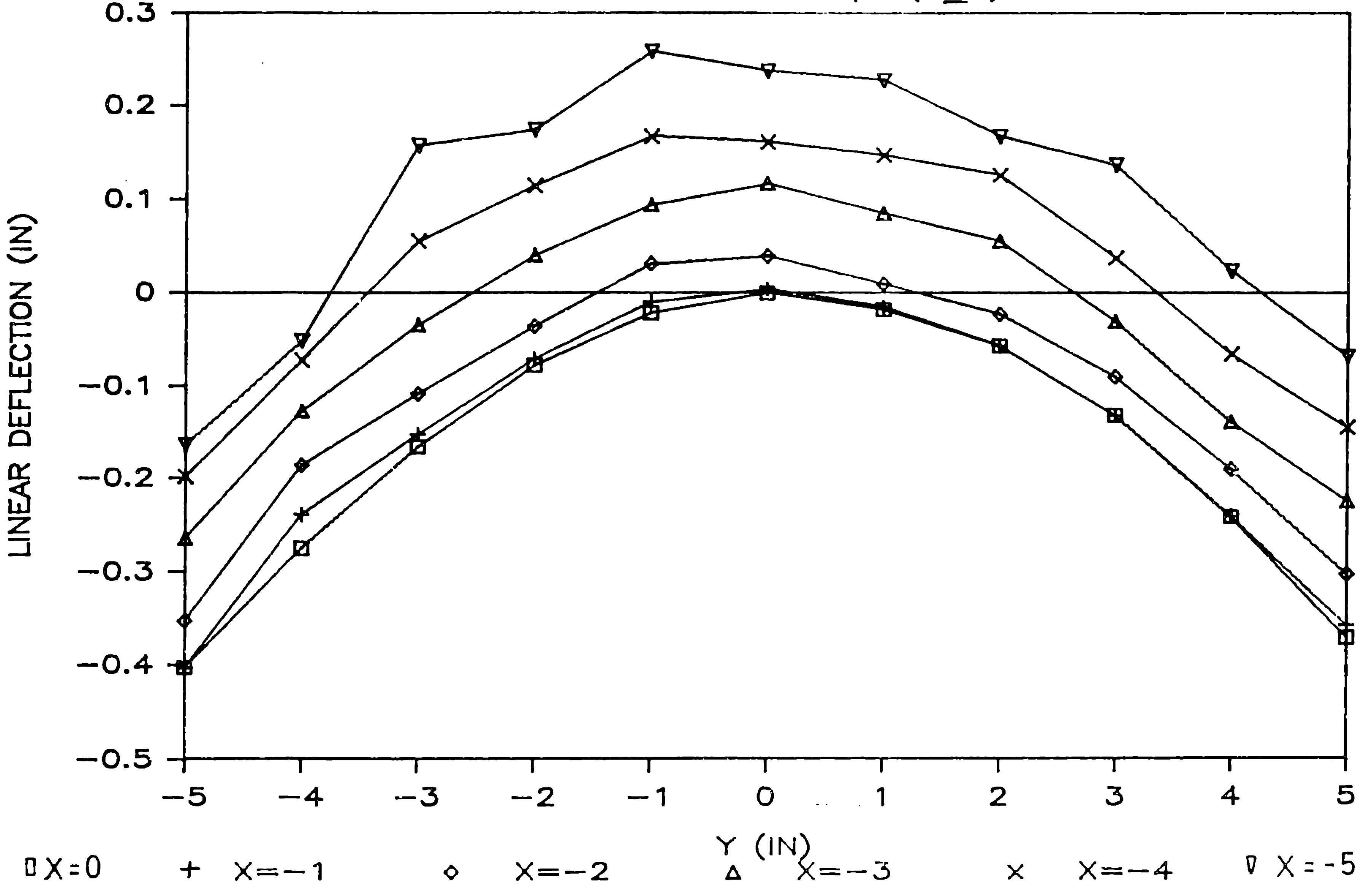

X	Y=-5 DEFL MODEL	Y=-4 DEFL MODEL	Y=-3 DEFL MODEL	Y=-2 DEFL MODEL	Y=-1 DEFL MODEL	Y=0 DEFL MODEL
-5	-0.123	0.011	0.132	0.186	0.215	0.226
-4	-0.190	-0.072	0.042	0.102	0.147	0.165
-3	-0.260	-0.142	-0.038	0.033	0.088	0.106
-2	-0.332	-0.200	-0.101	-0.024	0.025	0.042
-1	-0.379	-0.244	-0.140	-0.061	-0.009	0.008
0	-0.387	-0.258	-0.149	-0.068	-0.020	0.000
1	-0.379	-0.244	-0.140	-0.061	-0.009	0.008
2	-0.332	-0.200	-0.101	-0.024	0.025	0.042
3	-0.260	-0.142	-0.038	0.033	0.088	0.106
4	-0.190	-0.072	0.042	0.102	0.147	0.165
5	-0.123	0.011	0.132	0.186	0.215	0.226

X	Y=0 DEFL MODEL	Y=1 DEFL MODEL	Y=2 DEFL MODEL	Y=3 DEFL MODEL	Y=4 DEFL MODEL	Y=5 DEFL MODEL
-5	0.226	0.215	0.186	0.132	0.011	-0.123
-4	0.165	0.147	0.102	0.042	-0.072	-0.190
-3	0.106	0.088	0.033	-0.038	-0.142	-0.260
-2	0.042	0.025	-0.024	-0.101	-0.200	-0.332
-1	0.008	-0.009	-0.061	-0.140	-0.244	-0.379
0	0.000	-0.020	-0.068	-0.149	-0.258	-0.387
1	0.008	-0.009	-0.061	-0.140	-0.244	-0.379
2	0.042	0.025	-0.024	-0.101	-0.200	-0.332
3	0.106	0.088	0.033	-0.038	-0.142	-0.260
4	0.165	0.147	0.102	0.042	-0.072	-0.190
5	0.226	0.215	0.186	0.132	0.011	-0.123

Table 5.3.4-2: Model Deflections for the Saddle Shape

Figure 5.3.4—5: Model Deflections

for the Saddle Shape (Y's are +/−)

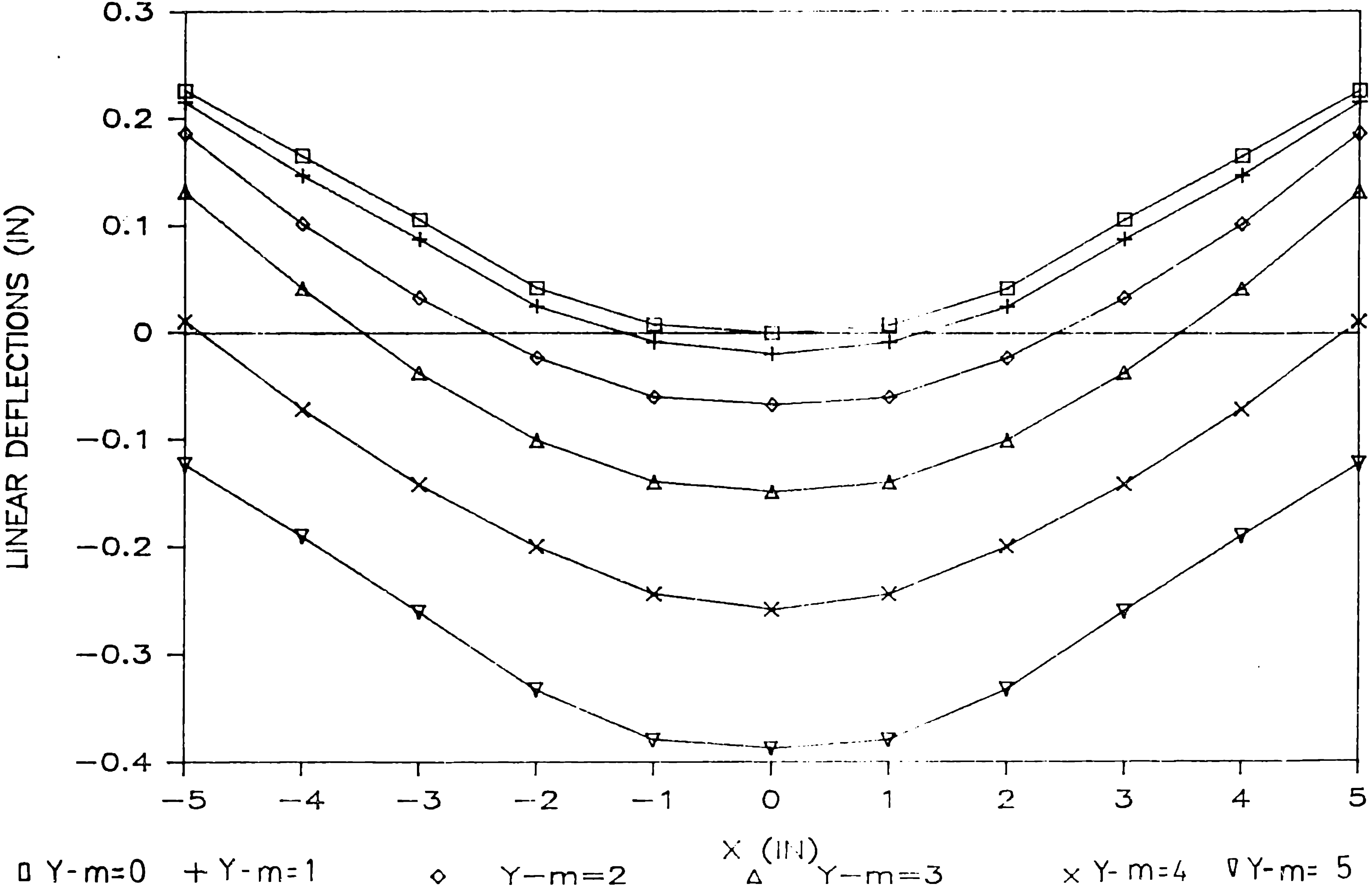

deflections which are reasonably modeled by the tan(k) parameter. Perhaps, the reason is that the process has insufficient power to overcome the high longitudinal residual stresses imposed during the "top" plate irradiation. On the other hand no such stresses oppose the longitudinal bending during the first series of passes.

The algorithm equations become:

$$\tan(k) = \tan[(16)(0.7)(.64)/2] = 0.0626$$

$$z_a(x,0) = .5[.33\tan(k)]|x| \qquad |x| = 0.1W_x$$

$$z_a(0,y) = .5[(\quad)^{.5}\tan(k)]|y| \qquad |y| = 0.1W_y$$

$$z_a(x,0) = .33\tan(k)|x| \qquad 0.1 \le |x| \le 0.2W_x$$

$$z_a(0,y) = (\nu)^{.5}\tan(k)|y| \qquad 0.1 \le |y| \le 0.2W_y$$

$$z_a(x,0) = \tan(k)[|x| - .4W_x/3] \qquad .2W_x < |x| \le .5W_x$$

$$z_a(0,y) = (1+\nu)\tan(k)[|y| - .2W_y(1 - \frac{(\nu)^{.5}}{1+\nu})] \text{ for}$$

$$.2W_y < |y| \le .4W_y$$

$$z_a(0,y) = (\nu)^{.5}\tan(k)[|y| + .2W_y \cdot C] \text{ where}$$

$$C = (\nu)^{.5} + (\nu)^{1.5} + (\nu) - 2 \text{ for}$$

$$.4W_y < |y| \le .5W_y$$

$$z_a(x,y) = z_a(-x,y); \quad z_a(x,y) = z_a(x,-y)$$

b. Comparison of the Algorithm, Model, and Measured Deflections

Table 5.3.4-3 shows the predicted and model deflections. Average deviation is 10.6%. The average deviation on the plate greater than a distance of about 2/3 BD from the edges is 9%. Figures 5.3.4-6 to 5.3.4-8 compare the results of the algorithm and the model. Figures 5.3.4-9 and 5.3.4-10 compare the results of the algorithm with the actual deflections. Figures 5.3.4-11 and 5.3.4-12 are 3-D perspectives of the saddle shape.

X (+/-)	Y (+/-)	Z-mdl (IN)	Z-alg (IN)	DEVIATION %
0	0	.000	.000	0
1	0	.008	.010	20
2	0	.042	.042	0
3	0	.106	.104	1.9
4	0	.165	.167	1.2
5	0	.226	.230	1.7
0	1	-.020	-.017	15
1	1	-.009	-.007	22
2	1	.025	.025	0
3	1	.088	.087	1.1
4	1	.147	.150	2.0
5	1	.215	.213	0.9
0	2	-.068	-.069	1.4
1	2	-.061	-.061	0
2	2	-.024	-.027	11.1
3	2	.033	.037	10.8
4	2	.102	.096	5.9
5	2	.186	.157	15

Table 5.3.4-3: Model and Algorithm Deflections for the Saddle

X (+/-)	Y (+/-)	Z-mdl (IN)	Z-alg (IN)	DEVIATION %
0	3	-.149	-.150	0.7
1	3	-.140	-.142	1.4
2	3	-.101	-.108	6.5
3	3	-.038	-.044	13.6
4	3	.042	.015	64
5	3	.132	.076	42
0	4	-.258	-.231	10.5
1	4	-.244	-.223	8.6
2	4	-.200	-.189	5.5
3	4	-.142	-.125	12
4	4	-.072	-.066	8.3
5	4	.011	.005	54
0	5	-.387	-.346	10.6
1	5	-.379	-.338	10.8
2	5	-.332	-.304	8.4
3	5	-.260	-.240	7.7
4	5	-.190	-.181	4.7
5	5	-.123	-.120	2.4

Table 5.3.4-3: Model & Algorithm Defl. for the Saddle (cont)

Figure 5.3.4—6: Algorithm & Model

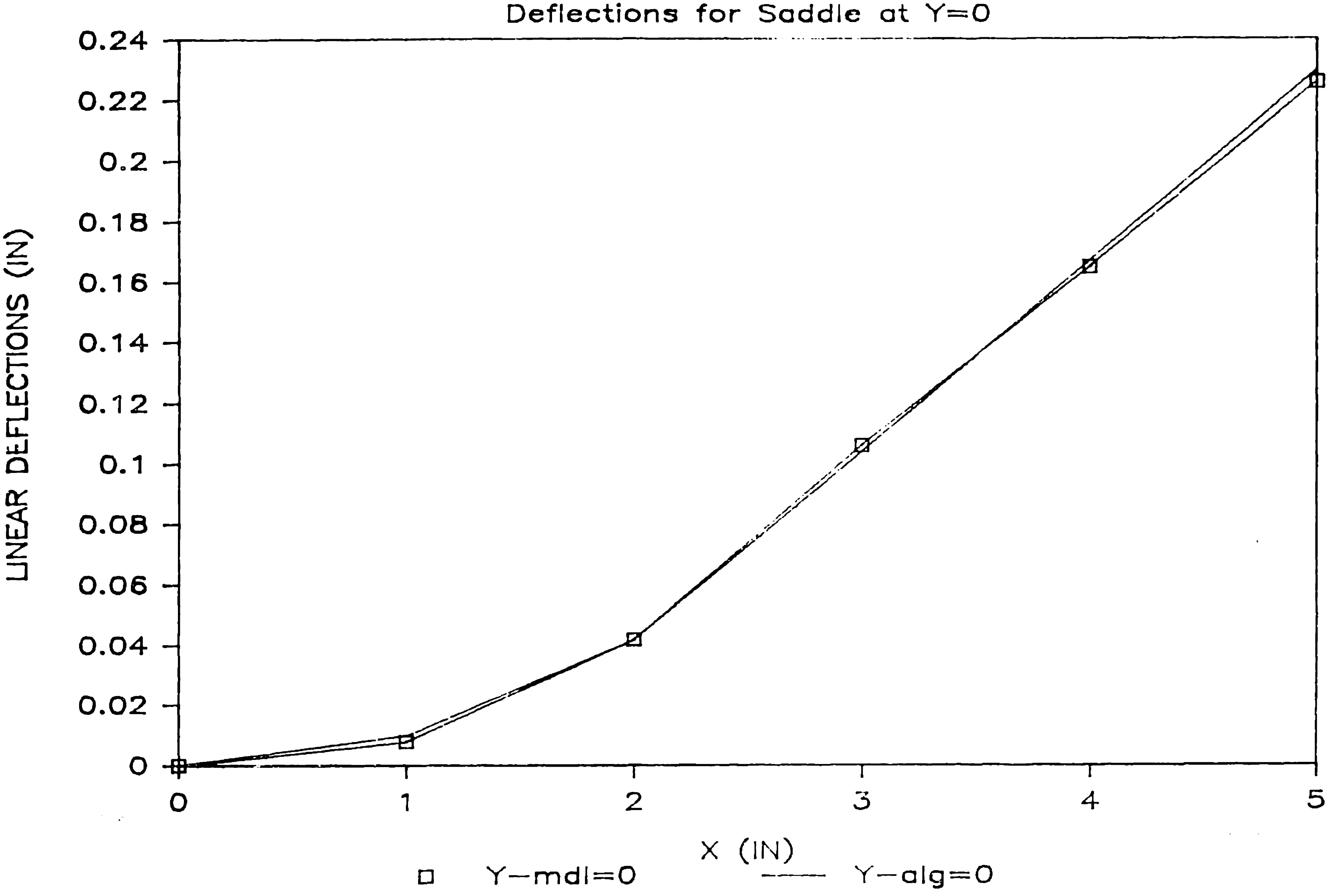

Figure 5.3.4—7: Algorithm & Model

Deflections for Saddle at X=0

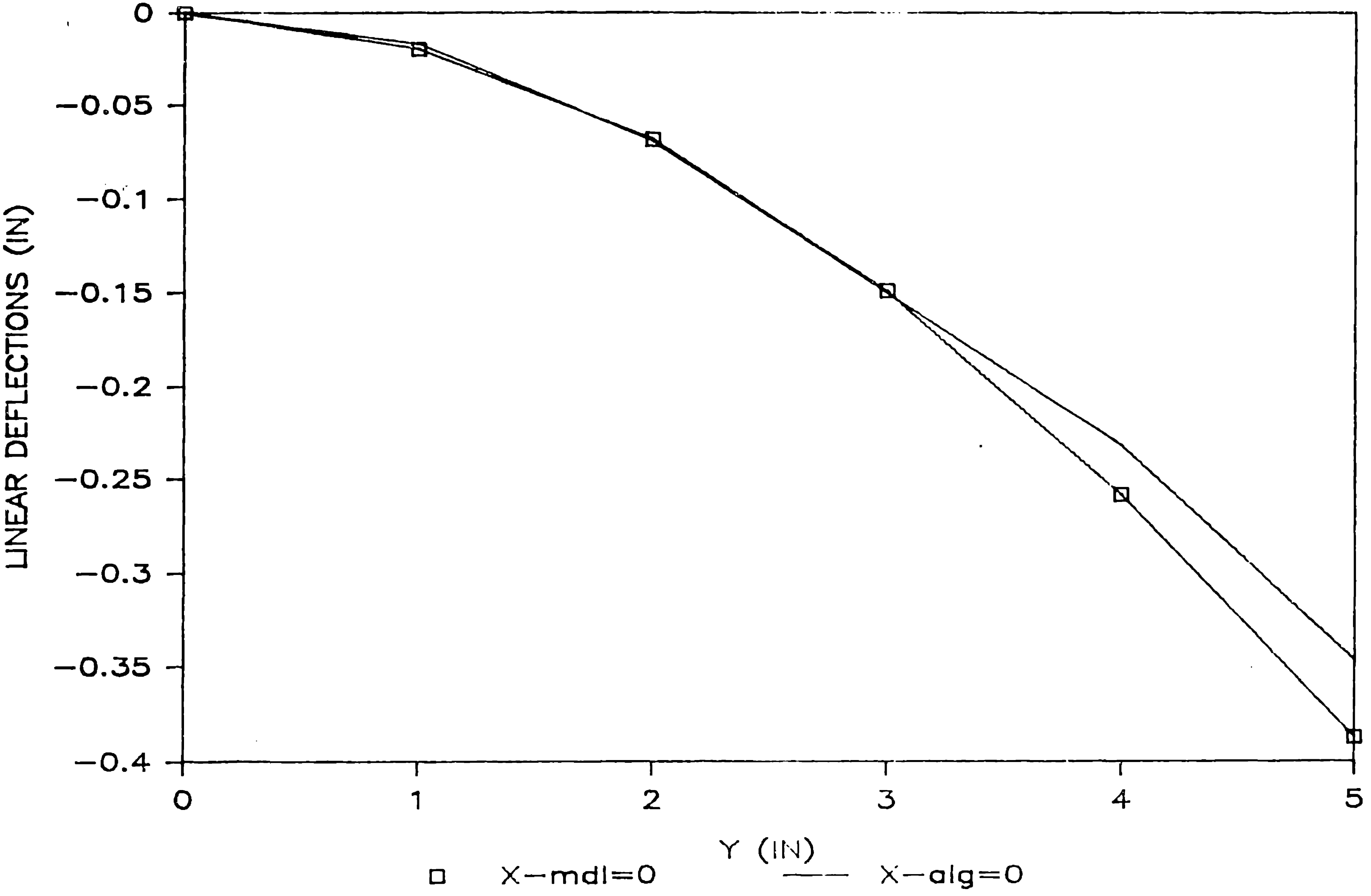

Figure 5.3.4—8: Algorithm & Model

Deflections for Saddle (Y'S are +/−)

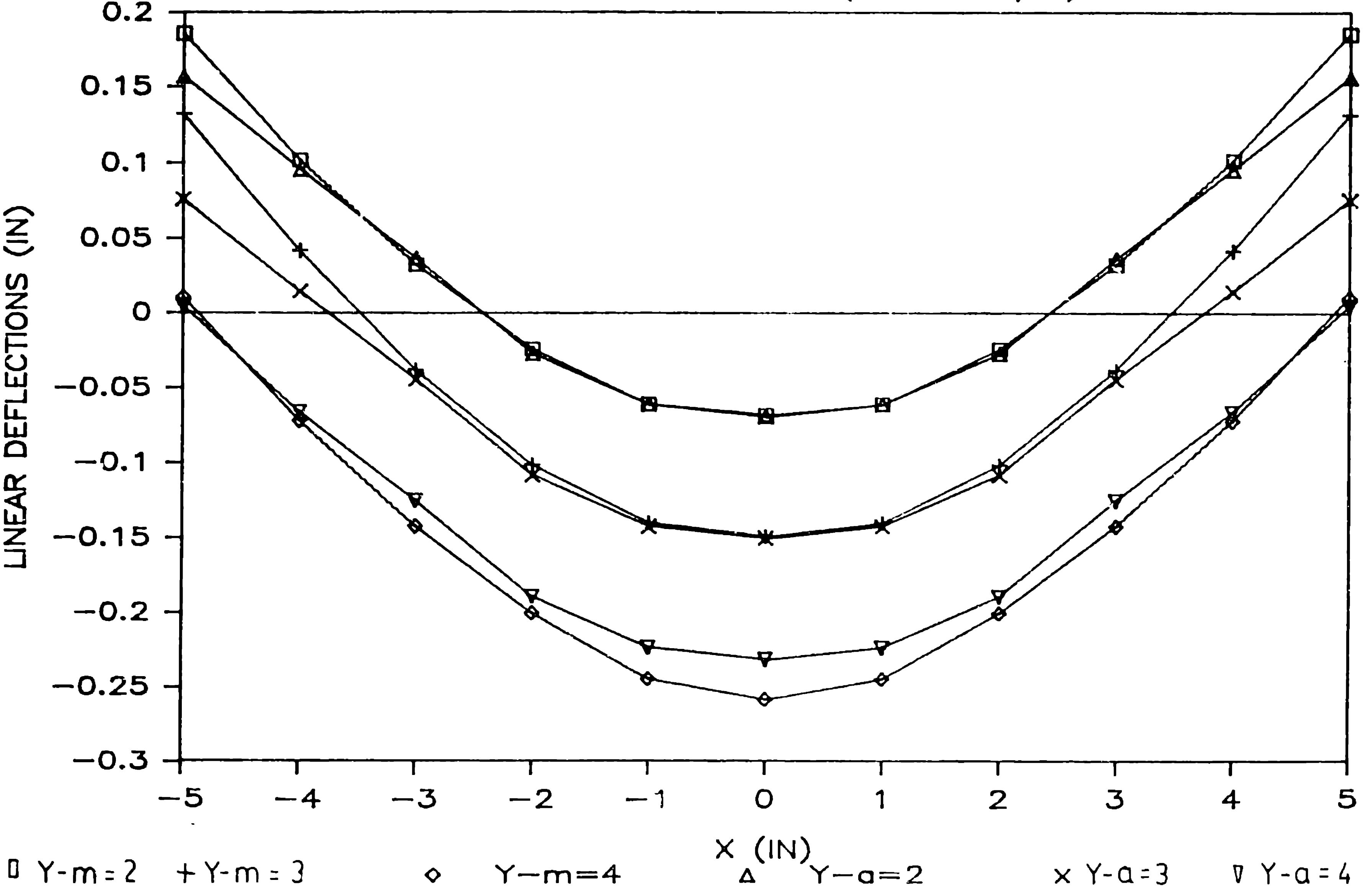

Figure 5.3.4—9: Algorithm & Actual

Deflections for Saddle (Y≥0)

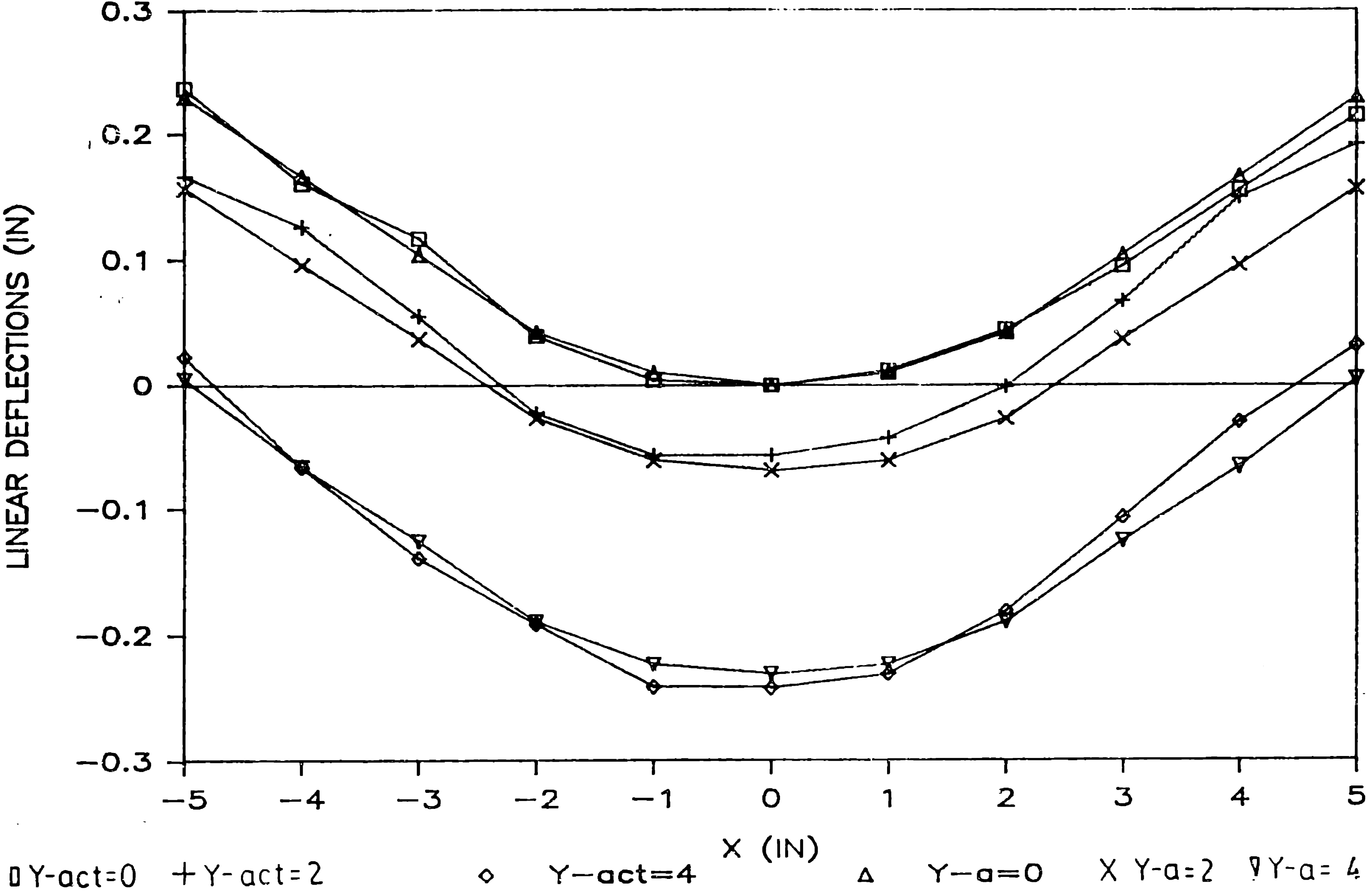

Figure 5.3.4—10: Algorithm & Actual

Deflections for Saddle (Y≤0)

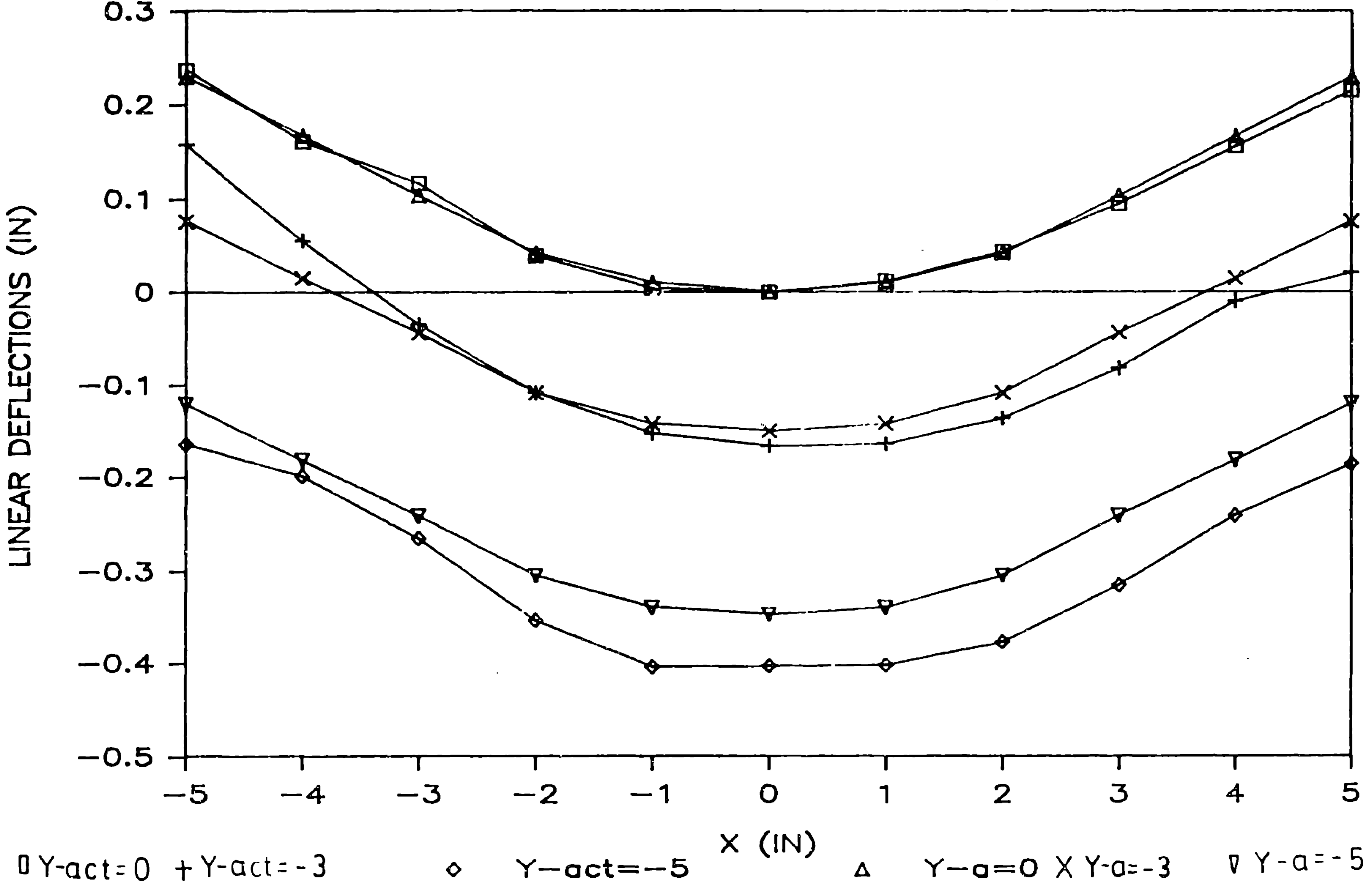

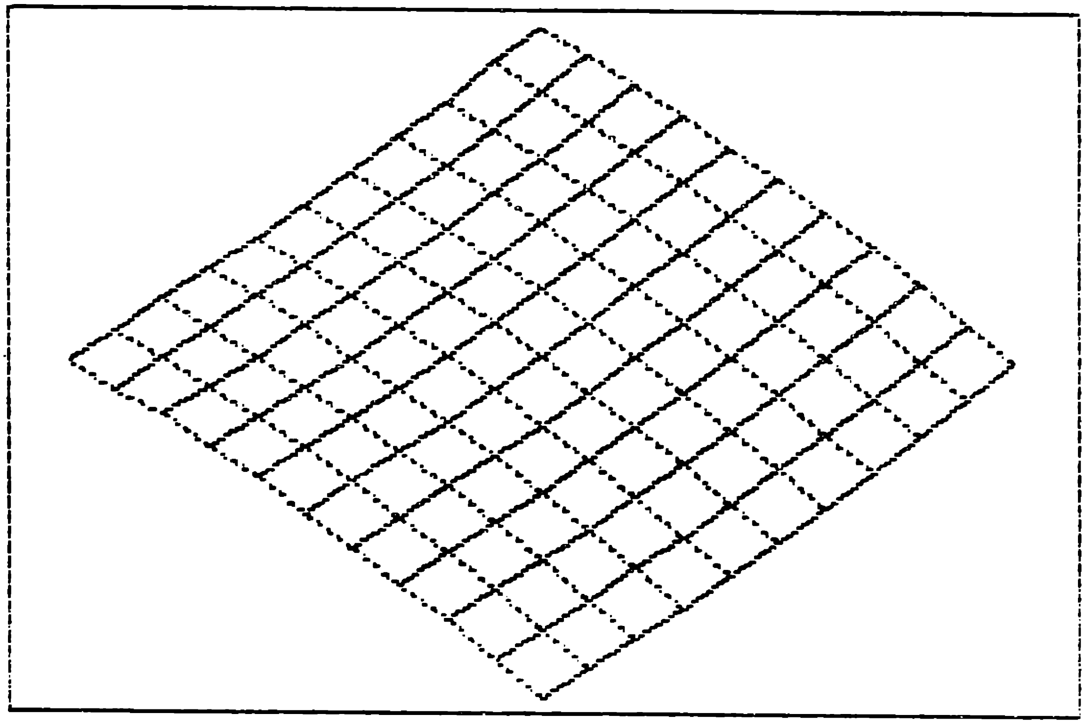

Figure 5.3.4-11: 3-D Perspective of the Saddle Shape with Actual Deflections

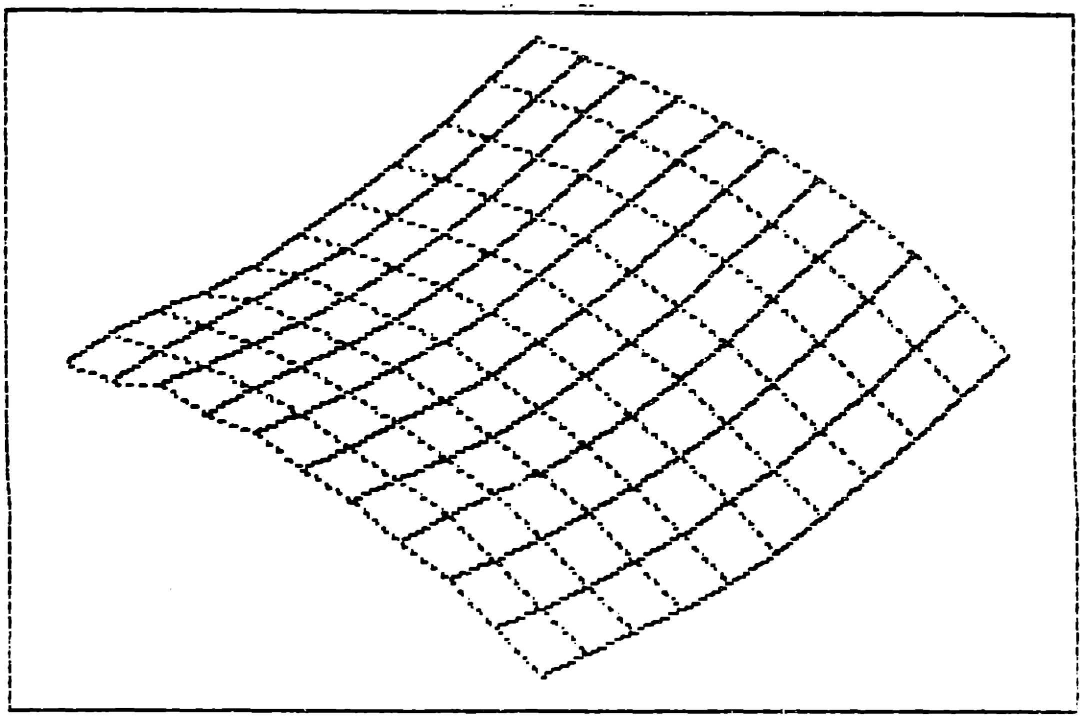

Figure 5.3.4-12: 3-D Perspective of the Saddle Shape with Deflections Magnified 3 Times

CHAPTER SIX

CONCLUSION AND RECOMMENDATIONS FOR FUTURE RESEARCH

The main purposes of the research and analyses in this paper have been proven. Namely:

a. The technique of irradiating a plate with a laser under controlled conditions is a reproducable and predictable phenomenon. Complex shapes can be mathematically constructed with reasonable accuracy using simple, linearized equations and well-known aspects of geometric symmetry.

b. Generality between algorithms has been established through the use of the TAN(k) parameter, poisson's ratio, plate dimensions, and the same general methodology.

c. Residual stress analysis appears to be consistent with the general algorithmic development with respect to poisson's effect.

d. All methods used to establish the construction algorithms are applicable to flame line heating as well as laser line heating with appropriate modifications for differences in heating parameters. This should provide sufficient flexibility for further development of a general line heating automated process using either lasers or flames.

It was stated previously that the algorithms developed in this paper are only a "first step". Admittedly, they lose accuracy near the edges and sometimes near the points of maximum and minimum curvature. Future research should, in part, focus toward "fine-tuning" them. Futhermore, the eventual goal of the algorithmic development should be to generalize the shapes into as few algorithms as is practicable. Possibly all conical and spherical shapes can be generalized into a single algorithm. Due to the lack of experimental data, it was not possible to generate general algorithms which would cover a variety of pure or combined shapes. For example, no algorithm was generated which would predict with correlatable accuracy a combined shape such as a sine curve superimposed on a conical shape. Also, since no experimental data exists on shapes which were unsymetrically heated in terms of the P/ V for the various passes, the applicability of these algorithms to this condition is untried and may not be accurate. However, futher experimentation including that which is on-going at the time of this writing should clarify and better define the scope of applicability of these routines.

Most research, up to this time, has concentrated in producing a process to laser bend metals without much attention on the mechanisms and consequences of the process. The practicability of the process has been demonstrated. At some point the physics of laser line heating should be thoroughly investigated. This is of more than academic importance. For example, current studies indicate that laser beam spot geometry has a significant effect on the magnitude of deflections.

If this turns out to be true, P/ V, in itself, may no longer be the best parameter to use to correlate deflection angles. More research into the questions of power, thermal, and stress distributions are recommended.

With the exception of the conical shape, all the complex shapes formed up to now have been fabricated with beam passes either parallel or perpendicular to the edges of the plate. This may not be the most efficient pattern. Other patterns to produce the same shape may reduce the warpage and asymmetry found in the shapes already constructed. A dish might be formed by a circular or spiralling beam pattern and it conceivably could be more efficient and/or produce less warpage. Therefore, research is recommended in studying various patterns to produce a shape and in correlating the total heat required to produce the shape as compared to the patterns used in the experiments described in this paper.

Perhaps the most important of the recommendations is the investigation of using the laser bending with closed loop system to symetrize and dewarp a plate made with the laser. It has been shown that almost any shape can be fabricated. What has not been demonstrated up to now is if the same laser system can economically produce those shapes to the same tolerances required in many industries including ship building. The use of the laser interferometer/video system will be invaluable in accomplishing this.

REFERENCES

1. Masubuchi, K., "Phase I Report on Laser Forming of Steel Plates for Ship Construction", submitted to Todd Shipyards Corporation, Los Angelese Division, February 1985.

2. M^{c}Carthy, R. W., "Thermomechanical Forming of Steel Plates Using Laser Line Heat", S.M. Thesis, Department of Ocean Engineering, M.I.T., Cambridge, MA, June 1985.

3. Deacon, D. L., Material Degradation in Heavy Plates Caused by Bending with a Laser", S.M. Thesis, Department of Ocean Engineering, M.I.T., Cambridge, MA., June 1984.

4. Haidemenopoulos, G. N., "Heat Flow and Material Degradation During Laser Metal Forming", S.M. Thesis, Department of Ocean Engineering, M.I.T., Cambridge, MA., June 1985.

5. Moshaiov, A., "Thermo-Elastic-Plastic Plate Bending by a Boundary Element Method with Initial Plastic Moments", Ph.D Dissertation, Department of Naval Architecture and Marine Engineering, University of Michigan, Ann Arbor, Mich., 1985.

6. Masubuchi, K., Analysis of Welded Structures, Oxford: Pergamon Press, 1980.

7. Vishay Instruments,"Model P-350A Digital Strain Indicator Instruction Manual", November 1975.

Appendix A

Photographs: Complex Curvature Study

DISH SHAPE

PLATE SIZE	10in X 10in
PLATE THICKNESS	1/2 inch
MATERIAL	A-36 Mild Steel
POWER INPUT	6.3 KW
PLATE TRAVEL SPEED	12 ipm
HEAT INPUT	31.5 KJ/in
BEAM DIAMETER	1.5 in (38.1 mm)
NUMBER OF PASSES	30 (6 long., 6 trans., 9 diag., 9 di

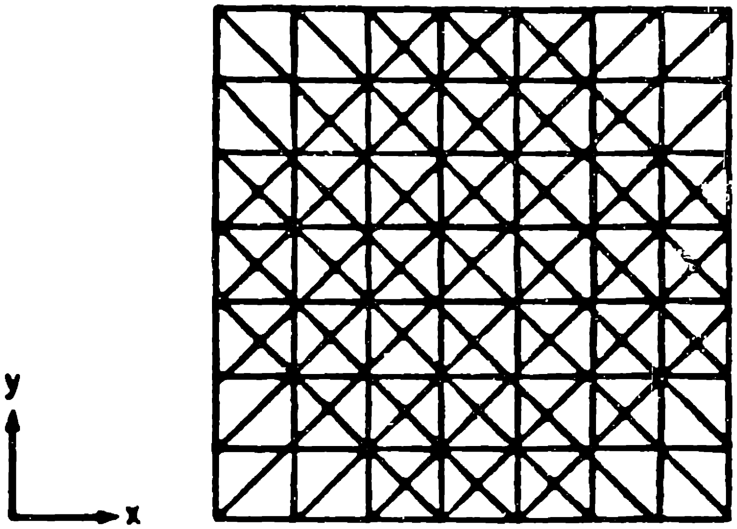

SOLID LINE: TOPSIDE PASS
DASHED LINE: PASS OPPOSITE SIDE

DISH SHAPE - WITH DIAGONAL PASSES

1/4" = 1"

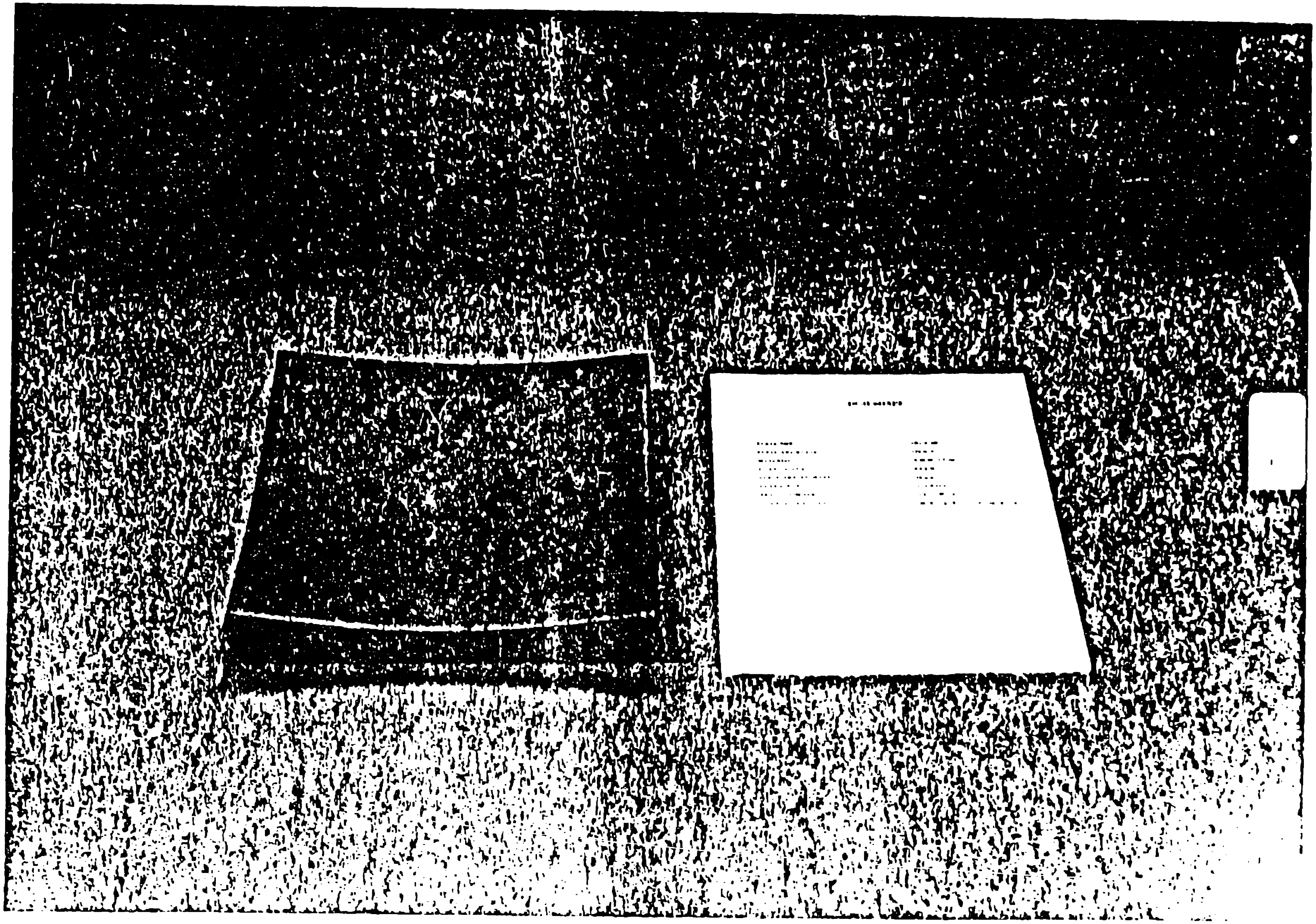

CONE SEGMENT

PLATE SIZE	18in X 24in
PLATE THICKNESS	1/2 inch
MATERIAL	A-36 Mild Steel
POWER INPUT	5.0 KW
PLATE TRAVEL SPEED	8 ipm
HEAT INPUT	37.5 KJ/in
BEAM DIAMETER	1 5/8 in (43.1 mm)
NUMBER OF PASSES	7 (topside only)

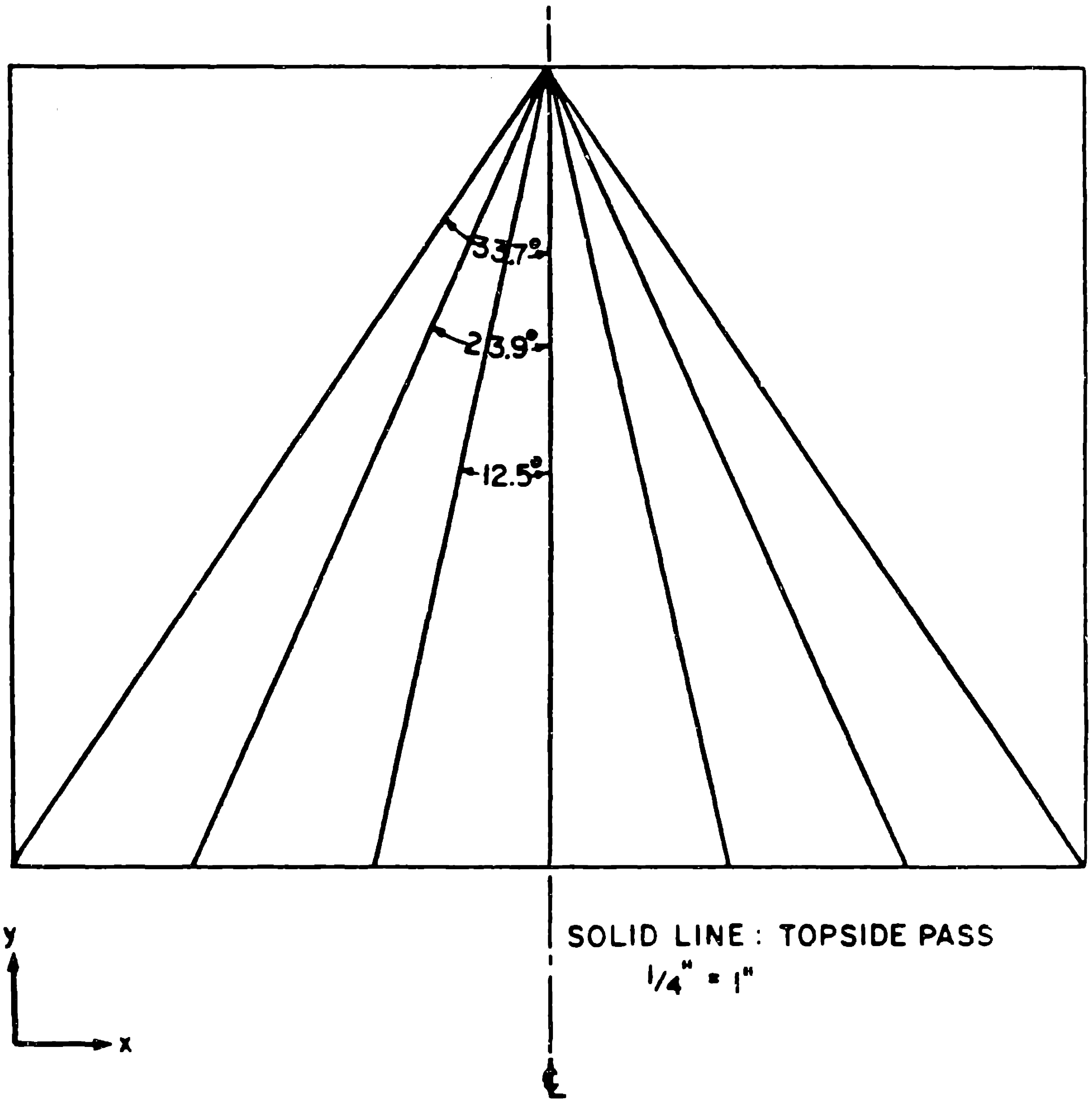

CONE SEGMENT I

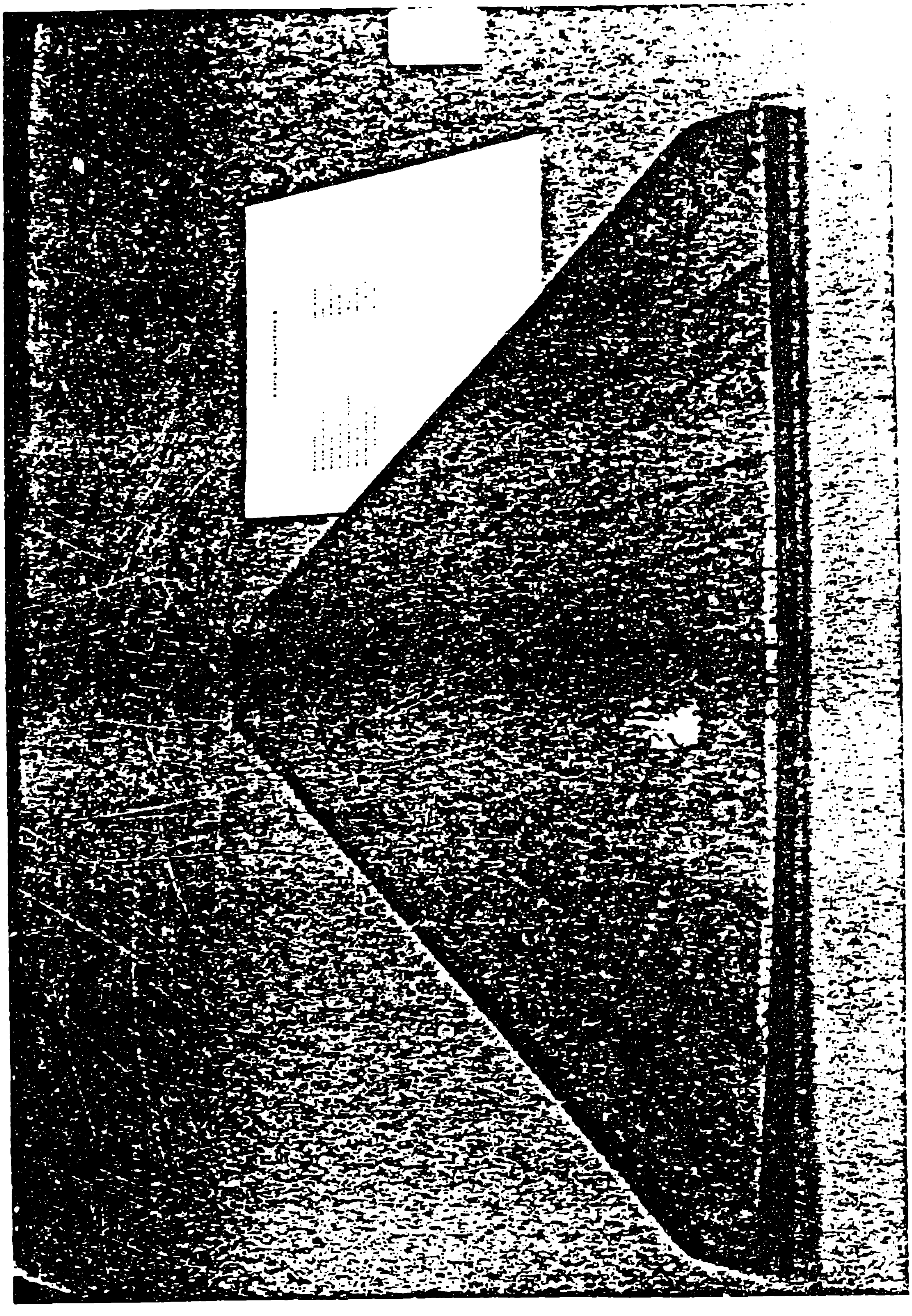

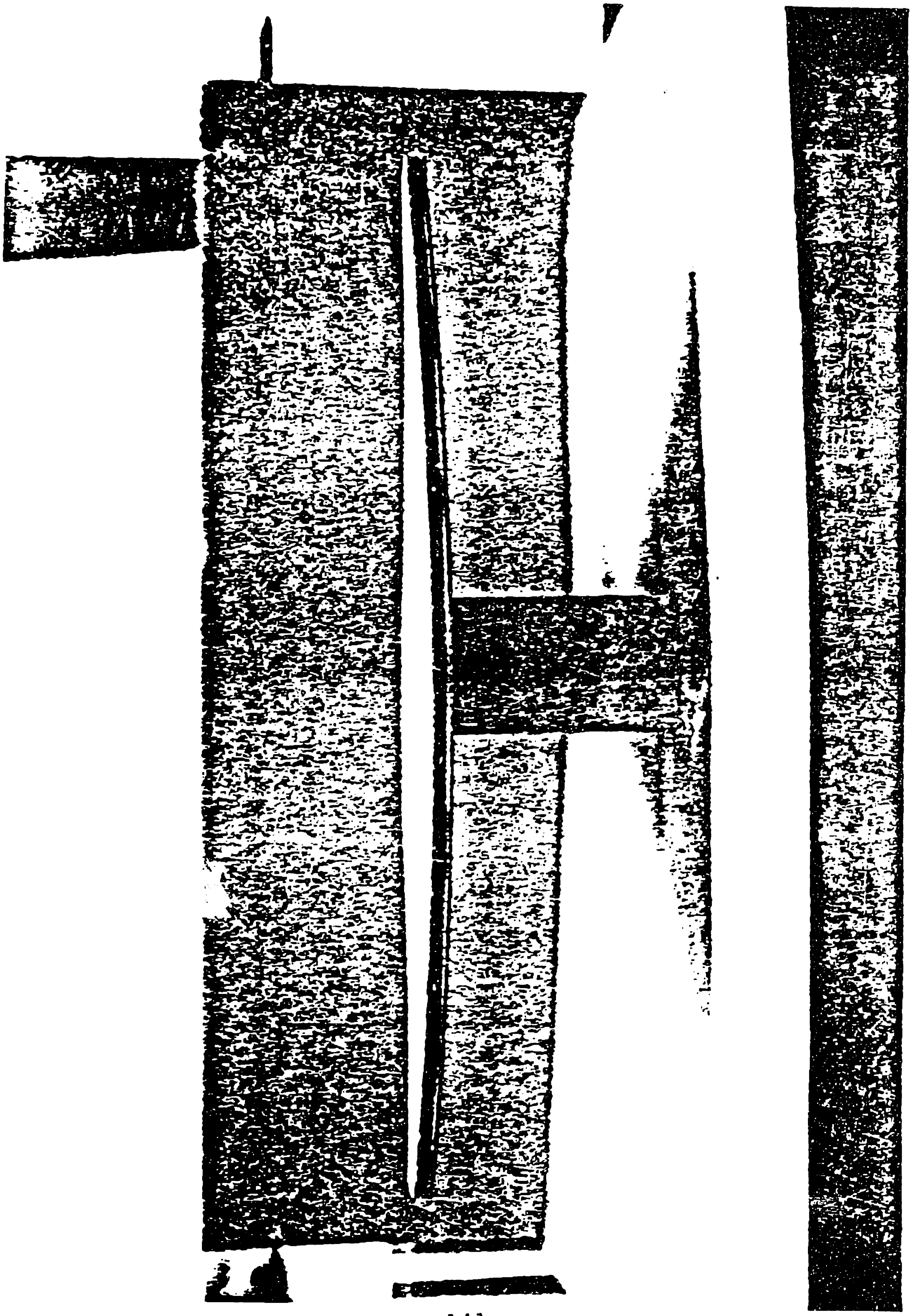

SINE SHAPE

PLATE SIZE	12in X 12in
PLATE THICKNESS	1/2 inch
MATERIAL	A-36 Mild Steel
POWER INPUT	6.3 KW
PLATE TRAVEL SPEED	12 ipm
HEAT INPUT	31.5 KJ/in
BEAM DIAMETER	1.5 in (38.1 mm)
NUMBER OF PASSES	8 (4 each side)

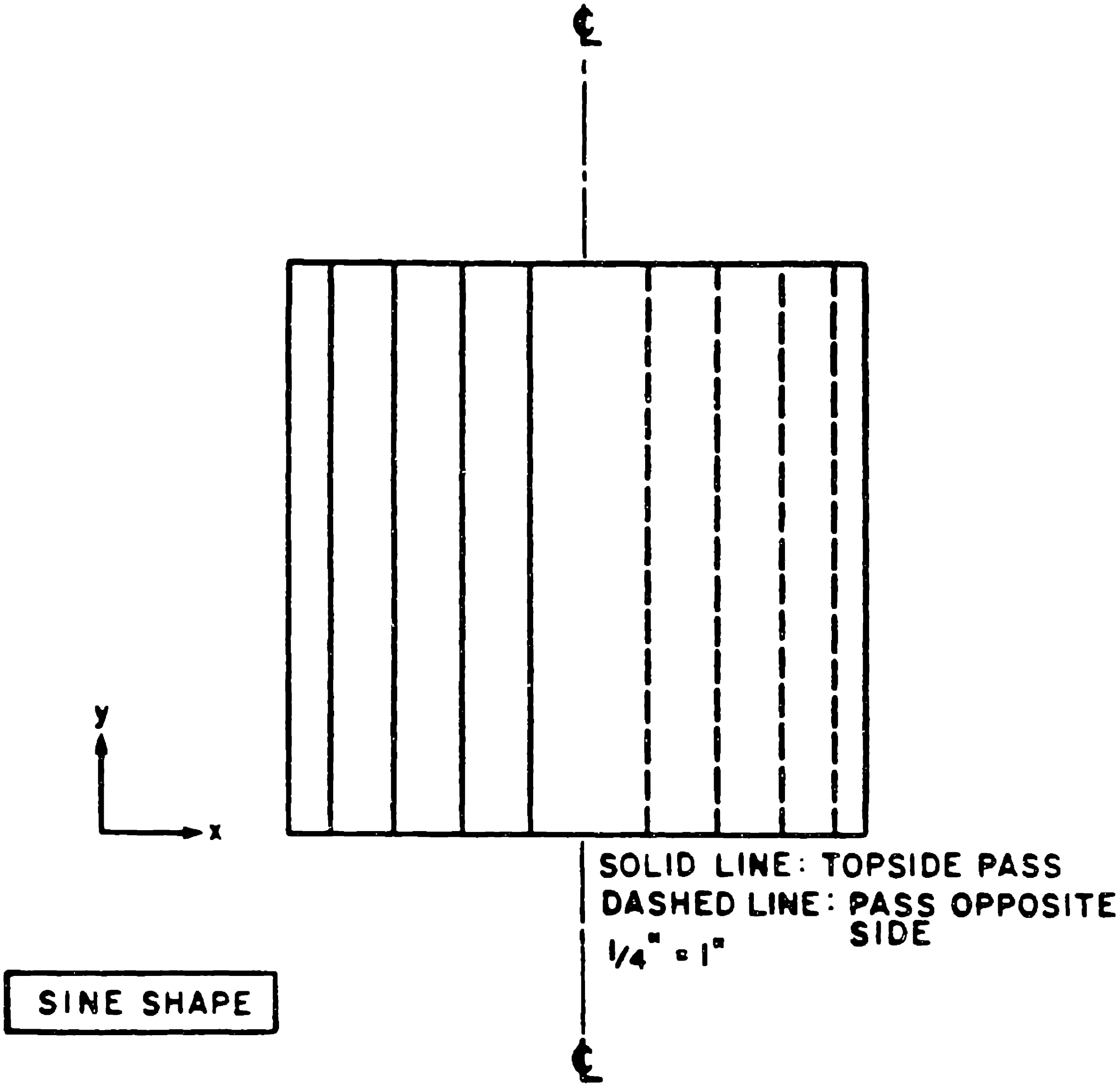
℄
y
x
SOLID LINE: TOPSIDE PASS
DASHED LINE: PASS OPPOSITE SIDE
1/4" = 1"
SINE SHAPE
℄

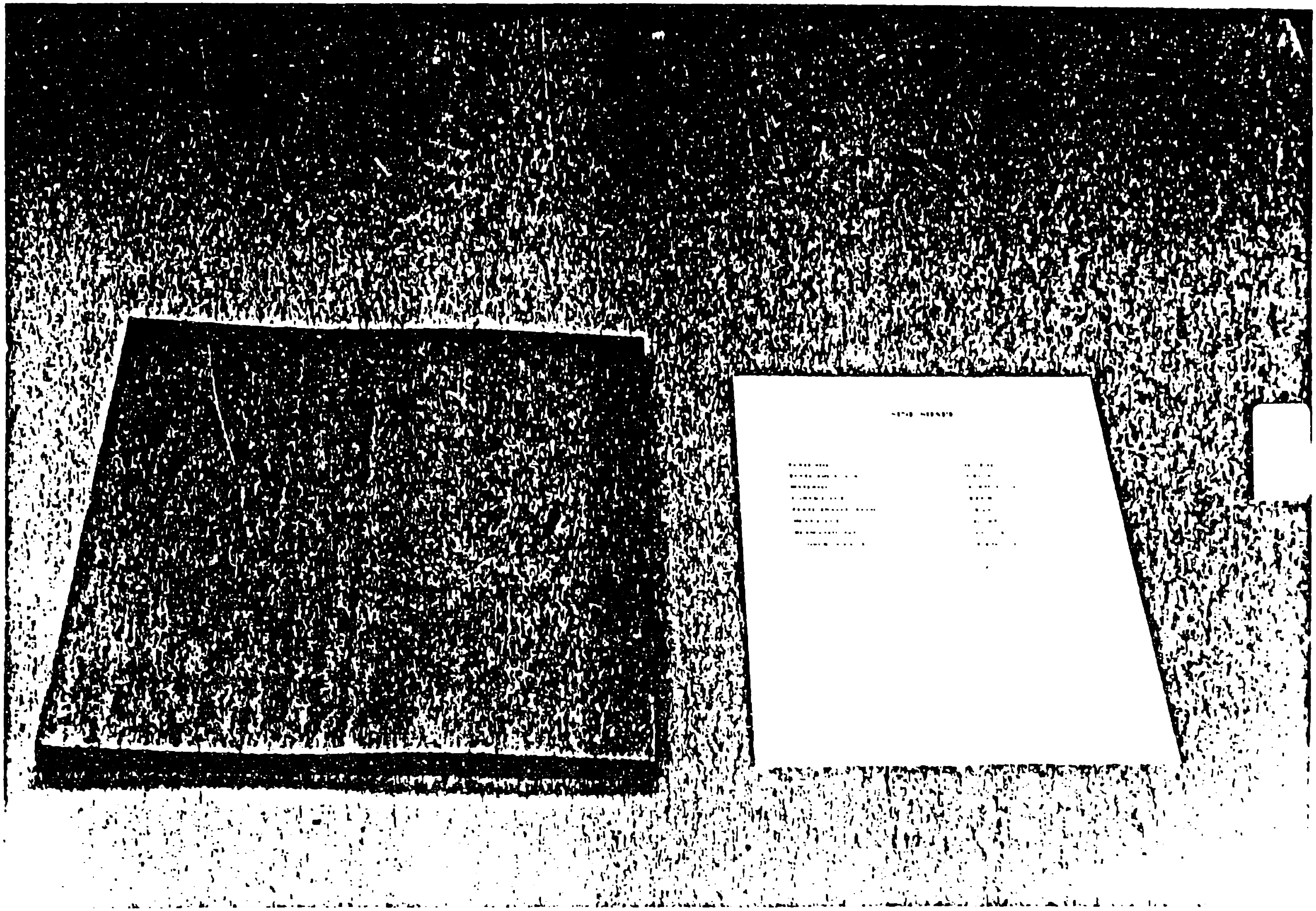

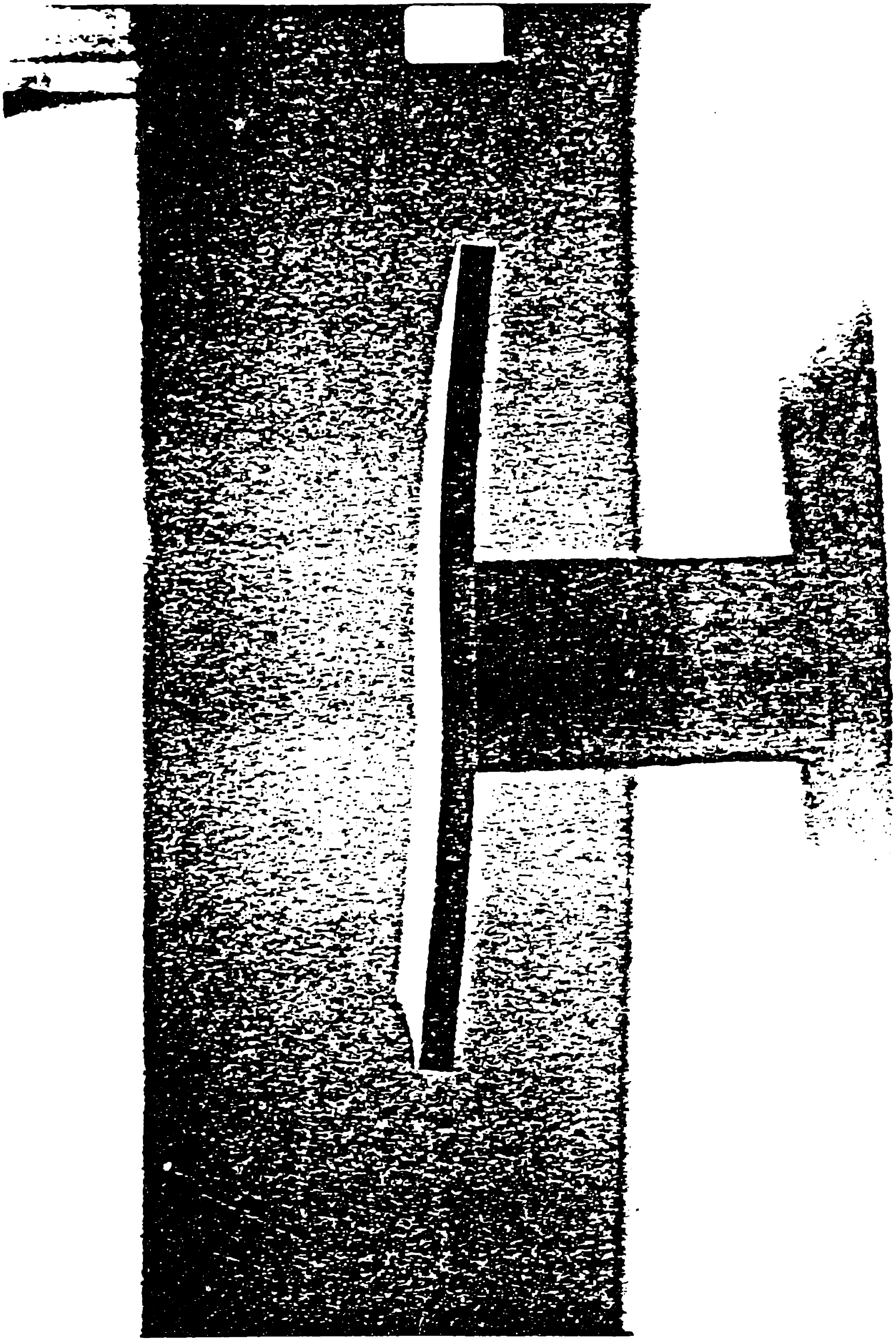

SADDLE SHAPE

PLATE SIZE	10in X 10in
PLATE THICKNESS	1/2 inch
MATERIAL	A-36 Mild Steel
POWER INPUT	6.3 KW
PLATE TRAVEL SPEED	12 ipm
HEAT INPUT	31.5 KJ/in
BEAM DIAMETER	1.5 in (38.1 mm)
NUMBER OF PASSES	32 (16 long. top, 16 trans

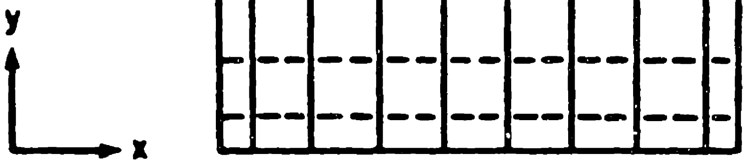

SOLID LINE: TOPSIDE PASS
DASHED LINE: PASS OPPOSITE SIDE

SADDLE SHAPE

1/4" = 1"

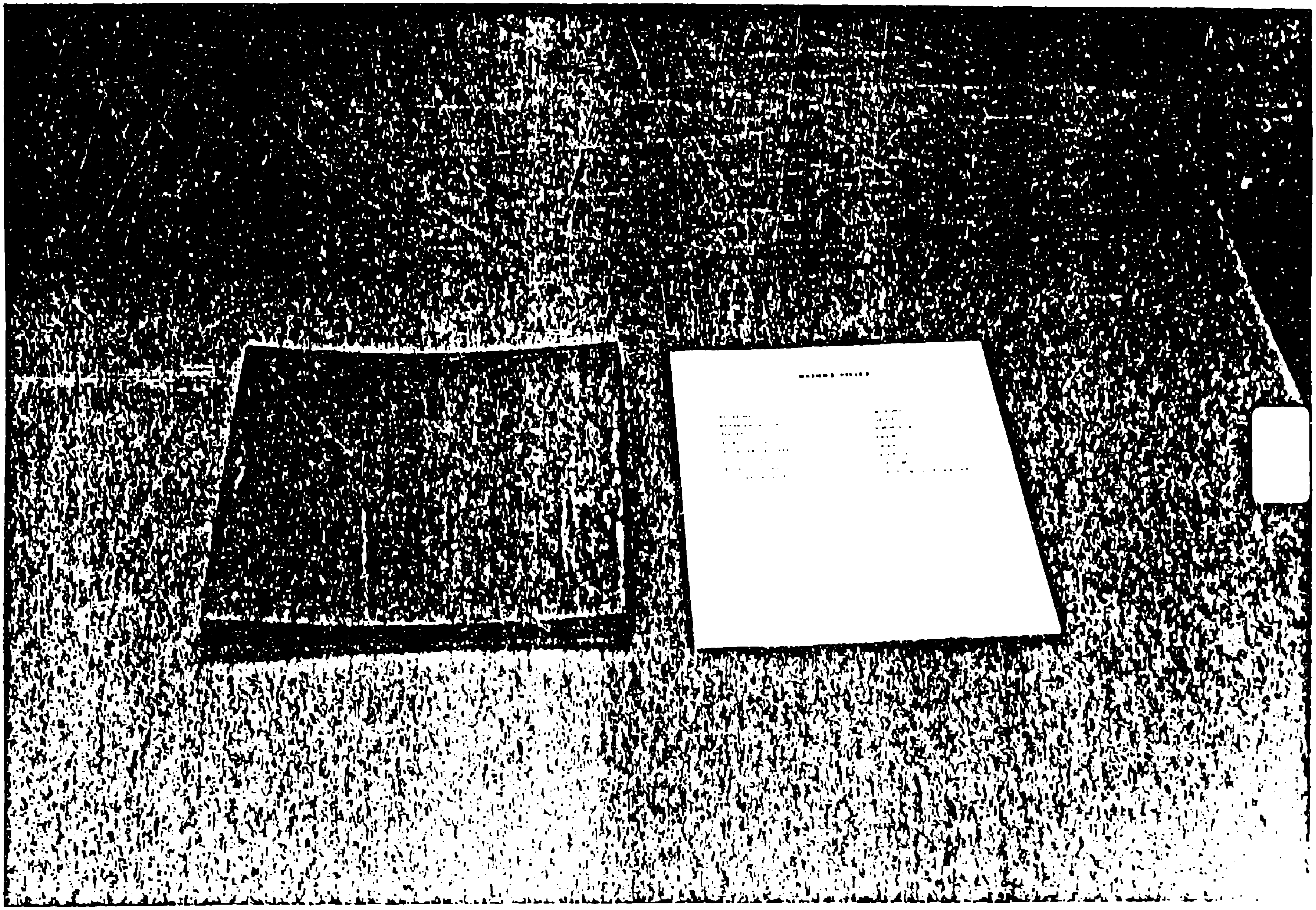

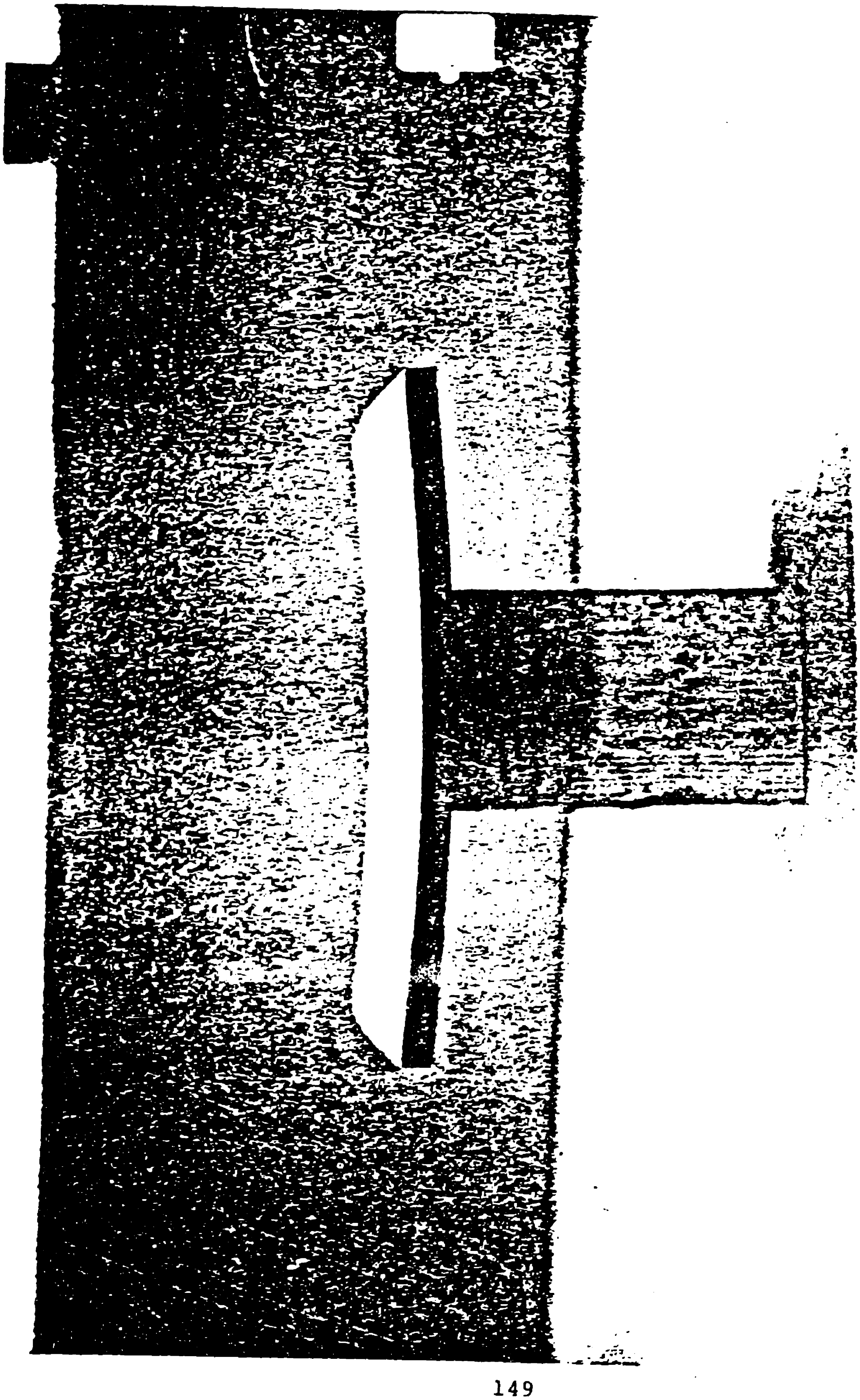

APPENDIX B

Application of the Algorithms/Predictions for Future Experiments

Ongoing research at the United Technologies Research Center (UTRC) in Hartford, Connecticut by M.I.T. staff and students is based on increasing the number of samples of complex shapes and, using the algorithms within this paper, to predict the deflections under given power parameters. Enclosed within Appendix B are the predictions for the deflections (symmetrized and dewarped) of the shapes. Furthermore, the research will determine if "fine tuning" with a laser is practicable. That is, can the formed plates be irradiated again to achieve the final desired deflections? All plates within this appendix are assumed to be 18"x24"x1/2" and the pattern of laser passes are the same as for those plates used to develop the algorithms. $P/\sqrt{V}$ and the number of laser passes are varied to determine the accuracy of the algorithm.

The beam spot of the CO_2 laser at UTRC is annular vice the "top hat" spot geometry of the laser at NRL. Beam diameter was varied in accordance with optical power theory to give approximately the same power density as that delivered by the 6 kW laser at NRL. The accuracy of this approach will be determined only after the analysis of the samples.

I. DISH

A. Parameters

$-P/\sqrt{V}$	1.708
$-\theta_f$	0.417°
-Number of Passes	10 diagonal
	10 diagonal
	10 longitudinal
	10 transverse

B. Equations

$$\tan(k) = \tan[(40)(.417)(22)916)/(2)(24)(18)]$$

$$z(x,0) = 0.0179|x| \qquad |x| \le 2.5''$$

$$z(0,y) = 0.0179|y| \qquad |y| \le 2''$$

$$z(x,0) = 0.0358|x| \qquad 2.5'' < |x| \le 5''$$

$$z(0,y) = 0.0358|y| \qquad 2'' < |y| \le 3.6''$$

$$z(x,0) = .1192|x| - .4005 \qquad 5'' < |x| \le 9.6''$$

$$z(0,y) = .1192|y| - .3004 \qquad 3.6'' < |y| \le 7.2''$$

$$z(x,0) = .0894|x| - .1144 \qquad 9.6'' < |x| \le 12''$$

$$z(0,y) = .0894|y| - .0858 \qquad 7.2'' < |y| \le 9''$$

C. Results

X +/-	Y +/-	Z	X +/-	Y +/-	Z	X +/-	Y +/-	Z	X +/-	Y +/-	Z
0	0	0	0	3	.107	0	6	.415	0	9	.719
3	0	.107	3	3	.215	3	6	.522	3	9	.826
6	0	.315	6	3	.422	6	6	.730	6	9	1.03
9	0	.672	9	3	.779	9	6	1.09	9	9	1.39
12	0	.958	12	3	1.07	12	6	1.37	12	9	1.68

II. <u>DISH</u>

A. Parameters

$-P/\sqrt{V}$	2.5
$-\theta_f$	1.2^{o}
-Number of Passes	Same as I.

B. Equations

$\tan(k) = .3553$

$z(x,0) = 0.0533|x| \qquad |x| \le 2.5''$

$z(0,y) = 0.0533|y| \qquad |y| \le 2''$

$z(x,0) = 0.1066|x| \qquad 2.5'' < |x| \le 5''$

$z(0,y) = 0.1066|y| \qquad 2'' < |y| \le 3.6''$

$z(x,0) = .3553|x| - 1.1938 \qquad 5'' < |x| \le 9.6''$

$z(y,0) = .3553|y| - .8954 \qquad 3.6'' < |y| \le 7.2''$

$z(x,0) = .2665|x| - .3411 \qquad 9.6'' < |x| \le 12''$

$z(0,y) = .2665|y| - .2558 \qquad 7.2'' < |y| \le 9''$

C. Results

X +/-	Y +/-	Z	X +/-	Y +/-	Z	X +/-	Y +/-	Z	X +/-	Y +/-	Z
0	0	0	0	3	.320	0	6	1.24	0	9	2.14
3	0	.320	3	3	.640	3	6	1.56	3	9	2.46
6	0	.940	6	3	1.26	6	6	2.18	6	9	3.08
9	0	2.0	9	3	2.32	9	6	3.24	9	9	4.14
12	0	2.86	12	3	3.18	12	6	4.09	12	9	5.0

III. CONE

A. Parameters

$-P/\sqrt{V}$	1.708
$-\theta_f$	0.417°
-Number of Passes	Same as Appendix A

B. Equations

$z(0,y) = 0$ $\quad -3'' \leq y \leq 3''$

$z(0,y) = -0.0140[y - 3]$ $\quad y > 3''$

$z(0,y) = 0.0140[y + 3]$ $\quad y < -3''$

$Y = 0$

$z(x,0) = .0201|x|$ $\quad |x| \leq 4''$ *

$z(x,0) = .0501[|x| - 2.4]$ $\quad 4'' < |x| \leq 8''$ **

$z(x,0) = .1153|x| - .6416$ $\quad 8'' < |x| \leq 12''$

*This equation applies for all y's (+/- or 0)

**This equation applies for $Y \leq 0$

$Y < 0$

$z(x,0) = .0807|x| - .3649$ $\quad 8'' < |x| \leq 12''$

$Y > 0$

$z(x,0) = .0737|x| - .2145$ $\quad 4'' < |x| \leq 12''$

C. Results

X	Y	Z	X	Y	Z
0	0	0	0	-6	-.042
3	0	.060	3	-6	.018
6	0	.180	6	-6	.138
9	0	.396	9	-6	.319
12	0	.742	12	-6	.561
0	3	0	0	9	-.084
3	3	.060	3	9	-.024
6	3	.228	6	9	.143
9	3	.456	9	9	.364
12	3	.670	12	9	.585
0	-3	0	0	-9	-.084
3	-3	.060	3	-9	-.024
6	-3	.180	6	-9	.096
9	-3	.361	9	-9	.277
12	-3	.603	12	-9	.519
0	6	-.042			
3	6	.018			
6	6	.186			
9	6	.407			
12	6	.628			

IV. CONE

A. Parameters

$-P/\sqrt{V}$	2.5
$-\theta_f$	1.2°
-Number of Passes	Same as Appendix A

B. Equations

$$z(0,y) = 0 \qquad |y| \leq 3''$$

$$z(0,y) = -0.0404[|y| - 1.8485] \qquad |y| > 3''$$

$Y = 0$

$$z(x,0) = .0578|x| \qquad |x| \leq 4''\ ^{*}$$

$$z(x,0) = 0.1444[|x| - 2.4] \qquad 4'' < |x| \leq 8''\ ^{**}$$

$$z(x,0) = .2325[|x| - 1.0513] \qquad 8'' < |x| \leq 12''$$

*This equation applies for all y's (+/- or 0)

**This equation applies for $Y \leq 0$

$Y \leq 0$

$$z(x,0) = .2335[|x| - 1.0513] \qquad 8'' < |x| \leq 12''$$

$Y \geq 0$

$$z(x,0) = .2123[|x| - .6181] \qquad 4'' < |x| \leq 12''$$

C. Results

X	Y	Z	X	Y	Z
0	0	0	0	-6	-.121
3	0	.173	3	-6	.052
6	0	.520	6	-6	.399
9	0	1.14	9	-6	.920
12	0	2.14	12	-6	1.62
0	3	0	0	9	-.243
3	3	.173	3	9	-.070
6	3	.656	6	9	.413
9	3	1.29	9	9	1.05
12	3	1.93	12	9	1.69
0	-3	0	0	-9	-.243
3	-3	.173	3	-9	-.070
6	-3	.520	6	-9	.277
9	-3	1.04	9	-9	.798
12	-3	1.74	12	-9	1.50
0	6	-.121			
3	6	.052			
6	6	.535			
9	6	1.17			
12	6	1.81			

V. Sine

A. Parameters

$-P/\sqrt{V}$	2.5
$-\theta_f$	1.2°
-Number of Passes	8 Passes Each Side

B. Equations

$$\tan(k) = \tan[(8)(1.2)(.815)/2] = 0.0684$$

$$z(x,0) = -0.2279x \qquad x \leq 4''$$

$$z(x,0) = -.0684x - .6383 \qquad 4'' < x \leq 5.4''$$

$$z(x,0) = .0684x - 1.3885 \qquad 5.4'' < x \leq 7.3''$$

$$z(x,0) = .19314x - 2.5108 \qquad 7.3'' < x \leq 12''$$

$$z(x,0) = -z(-x,0)$$

$$z(0,y) = -.05129|y| \qquad |y| \leq 4''$$

$$z(0,y) = -.0684|y| + .0570 \qquad 4'' < |y| \leq 9''$$

C. Results

X	Y	Z	X	Y	Z
0	0	0	0	6	-.353
3	0	-.684	3	6	-1.04
6	0	-.978	6	6	-1.33
9	0	-.773	9	6	-1.13
12	0	-.193	12	6	-.546
-3	0	.684	-3	6	.331
-6	0	.978	-6	6	.625
-9	0	.773	-9	6	.420
-12	0	.193	-12	6	-.160
0	3	-.154	0	9	-.558
3	3	-.838	3	9	-1.24
6	3	-1.13	6	9	-1.54
9	3	-.927	9	9	-1.33
12	3	-.347	12	9	-.751
-3	3	.530	-3	9	.126
-6	3	.824	-6	9	.420
-9	3	.619	-9	9	.215
-12	3	.039	-12	9	-.365

VI. SINE

A. Parameters

$-P/\sqrt{V}$	1.708
$-\theta_f$	0.417°
-Number of Passes	Same as VI.

B. Equations

$z(x,0) = -.0791x \qquad x \leq 4''$

$z(x,0) = -.0237x - .7383 \qquad 4'' < x \leq 5.4''$

$z(x,0) = .0237x - .4818 \qquad 5.4'' < x \leq 7.3''$

$z(x,0) = .0670x - .8713 \qquad 7.3'' < x \leq 12''$

$z(x,0) = -z(-x,y)$

$z(0,y) = -.0178|y| \qquad |y| \leq 4''$

$z(0,y) = -.0237 \qquad 4'' < |y| \leq 9''$

C. Results

X	Y	Z	X	Y	Z
0	0	0	0	6	-.123
3	0	-.237	3	6	-.360
6	0	-.339	6	6	-.462
9	0	-.268	9	6	-.391
12	0	-.067	12	6	-.190
-3	0	.237	-3	6	.114
-6	0	.339	-6	6	.216
-9	0	.268	-9	6	.145
-12	0	.067	-12	6	-.056
0	3	-.053	0	9	-.194
3	3	-.290	3	9	-.431
6	3	-.392	6	9	-.533
9	3	-.321	9	9	-.462
12	3	-.120	12	9	-.261
-3	3	.184	-3	9	.043
-6	3	.286	-6	9	.145
-9	3	.215	-9	9	.074
-12	3	.014	-12	9	-.127

VII. SADDLE

A. Parameters

$-P/\sqrt{V}$	1.708
$-\theta_f$	0.417°
-Number of Passes	16 Top; 16 Bottom

B. Equations

$$\tan(k) = \tan[(16)(.417)(.815)/2] = .0475$$

$$z(x,0) = .008 \qquad |x| = 2.5''$$

$$z(0,y) = .013 \qquad |y| = 2''$$

$$z(x,0) = .0158|x| \qquad 2.5'' < |x| \leq 5''$$

$$z(0,y) = .0260|y| \qquad 2'' < |y| \leq 3.6''$$

$$z(x,0) = .0475|x| - .1520 \qquad 5'' < |x| \leq 12''$$

$$z(0,y) = .0617|y| - .1286 \qquad 3.6'' < |y| \leq 7.2''$$

$$z(0,y) = .0867|y| - .3084 \qquad 7.2'' < |y| \leq 9''$$

where: $z(x,0) \geq 0$; $z(0,y) \leq 0$.

C. Results

X	Y	Z	X	Y	Z
0	0	0	0	6	-.242
3	0	.048	3	6	-.194
6	0	.133	6	6	-.109
9	0	.275	9	6	.033
12	0	.420	12	6	.178
0	3	-.078	0	9	-.472
3	3	-.030	3	9	-.424
6	3	.055	6	9	-.339
9	3	.197	9	9	-.197
12	3	.342	12	9	-.052

VIII. SADDLE

A. Parameters

$-P/\sqrt{V}$	2.5
$-\theta_f$	1.2^o
-Number of Passes	Same as VII.

B. Equations

$$\tan(k) = \tan[(16)(1.2)(.815)/2] = .1374$$

$$z(x,0) = .0229 \qquad |x| = 2.5"$$

$$z(0,y) = .0376 \qquad |y| = 2"$$

$$z(x,0) = .0458|x| \qquad 2.5" < |x| \leq 5"$$

$$z(0,y) = .0753|y| \qquad 2" < |y| \leq 3.6"$$

$$z(x,0) = .1374|x| - .4397 \qquad 5" < |x| \leq 12"$$

$$z(0,y) = .1786|y| - .3721 \qquad 3.6" < |y| \leq 7.2"$$

$$z(0,y) = .2509|y| - .8923 \qquad 7.2" < |y| \leq 9"$$

where: $z(x,0) \geq 0$; $z(0,y) \leq 0$.

C. Results

X	Y	Z	X	Y	Z
0	0	0	0	6	-.700
3	0	.137	3	6	-.562
6	0	.385	6	6	-.315
9	0	.780	9	6	.080
12	0	1.21	12	6	.509
0	3	-.226	0	9	-1.37
3	3	-.088	3	9	-1.23
6	3	.159	6	9	-.981
9	3	.554	9	9	-.586
12	3	.983	12	9	-.157